Proximity-induced transport phenomena in graphene-based spintronic devices

Daniel Solis Lerma

Daniel Solis Lerma. Proximity-induced transport phenomena in graphene-based spintronic devices. Materials Science [cond-mat.mtrl-sci]. Université Grenoble Alpes [2020-..], 2020. English. NNT : 2020GRALY012 . tel-03076712

HAL Id: tel-03076712
https://theses.hal.science/tel-03076712v1

Submitted on 16 Dec 2020

THÈSE

Pour obtenir le grade de

DOCTEUR DE L'UNIVERSITE GRENOBLE ALPES

Spécialité : **Physique de la Matière Condensée et du Rayonnement**

Arrêté ministériel : 25 mai 2016

Présentée par

Daniel SOLIS LERMA

Thèse dirigée par **Mairbek CHSHIEV**, Université Grenoble Alpes
et codirigée par **Xavier WAINTAL**, CEA

Préparée au sein du **Laboratoire Spintronique et Technologie des Composants (SPINTEC)** dans **l'École Doctorale Physique**

Phénomènes de transport sous effets de proximité dans des dispositifs spintroniques à base de graphène

Proximity-induced transport phenomena in graphene-based spintronic devices

Thèse soutenue publiquement le **13 Mai 2020**,
devant le jury composé de :

Monsieur Aurélien MANCHON
Professeur des universités, CINaM - Aix Marseille Université, Rapporteur
Monsieur Stephan ROCHE
ICREA Professor, Institut Català de Nanociència i Nanotecnologia, Rapporteur
Monsieur Alessandro CRESTI
Chargé de recherche, IMEP-LaHC (UMR 5130) - CNRS / Grenoble INP / UGA / USMB, Examinateur
Monsieur Philippe DOLLFUS
Directeur de recherche, C2N (UMR 9001) - CNRS / Université Paris-Saclay, Examinateur
Monsieur Olivier ISNARD
Professeur des universités, Institut NEEL (UPR 2940) - CNRS / UGA, Président du jury

Contents

Acknowledgments

After 3 years of preparation working with an exceptional group at Spintec and preparing my defense during a pandemic I have no more than words of thanks to all the people with whom I worked with and those with whom I shared one the most challenging and fascinating moments of my life.

I would like to start by expressing my greatest gratitude to my advisor Mairbek Chshiev for giving me the opportunity to work in his group, for his guidance, patience and for helping me to think differently. I am thankful for all the time spent hearing my presentations, reading my drafts and correcting my thesis. Mair always encourage me and gave me the opportunity to attend different schools, conferences and workshops on spintronics and 2D materials and thanks to this I was able to broaden my horizons and learn many new things.

I would like also to express my greatest gratitude to my co-advisor Xavier Waintal for all the suggestions, explanations and help. Xavier was always showing me where I was wrong and I am really grateful for that, I learnt a lot from all those mistakes and his suggestions.

Special thanks to my jury committee members: Aurélien Manchon, Stephan Roche, Alessandro Cresti, Philippe Dollfus and Olivier Isnard for having interest on my work and for all the suggestions and feedback given.

Last but not least, I would like to thank to Nessita for all the motivation, care and love. To my mother for believing in me, also to my friends and family. To Ali and Fatima for all the insightful discussions we had and of course all wonderful people I met at Spintec.

Abstract

In this thesis we present a study of transport properties of a proposed lateral graphene-based spintronic device comprising two identical magnetic regions induced by proximity of magnetic insulators on top of a graphene sheet. We investigate in detail the spin-dependent transport properties of the device in both collinear and non-collinear configuration of the magnets. In particular, we focus on the magnetoresistance phenomena induced by various magnetic insulators, as well as, the impact of ferroelectricity when the magnets are made of the multiferroic material BFO. We demonstrate the existence of proximity magnetoresistance phenomena (PMR) generating spin polarized currents without direct injection through the ferromagnet and present promising results at room temperature. Furthermore, the possibility of tuning of the magnetoresistance by the electrical polarization of BFO is demostrated. Namely, the extra degree of freedom allows defining two extra physical quantities: the proximity electroresistance (PER) and proximity multiferroic resistance (PMER). In addition, we provide a theoretical derivation of the spin current conservation equation for the case when the Hamiltonian of the system has spin dependent hoppings and sublattice potential. Lastly, we study in detail the spin transfer phenomena (STT) in the proposed spin valve device considering magnets made of yittrium iron garnet (YIG) including STT dependence with respect to size dimensions. We calculate the corresponding phase diagram, from which it is possible to estimate the order of magnitude of the current needed to switch the magnetization of thin magnet adjacent to graphene

Résumé

Dans cette thèse, nous présentons une étude des propriétés de transport d'un vanne de spin lateral a basse de graphène constitue de deux régions magnétiques identiques induite avec isolant magnétiques par effets de proximité sur une feuille de graphène. Nous étudions en détail le transport de spin dans deux configurations magnétiques différentes de les aimants: colinéaires et non colinéaires. En particulier, nous nous concentrons sur les phénomènes magnétorésistence, ainsi que l'impact de la ferroélectricité lors des aimants fait de le multiferroïque BFO. Nous démontrons l'existence d'une magnétorésistance de proximité (PMR) en générant une polarisation du courant de spin sans injection directe à travers le ferromagnet et présentent des résultats prometteurs à température ambiante. De plus, nous démontrons la possibilite de manipule la magnétorésistance par la polarisation électrique du BFO. En raison du degré de liberté supplémentaire, nous définissons deux quantités physiques supplémentaires: la électrorésistance de proximité (PER) et la résistance multiferroïque de proximité (PMER). De plus, nous fournissons une dérivation théorique de l'equation de conservation du courant de spin pour le cas où le hoppings et le potentiel de sous-réseau de l'hamiltonien du système sont dépendant du spin. Enfin, nous étudions en détail les phénomènes de couple de transfert de spin dans le vanne de spin proposé en regardant des aimants fait de YIG, sa dépendance par report le dimensions de system et fait le calcul correspondant pour obtenir leur diagramme de phase, à partir duquel il est possible estimer l'ordre de grandeur du courant nécessaire pour commuter la magnetization d'un aimant fin adjacent à graphène.

CHAPTER 1

Introduction

In the operation of conventional electronic devices the charge of the electron is considered only and “0” and “1” states are defined by letting or not to flow charge current through a particular gate. The advent of the miniaturization of devices and the demand of more efficient devices, has permitted to remain in accordance with the Moore’s law of exponential increase of transistor per square inch in integrated circuits. The transistors are essentially an electrically driven switch that permits or denies the flow of electrons. A transistor is composed by a source, a drain and a gate. Depending on the voltage in the gate, current can be transmitted from the source to the drain.

The number of transistors in a chip determine its capacity. To increase the number of transistors in a chip, basically two approaches are followed, either novel transistor designs are developed in order to shrink the transistor’s size, or novel chip architectures are proposed in order to pack more transistors per area unit. As more and more transistors are included in the chips, the greater becomes the Joule heating in the device, decreasing its performance. Shrinking the transistor’s size also present technical limitations, being the most important, the efficiency reduction of the electrical current blocking by the gate, due to the quantum tunneling, whose probability is enhanced as the separation of the drain and the source is decreased. So, within few years the chips capacity will reach a technical limit imposed by physics.

One option to overcome these issues is to increase the information carried by the electrons, adding new functionalities and capabilities to the already existing devices, or to create devices that explore a quantum property called spin in addition to electron’s charge. The use of this extra degree of freedom can be the solution to the stagnant challenge we will face within few years, as we get closer to the end of the Moore’s law.

1.1 Magnetism

Since ancient times humanity have been captivated by the magnet's ability to attract ferrous objects from the distance. Perhaps the most remarkable use of magnetism was in the compass, a device invented in China in the XI century that is composed by a free to rotate metallic piece with magnetized tip. Because the tip was able to align with the earth's magnetic field, pointing always north (south), the compass was a very important tool for the orientation during navigation, that is still in use nowadays.

Regardless of the numerous experiences carried out the following centuries after the compass invention, no much understanding on the nature of magnetism was achieved. Things started to change in the late 18th century, when ideas about the connection between magnetism and electricity spread over Europe stimulating different scientific communities. The first prove of this connection was found in 1820, when Hans-Christian Oersted discovered by accident that a current in a wire was able to deflect the compass needle. Almost at the same time Ampére showed that when electrical current travels in a coil, this system behaves as a magnet. In 1821 Michael Faraday discovered the magnetic induction and some time later (1845), proved the relation between magnetism and optics with the magneto-optic Faraday effect [1]. All these discoveries where summarized in four equations by Clerk Maxwell, that completely revolutionized physics and unified forever light, electricity and magnetism. The famous equations are the following:

$$\begin{aligned} \nabla \cdot \mathbf{B} &= 0, \\ \epsilon_0 \nabla \cdot \mathbf{E} &= \rho, \\ \frac{\nabla \times \mathbf{B}}{\mu_0} &= \mathbf{j} + \epsilon_0 \frac{\partial \mathbf{E}}{\partial t}, \\ \nabla \times \mathbf{E} &= -\frac{\partial \mathbf{B}}{\partial t} \end{aligned} \tag{1.1}$$

E and **B** are the electric and magnetic field respectively, ρ indicates the charge distribution and **j** is the current density. The first equation is the Gauss's law for magnetism and physically indicates that it is not possible to have magnetic monopoles, the second equation is the "usual" Gauss's law and relates the electric flux across surface S with the charge in the volume V, that enclose the surface S. The third equation is the Ampére law that relates the generation of a magnetic field by currents in circuits as well as by time dependent electrical fields and the last equation is the Faraday's law of induction that explains how a time dependent magnetic field can induce an electrical current. From these equations the connection with magnetism is not obvious. To make it evident, let us use the displacement field **D** and the magnetizing field **H** in the Maxwell equations instead of **B** and **E**. These quantities are defined as:

$$\mathbf{H} = \left(\frac{1}{\mu_0}\mathbf{B} - \mathbf{M}\right) \tag{1.2}$$

$$\mathbf{D} = \left(\epsilon_0 \mathbf{E} - \mathbf{P}\right), \tag{1.3}$$

where **M** is the magnetization and **P** is the electrical polarization density. The Maxwell's equations are then written as:

$$\begin{aligned}
\nabla \cdot \mathbf{H} &= 0, \\
\nabla \cdot \mathbf{D} &= \rho_f, \\
\frac{\nabla \times \mathbf{H}}{\mu_0} &= \mathbf{J}_f + \frac{\partial \mathbf{D}}{\partial t}, \\
\nabla \times \mathbf{E} &= -\frac{\partial \mathbf{B}}{\partial t},
\end{aligned} \tag{1.4}$$

where ρ_f and $\mathbf{J}_f$ are the free charge and free current respectively. These equations are known as the Maxwell's equations in matter. For more details please see Ref. [2].

Despite the Maxwell equations were able to explain the interaction between currents and magnetic dipoles, and predicted the existence of electromagnetic waves, a satisfactory explanation for the ferromagnetic phenomenon was still missing. The explanation only came after two key discoveries, the electron in 1897 by Joseph John Thompson and the electron's intrinsic momentum (spin) in 1925 by George Uhlenbeck and Samuel Goudsmit. Thanks to these findings and the development of quantum mechanics and relativity theory in the XX century, it became possible to explain the spontaneous magnetization.

The spontaneous magnetization is a phenomenon of pure quantum mechanical origin and is a direct consequence of the Pauli's principle. Pauli's principle enforces the fermions wave functions to be antisymmetric. Let us consider the wave function of a system composed by two hydrogen atoms, and considering the Born-Oppenheimer approximation we will care only about the 2 electrons of the system, so that their wave function can be written as:

$$\psi(1,2) = \chi(\sigma_1, \sigma_2)\varphi(\vec{r}_1, \vec{r}_2),$$

where χ is the spin function part while ϕ is the particle position part. ψ is antisymmetric if $\psi(1,2) = -\psi(2,1)$, so either χ is antisymmetric or ϕ is antisymmetric. In this situation we can construct the following spin wave functions:

$$\chi_A = \frac{1}{\sqrt{2}}(|\uparrow\downarrow\rangle - |\downarrow\uparrow\rangle), \text{ for S=0} \tag{1.5}$$

$$\chi_S = \frac{1}{\sqrt{2}}(|\uparrow\downarrow\rangle + |\downarrow\uparrow\rangle);\ |\uparrow\uparrow\rangle;\ |\downarrow\downarrow\rangle, \text{ for S=1}, \tag{1.6}$$

where χ_A and χ_S are the spin wave function of the antisymmetric and symmetric case, respectively. Eqs. (1.5) and (1.6) are known as singlet and triplet state spin functions, respectively. The reason for these labels is that there is only one state in the former one due to the fact there is only one magnetic quantum number $m_l = 0$, while in the latter one there are 3 states because its magnetic quantum number m_l can be any value in the set $\{-1, 0, 1\}$. The corresponding spatial wave functions are:

$$\varphi_S = \frac{1}{\sqrt{2}}(\phi_A(\vec{r}_1)\phi_B(\vec{r}_2) + \phi_A(\vec{r}_2)\phi_B(\vec{r}_1)), \text{ for S=0} \tag{1.7}$$

$$\varphi_A = \frac{1}{\sqrt{2}}(\phi_A(\vec{r}_1)\phi_B(\vec{r}_2) - \phi_A(\vec{r}_2)\phi_B(\vec{r}_1)), \text{ for S=1,} \tag{1.8}$$

where Eq. (1.7) and Eq. (1.8) correspond to a symmetric and antisymmetric spatial wave function respectively. Usually the spins in the materials point randomly, so the average magnetization is zero, this magnetic configuration or phase is known as paramagnetic state. The magnetic ordering emerges in materials where this phase is energetically advantageous for the atoms in the lattice, that is why not all the materials are ferromagnetic [3]. This feature gives rise to the well-known exchange interaction, which at the core, is nothing more than electrostatic interaction, of particular relevance the Coulomb repulsion [4]. So, just considering the latter, the exchange interaction can be written as:

$$H = H_0 + H_{repulsion}, \tag{1.9}$$

with $H_0 = \frac{p_1}{2m_1} + \frac{p_2}{2m_2} - \frac{e^2}{|\vec{r}_1|} - \frac{e^2}{|\vec{r}_2|}$ and $H_{repulsion} = \frac{e^2}{|\vec{r}_1 - \vec{r}_2|}$, being p the momentum, m the mass of the electron and e its charge. The effective interaction is then:

$$\mathit{\Delta} E = E_A - E_S = \langle\varphi_A|H|\varphi_A\rangle - \langle\varphi_S|H|\varphi_S\rangle, \tag{1.10}$$

where E_A and E_S are the energy of the triplet and single state, respectively. Substituting Eq. (1.9) into the previous equation we get:

$$\mathit{\Delta} E = J_{ex}, \tag{1.11}$$

where we have defined

$$J_{ex} = e^2 \int d^3 r_1 \int d^3 r_2 \frac{\phi_A^*(\vec{r}_1)\phi_B^*(\vec{r}_2)\phi_A(\vec{r}_2)\phi_B(\vec{r}_1)}{|\vec{r}_1 - \vec{r}_2|}. \tag{1.12}$$

J_{ex} is the well-known exchange integral. This integral do not have a simple physical interpretation, but it is known is related to the exchange constant of the Heisenberg model. For more details please see Ref. [3]. A simplified model to explain ferromagnetic ordering is the Stoner theory, which uses mean field theory to solve the Hubbard Hamiltonian and can be written as:

$$\mathcal{H}_{\mathcal{U}} = U \sum_i n_i^{\uparrow}\langle n_i^{\downarrow}\rangle + n_i^{\downarrow}\langle n_i^{\uparrow}\rangle - \langle n_i^{\uparrow}\rangle\langle n_i^{\downarrow}\rangle, \tag{1.13}$$

where $n_i^{\uparrow(\downarrow)}$ is the local spin up (down) electronic density. This quantity can be rewritten as:

$$\begin{aligned} n_i^{\uparrow} &= \frac{1}{2}\left(\rho_i^c + \rho_i^s\right) \\ n_i^{\downarrow} &= \frac{1}{2}\left(\rho_i^c - \rho_i^s\right), \end{aligned} \tag{1.14}$$

with $\rho_i^c = n_i^{\uparrow} + n_i^{\downarrow}$ being the electronic density in the site i and $\rho_i^s = n_i^{\uparrow} - n_i^{\downarrow}$ being the spin density in the site i. For a metallic system (parabolic dispersion) it is easy to show that a small perturbation in the number of majority and minority electrons leads to

$$\mathit{\Delta} E = \mathit{\Delta} E_K - \mathit{\Delta} E_U \approx \frac{2\langle\rho^s\rangle^2}{g(E_F)} - U\langle\rho^s\rangle^2, \tag{1.15}$$

where E_K is the kinetic energy ($\propto p^2$), E_U is the mean field Hubbard energy, U represents the strength of the electron repulsion and $g(E_F)$ is the density of states at the Fermi energy. To have ferromagnetism is necessary to have $\mathit{\Delta} E$ negative, what happens when

$$U > \frac{2}{g(E_f)}. \tag{1.16}$$

This equation is the well-known Stoner criterion. This criterion is only satisfied by 3d metals like Fe, Co and Ni. The main limitation of this model is that it does not take into account the correlated spin excitations. More information about the Stoner model can be found in Ref. [3]. A more accurate model that includes the correlated spin excitations is the Heisenberg model. In 1929 Heisenberg aiming to explain ferromagnetism, proposed the following Hamiltonian that describes a direct interaction of magnetic moments in a crystal:

$$H = -\sum_{i,j} \mathcal{J}\mathbf{S}_i \cdot \mathbf{S}_j, \tag{1.17}$$

where $\mathcal{J}$ is the exchange constant and $\mathbf{S}_{i(j)}$ represents the spin of an atom in the $i(j)$ position. If $\mathcal{J}$ is negative, the spins in the system point in opposite directions. The system is antiferromagnetic if the magnetic moments have the same magnitude, in contrast if their magnitude differ, the system presents a non-zero magnetization and the system is called ferrimagnetic. When $\mathcal{J}$ is positive, all the spins points to the same direction, giving rise to a non-zero magnetization. This state is known as ferromagnetic [1]. Fig. 1.1 illustrates the different magnetic states discussed.

The magnetic ordering is temperature dependent. The ferromagnetic, antiferromagnetic and ferrimagnetic phases disappear at a certain critical temperature value, below it

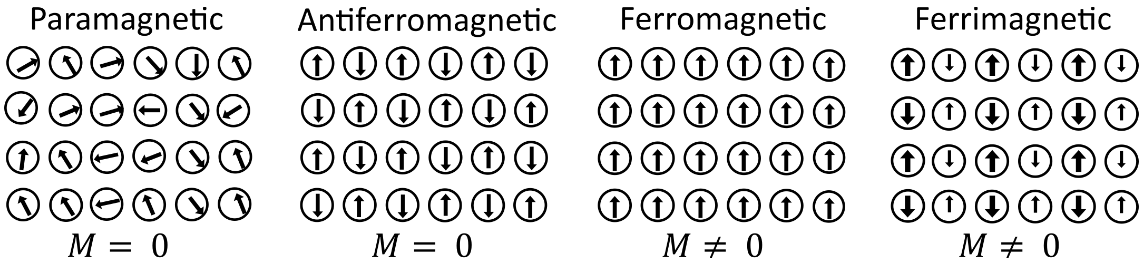

Figure 1.1: From left to right, paramagnetic, antiferromagnetic, ferromagnetic and ferrimagnetic states with their respective magnetization M.

the material keeps its magnetic ordering and above the material becomes paramagnetic. This temperature is known as Curie temperature for ferromagnets and ferrimagnets and as Néel temperature for antiferromagnets.

1.2 Spintronics

Understanding the interaction of the electron's spin in addition to its charge in mesoscopic systems is the main subject of study of spintronics. There are two ways of creating a spin current, either we pass a current through a ferromagnet so the current gets polarized or we generate a pure spin current and as its name indicates, it is a chargeless current where only spin is transferred. The latter does not required a magnetic material for its generation, but a material with a suitable spin-orbit coupling (SOC) value in order to convert the unpolarized charge current into a pure spin current through the spin Hall effect. The ability to create and manipulate spin currents can trigger the development of faster and more energetically efficient devices. The field of spintronics is very promising for the development of novel devices, in applications that goes from data storage, classical and quantum computation, communications, optics, sensing, etc. Key experiments prior the genesis of spintronics, relating ferromagnetism with electrical currents, can be tracked down to 1856 when the magnetoresistance effect was discovered. This effect consist on the change of the electrical resistance of ferromagnets when subjected to an external magnetic field [5].

Other effects include, the detection of a spin polarized current outside a ferromagnetic electrode in 1971 [6] and the tunneling magnetoresistance (TMR) discovered in 1975 [7]. The birth of spintronics is the discovery of the giant magnetoresistance (GMR) in 1988 [8, 9], whose differences from to the already known magnetoresistance, are first, it is several orders of magnitude higher than the latter, and second, it appears in systems with typical dimensions around 50 nm or less. Indeed, for such dimensions the electron's spin play a decisive role in the transport properties of the system as was suggested by Mott in 1936 [10]. The GMR was only achieved after 1988 thanks to the advent of novel fabrication techniques, of particular importance, the molecular beam epitaxy (MBE), that permitted to create multilayers composed of individual layers of just few nanometers [11].

GMR brought an intense research in spintronics, that continue nowadays mainly because of its industrial applications. Important advancements have been made in the growth and nanopatterning of magnetic heterostructures and new physical phenomena have been discovered like the spin-transfer torque, the spin-orbit torque, the spin Hall effect, the spin Seebeck effect, among others, but despite all these advancements, until now (2019) the major contributions have been done in data storage applications like GMR heads, TMR heads and MRAMs. At the same time devices like spin transistors or microwave generators that will certainly revolutionize the electronics remains challenging to realize.

1.2.1 Tunnel magnetoresistance

A magnetic tunnel junction is a spin valve composed by two ferromagnetic films separated by a non-magnetic insulator. It was discovered in 1975 by M. Julliere studying Fe/Ge/Co junctions at low temperatures [7]. He found that the conductance of the system was dependent on the relative orientation of the magnetization of the ferromagnetic films. The relative conductance variation found for this system was about 14% and this effect did not get the attention it deserved during the time it was published. To explain the origin of TMR phenomena, Julliere proposed that this effect was due to the spin polarization acquired by the conduction electrons when interacting with the ferromagnetic metals. In his description it is considered the central idea from Mott's two current model, that considers each spin species as traveling along independent channels [10]. Thus, the relative conductance variation (TMR factor) can be expressed as:

$$TMR = \frac{\varDelta G}{G} = \frac{R_{AP} - R_P}{R_P} = \frac{2P_1P_2}{1 - P_1P_2}, \tag{1.18}$$

with P_α being the spin polarization of the ferromagnet α and defined as:

$$P_\alpha = \frac{D_\alpha^\uparrow(E_F) - D_\alpha^\downarrow(E_F)}{D_\alpha^\uparrow(E_F) + D_\alpha^\downarrow(E_F)}, \tag{1.19}$$

where D_α^σ is the spin σ density of states of the ferromaget α. More accurate models, like the Slonczewski's model [12], include the effects of the tunnel barrier. The polarization in this model is defined as:

$$P = \left(\frac{k_{F\uparrow} - k_{F\downarrow}}{k_{F\uparrow} + k_{F\downarrow}}\right)\left(\frac{\kappa_0^2 - k_{F\uparrow}k_{F\downarrow}}{\kappa_0^2 + k_{F\uparrow}k_{F\downarrow}}\right), \text{ where} \tag{1.20}$$

$$\kappa_0 = \pm\sqrt{\frac{2m}{\hbar^2}(U - E_F)}. \tag{1.21}$$

$k_{F\uparrow}$ ($k_{F\downarrow}$) is the Fermi wavevector of the spin up (down) bands and U is the barrier height. These new equation is obtained when the band structure details of the ferromagnets are taken into account, as well as, the height of the barrier.

The discovery of GMR in 1988 brought back attention to the TMR phenomena and thanks to the 20% value found at room temperature in CoFe/Al_2O_3/Co MTJ in 1995 by Moodera et al. [13], the research on TMR became very active. In 2001 it was predicted that employing of MgO barriers in the magnetic tunnel junctions (MTJ's) could improve the performance of these devices [14, 15], what attracted a lot of attention, mainly because of its potential applications. In 2004 it was achieved an important breakthrough when was found a TMR value of around 200% at room temperature in a single-crystal of Fe/MgO/Fe [16, 17]. Since then, these TMR values have progressively improved and nowadays it can be find values up to 500% at room temperature and 1000% at 5 K can be found [18].

1.2.2 Giant magnetoresistance GMR

Let us consider a spin valve, that is, a multilayered ferromagnetic system, composed by two metallic ferromagnets separated by a non-magnetic metal, whose relative magnetizations are collinear (parallel or antiparallel) with one magnetic layer easier to switch. If a current is applied in the system and its resistance is measured as a function of the relative magnetic orientation of the magnetic layers, a drastic change in the resistance is observed. This was simultaneously found by the groups of A. Fert [8] and P. Grünberg [9] in Fe/Cr and Fe/Cr/Fe multilayer structures. This system presents a higher resistance when the magnetization of the adjacent layers was antiparallel as is shown in Fig. 1.2.

In the following two subsections theories explaining differences in conductances between parallel and antiparallel configurations are presented in the framework of the two-current model.

1.2.3 Two-current model

This model was developed by Sir Nevill Mott in 1936 to explain the electrical conductivities found in transition metals and their alloys, where the spin plays an important role in their transport properties [10, 19]. It is useful for understanding the GMR and TMR phenomena. In this model it is considered that the current inside a system is carried by two independent spin channels and the spin flip effects are disregarded. This approximation is valid for materials with small atomic number, because with a high atomic number, the Coulomb field increases what could lead to a relativistic effect that couples the electron's spin with the orbital angular momenta known as spin-orbit coupling [20]. Let us consider that a current is applied to a system, this current carry both up and down spin contributions, so the total current density can be written as:

$$\mathbf{J} = (\sigma_\uparrow + \sigma_\downarrow)\boldsymbol{E}, \tag{1.22}$$

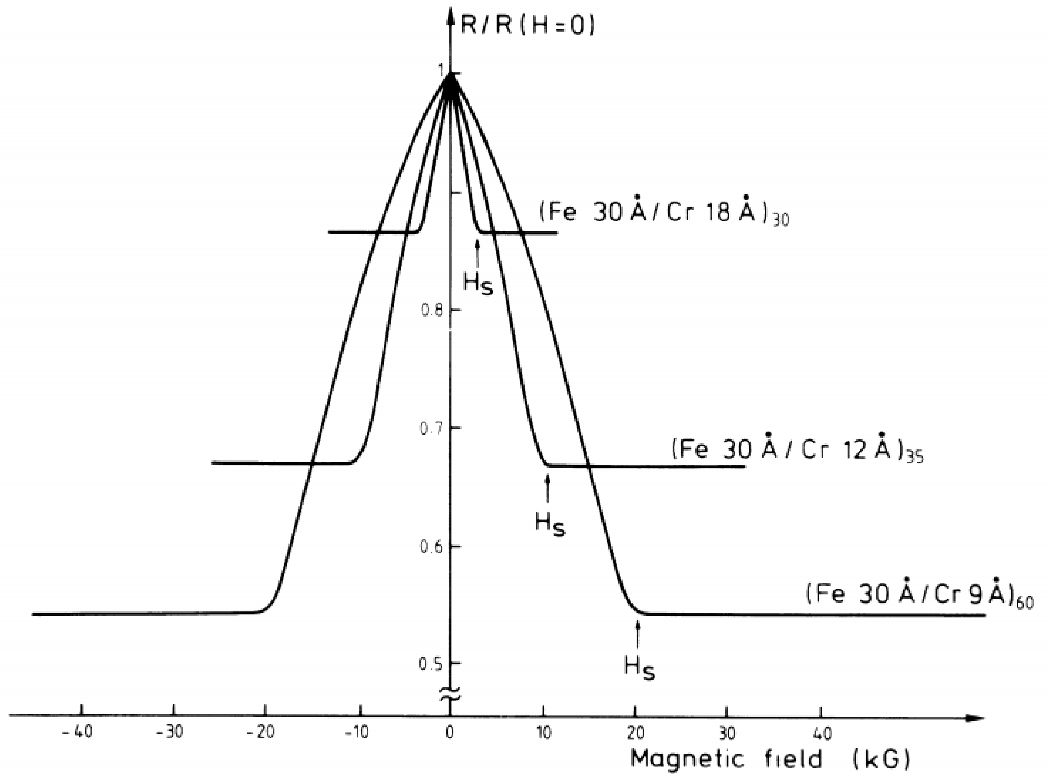

Figure 1.2: Magnetoresistance of three Fe/Cr superlattices at 4.2 K. Figure taken from Ref. [8].

where $\sigma_\uparrow$ and $\sigma_\downarrow$ are the conductances in the up and down channels, respectively. Remembering that the electric field is defined as the potential difference per distance units $|\boldsymbol{E}| = \Delta V/t_d$, and using Eq. (1.22), we have:

$$I = (\sigma_\uparrow + \sigma_\downarrow)\frac{A\Delta V}{t_d}, \tag{1.23}$$

where A is the transverse area and t_d the thickness. The expression for the resistance is then obtained:

$$R = \frac{\Delta V}{I} = \frac{1}{(\sigma_\uparrow + \sigma_\downarrow)\frac{A}{t_d}} = \frac{1}{\frac{1}{R_\uparrow} + \frac{1}{R_\downarrow}} = \frac{R_\uparrow R_\downarrow}{R_\uparrow + R_\downarrow}, \tag{1.24}$$

which is the well-known expression for the parallel resistor configuration. This permits to represent the difference in the resistance for the parallel and antiparallel magnetic orientation with a circuit whose resistances are arranged in parallel as illustrated in Fig. 1.3. The resistances $r/2$ and $R/2$ are defined for the majority and minority spin channel respectively, with $r < R$. Note that in Fig. 1.3(a) for the parallel case, the resistance in the spin up channel has the lowest possible value r, while in the spin down channel the electrons experience the highest resistance R. So, the total resistance for this magnetic configuration, with $R_T^{-1} = 1/R_1 + 1/R_2$, as:

$$R_P = \frac{Rr}{R + r}. \tag{1.25}$$

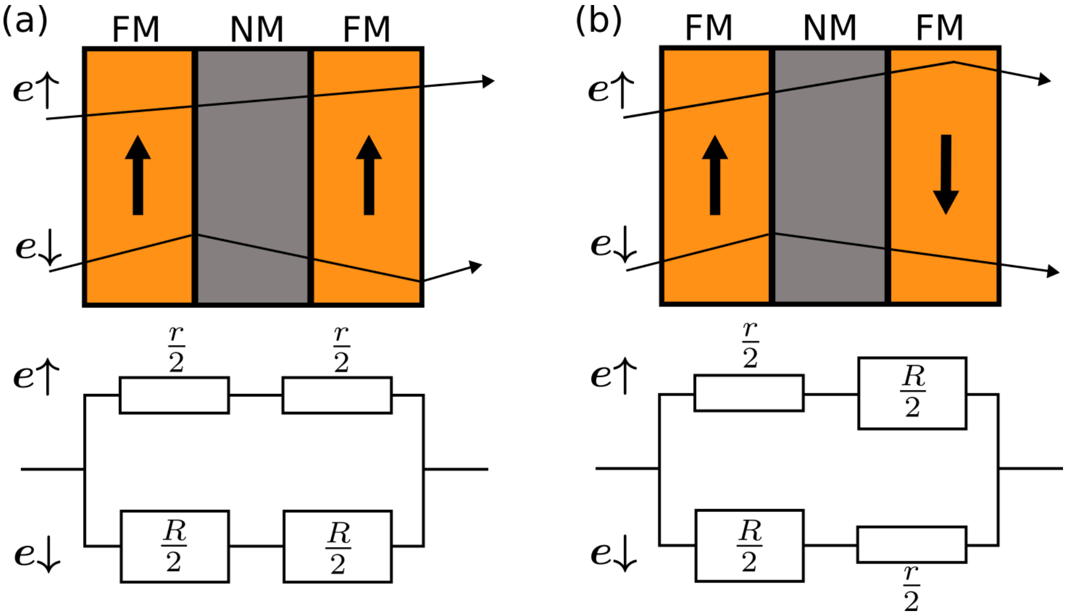

Figure 1.3: Schematic representation of a spin valve with its respective two current model in (a) parallel magnetic configuration and (b) in antiparallel magnetic configuration. The spin valves are composed by two ferromagnets (FM) separated by a non-magnetic material (NM).

For the antiparallel magnetic configuration, Fig. 1.3(b) shows that both spin channels have the same resistance $(r + R)/2$, so we get that the resistance in this configuration is:

$$R_{AP} = \frac{R + r}{4}, \tag{1.26}$$

and the GMR can be written then:

$$GMR = \frac{R_{AP} - R_P}{R_P} = \frac{(R - r)^2}{4Rr} \tag{1.27}$$

Looking at the values of R_{AP} and R_P it is not straightforward to see that $R_{AP} > R_P$, so let us demonstrate it. By contradiction

$$\begin{aligned} \frac{R + r}{4} &< \frac{Rr}{R + r} \\ (R + r)^2 &< 4Rr, \text{ so} \\ (R - r)^2 &< 0, \end{aligned} \tag{1.28}$$

what is impossible because any squared real number is bigger than zero, so $R_{AP} > R_P$.

1.2.4 s-d model

This model describes the interaction of conduction electrons with the magnetization of metallic ferromagnets [21]. It assumes that scattering with defects does not flip the electron's spins and the spin orientation is preserved. In addition, it considers the electrons in the d band as magnetized and localized to the crystal lattice sites, thus their contribution to electronic transport is negligible, while the s (p) electrons are considered delocalized and responsible for conductance [22]. Electrons from both band "types" interact with each other via exchange field. In this situation, an external magnetic field $\boldsymbol{\mathcal{H}}$ couples mainly with the spins of the d band electrons, then we can write for the delocalized s electrons the exchange interaction as:

$$H_{sd} = -\frac{J_{sd}}{2M_s}\boldsymbol{M}(\boldsymbol{r}) \cdot \boldsymbol{\sigma}, \tag{1.29}$$

where J_{sd} is the splitting of the spin up and spin down sub-bads of the d bands, M_s saturation magnetization and $\boldsymbol{M}(\boldsymbol{r})$ is the magnetization of the d band electrons. Ferromagnetism is understood is this model as follows. Due to exchange splitting the d band splits and as a consequence, depending on the Fermi energy position (if it intersects one or both d sub-bands), one of the sub-bands will have more electrons than the other, creating an unbalance of spin species, driving to the more energetically favorable, magnetic ordered state. The density of states in ferromagnets is schematically depicted in Fig. 1.4.

1.3 2D materials in spintronics

Graphene was the first truly 2D material synthesized in history. Followed by the realization of other 2D materials. These materials are usually allotropes of various elements compounds and are obtained after the isolation of a single atomic layer. Examples of such materials include hexagonal boron-nitride (hBN), silicene that is a silicon allotrope, germanene, an allotrope of germanium and phosphorene, an allotrope of phosphorus. Other 2D materials include the transition metal dichalcogenides (TMDCs), which are semiconducting materials of the type MX_2, where M could be a transition metal atom and X is a chalcogen, so TMDCs monolayers include molybdenum disulfide (MoS_2), Tungsten disulfide (WS_2), molybdenum diselenide ($MoSe_2$), among others.

Most of these materials have promising applications in spintronics, for example, graphene's high electron conductivity, weak spin-orbit coupling, long spin relaxation time and length up to room temperature, offers an optimal platform for spin manipulation. The 2D TMDCs, due to their unique spin-valley coupling provides and extra degree of freedom to manipulate spins [24, 25]. Silicene, germanene and 2D TMDCs, are serious candidates to display quantum spin Hall effect (QSHE) [25].

In addition to being able to induce ferromagnetism, spin-orbit coupling in 2D materials

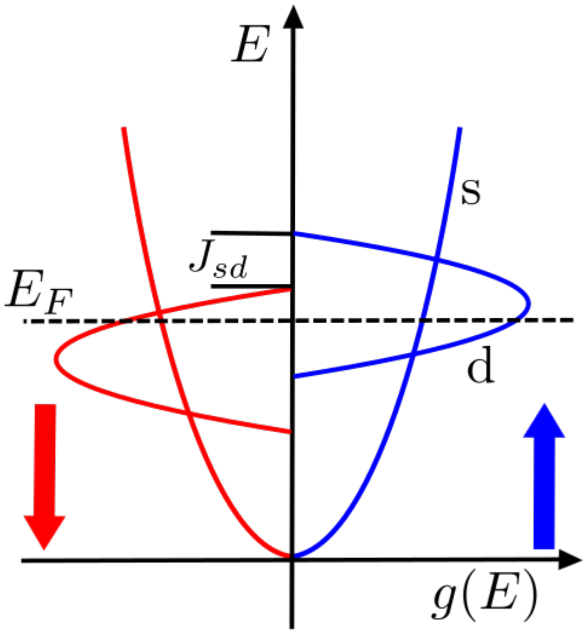

Figure 1.4: Scheme of the spin dependent bands in the s-d model. The figure shows the density of states g(E) in ferromagnets. E_F is the Fermi energy, the d bands are splitted by a factor J_{sd} and the s bands remains unchanged. The spin majority and spin minority in this illustration corresponds to the spin up and spin down respectively. Figure adapted from Ref. [23].

is fundamental to manipulate spin currents on them. In the next subsection we will describe spin-orbit coupling phenomenon.

1.3.1 Spin-orbit coupling (SOC)

The SOC is a relativistic effect that couples the electron's spin with its spatial motion. To have a clearer picture of what is going on, let us consider a system with SOC under the presence of an electric field with no external magnetic field applied. The electrons of the system will move because of the influence of the electric field and due to SOC are going to experience, a magnetic field in their frame of motion, that couples with their spin [26]. The presence of SOC in physical systems is a key ingredient for the emergence of a great variety of phenomena, like the magnetocrystalline anisotropy or the spin Hall effect. Likewise, it is important for the spin manipulation, as well as, the generation and detection of pure spin currents.

The impact of SOC on the band structure of either an atom or a crystalline lattice is a splitting in the bands or a shift of them. Despite this similar feature, the physics of both systems is quite different. In an atom the coupling happens between the electron's spin and the atomic orbital and can described by $\mathbf{L}\cdot\mathbf{S}$, where $\mathbf{L}$ is the angular momentum and $\mathbf{S}$ is the electron's spin. In a crystal the SOC happens between conduction electrons and the lattice potential. SOC only happens in crystals that intrinsically exhibit an

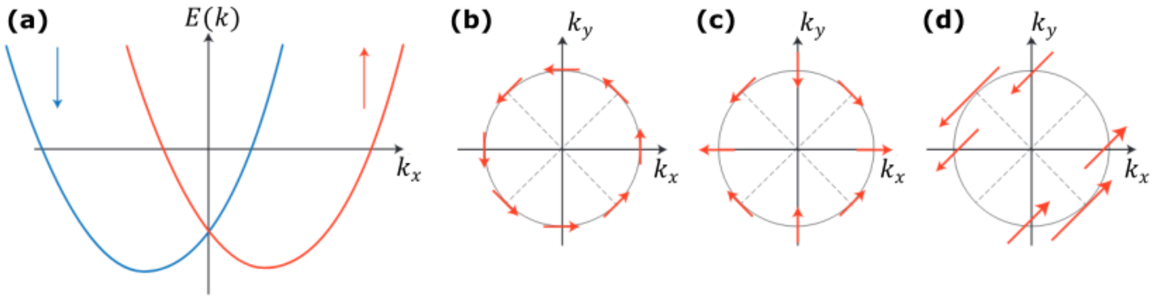

Figure 1.5: (a) Schematic of the energy dispersion of a 1D free electron gas in the presence of either Rashba or Dresselhaus type SOC. The red and blue parabolas indicates how were the spin bands before "turning on" the SOC interaction. Spin texture at the Fermi surface when is present Rashba SOC (b), Dresselhaus SOC (c) and when both are present with equal magnitude (d). Figure adapted from Ref. [26].

asymmetric lattice potential, due to its structure. Fig. 1.5(a) shows a schematic of the energy dispersion of a 1D electron gas in the presence of SOC, where it is clearly seen the shifting in the bands due to SOC. There are two ways structural characteristic can give rise to SOC, either the crystal has an uniaxial symmetry, like wurtzite, or is composed by the junction of two different crystals that creates an spatial inhomogeneity right at the interface, in which case the SOC displayed will be of Rashba type [27] or the crystal is non centro-symmetric, in whose case the SOC displayed will be of the Dresselhaus type [28]. The corresponding spin texture of both types are presented in Fig. 1.5(b) and (c) respectively. Fig. 1.5(c) shows the spin texture when both SOC effect are present and have the same magnitude. In this thesis, due to the nature of our system we will consider only SOC of the Rashba type.

1.3.2 2D materials in spintronic devices

There are basically two architectures in which a spintronic device can be arranged, vertically and laterally. In this subsection we will discuss these two configurations and their applications using 2D materials.

Vertical devices are characterized by the vertical stacking of two ferromagnets separated by a non-magnetic spacer. Spin valves in this configuration can have two different geometries depending on how is wanted the current to be applied into the system, current in plane (CIP), in which the current flows parallel to the interface of the layers as shown Fig. 1.6 (a), and current perpendicular to plane (CPP), where the current flows perpendicular to the plane of the layers as shown in Fig. 1.6(b). In both geometries, interfacial scattering plays a dominant role in transport for small layer thicknesses, even though, it is possible to create systems where the bulk effects are dominant, but this evidently requires larger layer thicknesses [19]. The main applications with 2D materials using CPP configuration are the spin filters and spin valves where it has been studied materials such

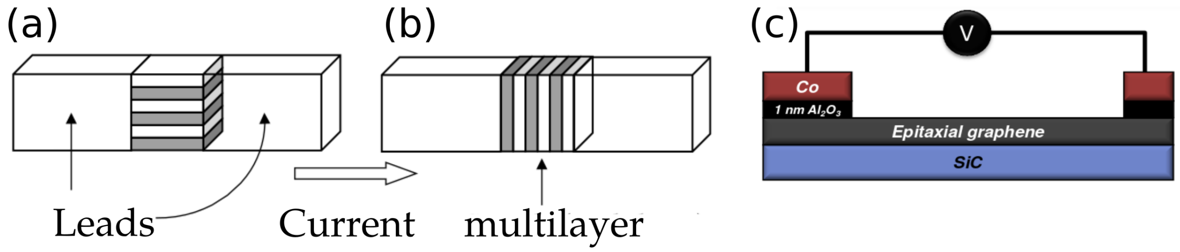

Figure 1.6: (a) Vertical spin valve in CIP configuration. (b) Vertical spin valve in CPP configuration. (c) Spin valve in lateral configuration. Figure adapted from Refs. [19] and [36].

as graphene [29–31], TMDCs and a combination of hBN with graphene [32, 33]. Also, it has been demonstrated the possibility to control electrically the magnetoresistance of a magnetic tunnel junction which uses graphene as spacer as reported in Ref. [34].

In lateral devices the two ferromagnets are separated laterally, as is shown in Fig. 1.6(c). Among its advantages, there is the generation of pure spin currents, which is impossible to achieve in vertical structures, because in this configuration the spin current cannot be completly uncoupled from the charge current [19]. Also, the lateral configuration is more suitable to study spin relaxation, via Hanle measurements for instance, due to the fact that this setup permits optical access to the non-magnetic spacer region [19]. The use of 2D materials in this configuration opens new opportunities for the study of novel spintronic devices. Indeed, spin propagation and spin detection in graphene has already been studied using this configuration experimentally, as in Ref. [35] or Ref. [36]. This is the configuration we considered for our investigations, without injecting electron current through the ferromagnets.

1.4 Graphene spintronics

1.4.1 Graphene

Graphene is a 2D material composed of carbon atoms arranged in a honeycomb lattice. Close to the Fermi level, it has a linear dispersion energy characteristic of massless Dirac fermions. It has no gap and the valence and conduction bands touch each other in only one point known as Dirac point. Graphene can be considered as a semiconductor of zero gap, whose lowest energy particles have relativistic behavior. It was synthesized for the first time in 2005 in Manchester by Andre Geim and Konstantin Novoselov and brought with it a real 2D materials revolution. Graphene has a very high charge mobility, for example when encapsulated in hexagonal boron nitride (hBN) it can reach 3×10^6 $cm^2/(Vs)$ [37], a weak spin-orbit coupling [35, 36, 38–45] and a long spin relaxation time and lengths even at room temperature. These physical properties among others have attracted a lot of interest in view of its potential applications in diverse fields such as electronics, spintronics and quantum computing [46–48].

Graphene properties

Carbon is part of IV group and has four valence atoms. Carbon has the following electronic configuration: $1s^2\ 2s^2\ 2p^2$, where the p orbital is partially filled. When graphene is formed, the s and p orbitals hybridize, giving rise to three sp^2 orbitals, that results in σ bonds, which are the strongest type of covalent bond. The remaining $2p_z$ electrons, are weakly bound to the carbon atoms and can be considered as delocalized [49]. These electrons play an important role in the high conductivity of the material.

In graphene the carbon-carbon length is approximately $a_{CC} \approx 1.42$ Å and its Bravais lattice has two atoms per basis, so the unit cell has two p_z electrons, that contribute to the electronic properties of graphene. In Fig. 1.7 are shown the vectors that form its unit cell, whose values are:

$$a_1 = \left(\frac{a}{2}, \frac{\sqrt{3}a}{2}\right), \qquad a_2 = (a, 0)\,, \tag{1.30}$$

being $a = \sqrt{3}a_{CC}$. Each carbon atom has 3 nearest neighbors, whose vectors are given by:

$$\delta_1 = \left(0, \frac{a}{\sqrt{3}}\right), \qquad \delta_2 = \left(\frac{-a}{2}, \frac{-2a}{\sqrt{3}}\right), \qquad \delta_3 = \left(\frac{a}{2}, \frac{-2a}{\sqrt{3}}\right) \tag{1.31}$$

The reciprocal vectors can be obtained using the formula $A = B \cdot (B^T \cdot B)^{-1}$, where B is a matrix whose columns are the lattice vectors and A is a matrix that describes the dual lattice (reciprocal space). So,

$$b_1 = 2\pi \left(0, \frac{2}{\sqrt{3}a}\right), \qquad b_2 = 2\pi \left(1, \frac{-\sqrt{3}}{3a}\right) \tag{1.32}$$

The graphene energy dispersion will be derived in detail in section 2.2, but let us briefly introduce it and discuss its properties. The energy dispersion is given by the following expression:

$$E(k_x, k_y) = \pm t\sqrt{1 + 4\cos\frac{\sqrt{3}a}{2}k_x \cos\frac{a}{2}k_y + 4\cos^2\frac{a}{2}k_y}, \tag{1.33}$$

where $t = 2.7\ eV$ is the graphene hopping parameter and k_x and k_y are moment values inside the First Brillouin zone. Using Eq. (1.33) we plotted the band structure shown in Fig. 1.8. The zoom highlights the linear behavior of the bands close to the K points. In fact, this characteristic is the most striking feature of graphene. Because of this, the electrons in graphene behave as relativistic particles and as a consequence for example, its quantum Hall effect is different from that one measured in 2D gases. For example, it has

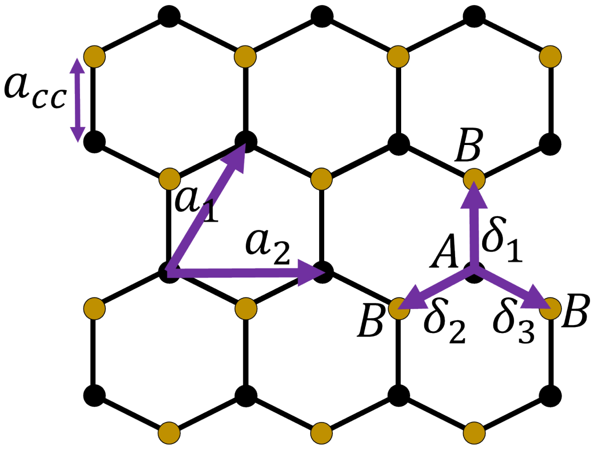

Figure 1.7: Honeycomb graphene lattice showing the primitive vectors a_1 and a_2 and the nearest neighbor δ_1, δ_2 and δ_3.

a zero Landau level and its cyclotron mass depends on the square root of the electronic density [46], and its charge carriers can tunnel an infinite potential barrier with perfect transmission due to the Klein tunneling [50]. From the Hamiltonian of Eq. (2.11) it is possible to get the Dirac equation for energies close to the K points. Without loss of generality, let us consider the K point with coordinate $\left(0, \frac{4\pi}{3a\sqrt{3}}\right)$ to do so, let us write the corresponding Hamiltonian operator of the eigenenergies from Eq. (2.11)

$$H(k_x, k_y) = t \begin{pmatrix} 0 & f(k_x, k_y) \\ f^*(k_x, k_y) & 0 \end{pmatrix} \tag{1.34}$$

where $f(k_x, k_y)$ is defined as:

$$f(k_x, k_y) = e^{-ia(k_x)} + 2e^{\frac{ia(k_x)}{2}} \cos\left(\frac{\sqrt{3}a}{2} a(k_y)\right). \tag{1.35}$$

Because we are interested to get the energy dispersion close to the chosen K point, let us consider the following:

$$f(q_x + K_x, q_y + K_y) = e^{-ia(q_x+K_x)} + 2e^{\frac{ia(q_x+K_x)}{2}} \cos\left(\frac{\sqrt{3}a}{2} a(q_y + K_y)\right),$$

with $K_x = 0, K_y = \frac{4\pi}{3a\sqrt{3}}$ and $q_x, q_y << 1$. Rewriting this equation using the identity $\cos(a+b) = \cos(a)\cos(b) - \sin(a)\sin(b)$ we get

$$f(k_x, k_y) = e^{-ia(q_x+K_x)} + 2e^{\frac{ia(q_x+K_x)}{2}} \cos\left(\frac{\sqrt{3}a}{2}(0)\right) \cos\left(\frac{\sqrt{3}a}{2}\left(\frac{4\pi}{3a\sqrt{3}}\right)\right) - \sin\left(\frac{\sqrt{3}a}{2}(0)\right) \sin\left(\frac{\sqrt{3}a}{2}\left(\frac{4\pi}{3a\sqrt{3}}\right)\right),$$

approximating the functions for small values and keeping those of order smaller than 2 we get

$$
\begin{aligned}
&= (1 - iaq_x) + 2\left(-\frac{1}{2}\left(1 + \frac{iaq_x}{2}\right) - \frac{3}{4}aq_y\right)\\
&= -\frac{3a}{2}(iq_x + q_y), \text{ so the new Hamiltonian can be written as:}\\
H(k_x, k_y) &= -\frac{3at}{2}\begin{pmatrix} 0 & iq_x + q_y \\ -iq_x + q_y & 0 \end{pmatrix} = -\frac{3at}{2\hbar}\boldsymbol{\sigma}\cdot\boldsymbol{p}, \qquad (1.36)
\end{aligned}
$$

which is the Dirac equation, probing the relativistic nature of the electrons close to the K points.

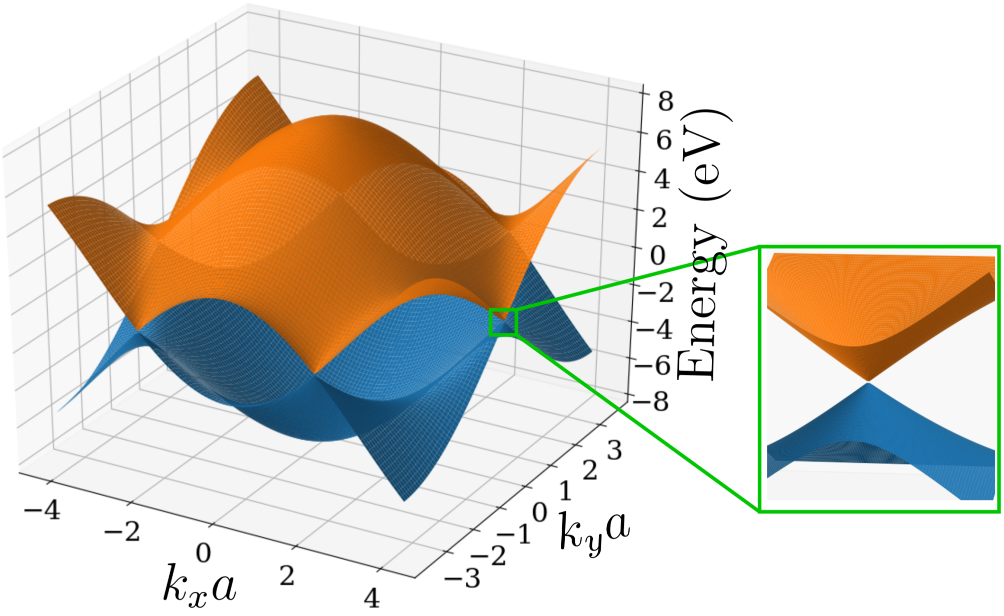

Figure 1.8: Band structure of graphene showing the six Dirac points. The inset zooms one Dirac point showing the linear dispersion of the bands close to it. Figure obtained by plotting Eq. (1.33)

Graphene edges

It is well-known that the edge terminations of graphene nanoribbon (GNR) affects the electronic properties of graphene. The most common edge terminations are the armchair and zigzag types. The GNR with armchair edges displays insulating or metallic behavior depending on graphene nanoribbon (GNR) width [51, 52], while the GNR with zigzag edges can show half-metallicity, due to the antiferromagnetic interaction of the edges [53]. If a cut is performed in a graphene GNR at an intermediate angular direction between these high symmetric cases (armchair and zigzag), this edge will be characterized by a chirality angle θ [54] and as a function of its value the band structure will change. In Fig.

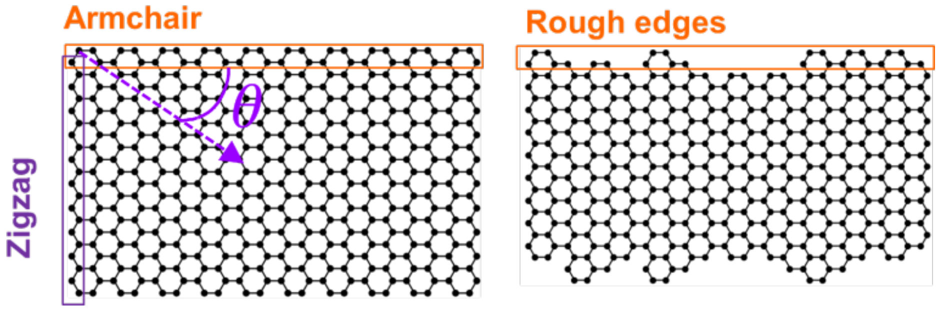

Figure 1.9: (a) GNR nanoribbon showing armchair and zigzag edges. The angle θ shows the new edge termination obtained doing a cut at this particular angle. (b) GNR with rough edges.

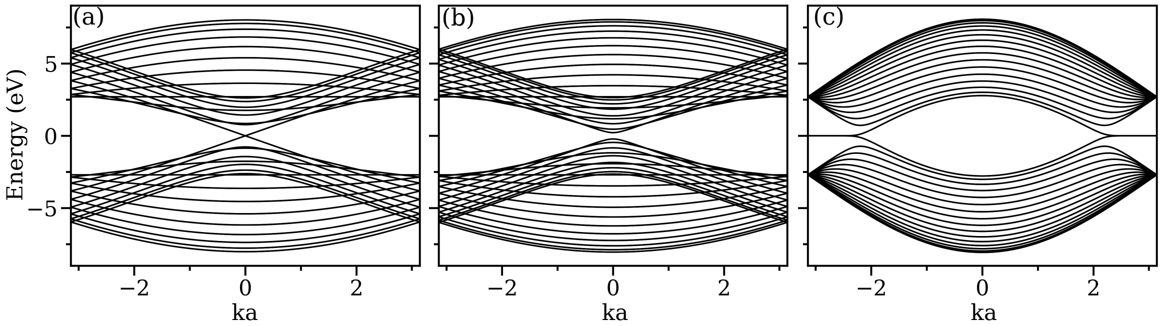

Figure 1.10: Band structure for (a) a metallic armchair GNR of width N=17 (1.97 nm) (b) a semiconducting armchair GNRs of width N=21 (2.46 nm). (c) zigzag GNR of width N=32 (3.44 nm). The band structures were obtained by using Kwant.

1.9(a) it is depicted the edge termination of the already discussed edges. If $\theta = 30°$ the GNR will have zigzag edges, otherwise if $\theta = 0°$ the GNR will have armchair edges.

The effects of the armchair and zigzag edges in a GNR on its band structure are shown in Fig. 1.10(a) and (b) both show the band structure of an armchair GNR. It is well-known that the number of atoms across the armchair GNR width determines its electronic behavior. If the number of atoms N follows the formula $N = 3 * p + 2$, where p can be any integer number, the armchair GNR is metallic like (a), otherwise it is semiconducting [55] like (b). The zigzag GNR electronic behavior does not depend on its width and is always metallic. Its band structure is shown in Fig. 1.10(c).

It is very difficult to have a GNR with perfect edges in the laboratory. Because defects change the edge format, they can also affect the electronic properties of graphene. Among the defects at the edges one can find vacancies, impurities, etc. In Fig. 1.9(b) it is shown a GNR with vacancies in its edges, for which it has been demonstrated a decrease in the charge conductance of the GNR like in Ref. [56] or can exhibit a nonzero spin conductance as reported in Ref. [57].

1.4.2 Applications of graphene in spintronics

Graphene is a diamagnetic material, so in order to make it useful in spintronics one needs to find methods to induce a ferromagnetic order in it. There have been several methods to achieve this, for example functionalization with adatoms, a process that consist on adding extra atoms of a particular species on the graphene surface [58]. Of particular interest is the hydrogen functionalization of graphene, for which it have been demostrated the presence of ferromagnetism, as a consequence of the interaction of the localized states of the hydrogenated graphene and the silicon dangling bonds of the bottom buffer layer [59]. The addition of defects, either vacancies or impurities, is another method that has been explored recently, in order to induce ferromagnetism on graphene [60–62]. Experimentally, the addition of defects can be achieved by means of lithography or by bombardment with electrons. Inducing magnetism by proximity effects via an adjacent ferromagnet, has been also explored [63–68]. The mechanism behind this effect is the hybridization between p_z orbitals in graphene with those of the neighboring substrate. In addition to inducing magnetism, proximity effects can lead to superconductivity, SOC strength enhancement and even induce topological properties. The advantage of inducing a ferromagnetic ordering by proximity effects over aforementioned methods, lies in the fact that it is more robust and less invasive, i.e. it is not necessary to change the lattice structure that can result in a reduction of the electronic conductivity or an unwanted increase of the SOC.

Applications and prospectives of graphene in spintronics range from spin devices, like spin transistors, spin interconnects; storage devices like hard disks, magnetic random access memory (MRAM) to optical devices like lasers [69, 70]. Beyond the aforementioned applications, there is opportunity to find new physical effects combining graphene with other 2D materials, new topological phases inducing SOC on graphene to have quantum anomalous Hall effect (QAHE), or doping the system to obtain high temperature robust spin Hall effect (SHE), that can be used to generate pure spin current [25]. These effects could be used for the design of new device concepts not only in spintronics, but in other fields as well.

1.5 Motivation

In the near future the capacity of our integrated circuits will reach a technical limit imposed by physics. Spintronics aims to find a solution to circumvent this problem, but there are still many challenges to overcome towards the realization of a fully spintronic device, despite the numerous applications already developed, like hard disk memories or magnetic random-access memories (MRAM). Thus, further investigations are required in order to find materials with relevant spin-dependent properties like spin lifetime and spin diffusion length. Transport measurements performed on graphene and some metals, like Cu, Ag, Al and some semiconductors like Si, GaAs, and Ge have demonstrated the superiority of the former over the mentioned materials [71]. Even more astonishing is the fact that graphene preserves its high spin lifetimes and long spin diffusion lengths even at room temperatures, what converts it in a suitable platform for spin control and for the development of novel devices. Even though, the graphene's advantages are well-known, it remains a challenge finding ways to enhance its SOC, necessary for spin manipulation, while keeping the efficiency and robustness of spin polarization.

1.6 Objectives and contributions

With the aim of studying in detail the magnetoresistance phenomena in graphene-based spin valves, in this thesis we propose a device composed of a graphene nanoribbon and two identical magnetic stripes that induce magnetism in graphene by proximity effects. A systematic study is performed, changing the material type of the magnets. Four different magnetic insulators (MI), as well as, one multiferroic material, are used as magnetic inductors. In addition, we study the physics of the spin transfer torque (STT) when considered a non-collinear magnetic configuration in the proposed spin valve. Uncovering the physics of the studied phenomena can lead to the development of new devices and the improvement of existing ones.

In Chapter 2 we briefly review the density functional theory (DFT) and the tight-binding approach. Then we apply the tight-binding technique to graphene and present the Hamiltonian of our system. Later, the transport formalism is review focusing on the scattering matrix method. Finally, we introduce the main observables studied in this thesis. In Chapter 3, we address the physics of spin transport in the aforementioned graphene-based spin valve. We demonstrate the existence of proximity magnetoresistance phenomena (PMR) generating spin current polarization without direct injection through the ferromagnet and present promising results on its robustness. In addition, we explore the control of spin currents via the ferroelectrical properties of multiferroic magnets. We show that besides PMR it is possible to define new effects, i.e. proximity electroresistance (PER) and proximity multiferroic resistance (PMER), that are of vital importance for clarifying the role of the electrical polarization in the tuning of the magnetic proximity effects in graphene-based spin valves with multiferroic BFO. In Chapter 4, we give a brief introduction of the spin transfer torque (STT) phenomena and present a derivation of the spin conservation equation in the steady state when the system's Hamiltonian has spin dependent hoppings and spin dependent sublattice potential as in our case. With this model in hand, we proceed to study the transport in the proposed graphene-based spin valve with magnets made of YIG in non-collinear magnetic configuration. We identify four typical energy zones of big importance for the understanding of the STT behavior. Also, we investigate the dependence of STT with respect to the size of the system and present an estimation of the order of magnitude of the critical current, which is the current needed to switch the magnetization of the immediate graphene region in contact with the magnet, that for suitable thicknesses may eventually switch the magnetic orientation of the whole magnet. In Chapter 5, we present our conclusions and perspectives.

CHAPTER 2

Theory and methodology: tight-binding quantum transport formalism

The size of a system determines the properties it can display. Saying so, we can divide physical systems into three different regimes depending on their size, namely macroscopic, mesoscopic and nanoscopic. There is not consensus on the exact dimensions defining these regimes, but it is widely accepted that macroscopic systems can include systems as large as galaxies (10^{21} m) and as small as bacteria (10^{-6} m), while nanoscopic system as its name indicates are systems whose size is of the order of few nanometers, comparable to the size of atoms. Systems in the mesoscopic regime are larger than atoms but still are small enough to be affected by quantum effects. As its name indicates it is an intermediate regime. Systems in this regime comprise few hundreds of atoms, so their typical sizes are about 100 nm. Examples of these systems are transistors, genes and viruses. The access to mesoscopic and nanoscopic systems was achieved thanks to great progress in experimental techniques in recent decades. Being able to control matter at atomic scale, made available phenomena that before were simply disregarded or unknown. The need for understanding mesoscopic systems led to new theoretical techniques to properly treat them.

There are several tools to study mesoscopic and nanoscopic systems, and their applicability depends on the characteristic length scales of the system. Among the analytical tools to simulate mesoscopic systems, there are the *ab initio* methods, like density functional theory (DFT), quantum Monte Carlo (QMC) or the Hartree-Fock methods, that derive the physical behavior of a system from first principles. Other approaches include semi-empirical methods in which empirical potentials are fitted from experimental data to describe accurately systems. When the required properties of a material are obtained

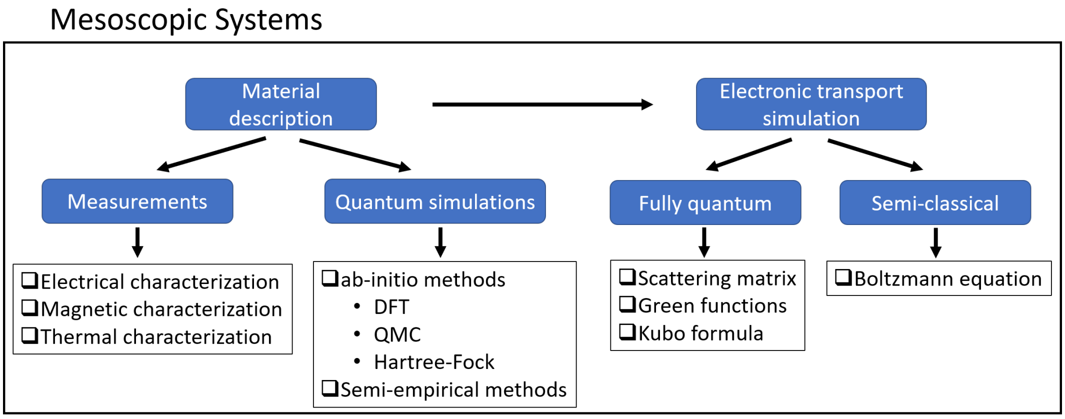

Figure 2.1: Hierarchy tree showing the steps that preceded the transport phenomena study done in this thesis. In this work it was fitted the band structure obtained from DFT calculations in order to obtain parameters that permitted the study of the transport properties of a lateral spin valve using the scattering matrix method.

(band structure, phase transition diagrams, etc), prototypical devices using this material can be designed and investigated. A hierarchy tree presenting the process of theoretical description of devices is presented in Fig. 2.1.

In this thesis we systematically investigated the transport phenomena of a spintronic device. For the description of transport phenomena of mesoscopic spintronics systems, it is of vital importance five characteristic lengths: the mean free path, the de Broglie wavelength, the phase relaxation length, the spin coherence length and the (Larmor) spin precession length. The mean free path ℓ is the distance traveled by an electron before it collide, the de Broglie wavelength defined as $\lambda_F = h/p$ relates the particle wavelength to its momentum p. This quantity naturally rises from the wave-particle duality. Systems whose size is comparable with this quantity present quantum effects, so they should be treated with quantum methods [72, 73]. The phase-relaxation length ℓ_ϕ is the distance for which the electron waves conserve their coherence. Processes that can cause phase relaxation (coherence loss) are those that break the time-reversal symmetry, like magnetic fields, or inelastic collisions. Finally, when the transverse spin current is not fully absorbed by the system, like in the current driven domain wall motion, or the spin transfer torque decays while oscillating [74] the spin coherence length $\ell_\perp$ and precession length ℓ_L become essential for the understanding of that phenomena. Physically, $\ell_\perp$ represents the transverse spin accumulation decay length and ℓ_L the transverse spin accumulation traveled distance while precessing inside a ferromagnet [75].

Systems whose phase-relaxation length is bigger than their size L, $\ell_\phi >> L$, Green function methods, scattering matrix and Kubo formula are applicable. If the de Broglie wavelength is smaller than the mean free path and the phase-relaxation length is smaller than the system, it is $\lambda_F << \ell$ and $\ell_\phi << L$, the description of the system via Boltzmann equation is more suitable [73]. In this chapter I will derive all the theoretical tools necessary to investigate the spin dependent transport and the spin transfer torque.

2.1 Density functional theory (DFT)

In this section we will describe briefly the theoretical basis of the DFT. The DFT is a powerful formalism used in chemistry, physics and materials science to model many-body systems. It aims to solve the Schrödinger equation by employing a mean field approximation including several particle interaction in a term called exchange-correlation potential, that will be described with more detail later. With DFT it can be handled reasonable large systems in shorter time when compared with other quantum methods. For its development Walter Kohn earned the Nobel prize in chemistry in 1998. DFT is based on two theorems known as Hohenberg-Kohn theorems [76], that states the following:

- The ground state energy of a system is a unique functional of the electron density

$$E_0 = E[\rho]$$

- When $E[\rho]$ reach the minima, the electron density corresponding to this energy minima is the true electron density of the ground state from the Schrödinger equation of the system.

The first theorem permits to replace the wave function of N particles with $3N$ degrees of freedom by the electronic density, decreasing the number of degrees of freedom to 3. The second one implies that while minimizing the energy of the system with respect to the electronic density, we get at the end the exact solution of the ground state of the Schrödinger equation. The trick to minimize the functional $E[\rho]$ is to solve the following auxiliary equation, known as Kohn-Sham equation:

$$\left[\frac{-\hbar^2}{2m}\nabla^2 + V_{eff}\right]\phi_i(\boldsymbol{r}) = \epsilon_i\phi_i(\boldsymbol{r}), \tag{2.1}$$

where ϵ_i and $\phi_i(\boldsymbol{r})$ are the eigenenergies and eigenfunctions of the non interacting system. Another useful quantity is the following:

$$\rho(\boldsymbol{r}) = \sum_i^{occ} |\phi_i(\boldsymbol{r})|^2, \tag{2.2}$$

which is the the sum of the squared Kohn-Sham eigenfunctions. This quantity is known as Kohn-Sham electron density. Similarly to what happens with the Kohn-Sham eigenfunctions this expression lacks of physical meaning, but in this case, this quantity do reproduce correctly one physical quantity, the ground state electron density. The effective potential

V_{eff} Eq. (2.1) can be written as [77]:

$$V_{eff}(\boldsymbol{r}) = V(\boldsymbol{r}) + e^2 \int \frac{\rho(\boldsymbol{r}')}{|\boldsymbol{r} - \boldsymbol{r}'|} d\boldsymbol{r}' + V_{xc}(\boldsymbol{r}), \tag{2.3}$$

The first term $V(r)$ is an external potential, the second one is the Hartree potential, that takes into account the Coulomb repulsion and the last term V_{xc} is the exchange-correlation potential that contain all the remaining many-particle interactions, including the electron-electron interaction. V_{xc} is the most important term from all the DFT theory and its exact form is unknown, that is why is usually approximated. Several methods to approximate the exchange-correlation potential do exist including, the local density approximation (LDA), that assumes a constant density and approximate the system as a homogeneous electron gas. The generalized gradient approximation (GGA), considers variations at each site of the lattice and then include a gradient term. LDA+U and GGA+U methods are suitable for highly correlated systems, among other methods. In this section we will focus only on the most commonly used. More details on exchange-correlation potentials can be found in Ref. [78]. Once an approximation for V_{xc} is adopted, Eq. (2.1) can be solved self-consistently, following the procedure depicted in Fig. 2.2.

2.1.1 Local density approximation (LDA)

This method is widely used and is the simplest one to approximate the exchange-correlation potential V_{xc}. It consists in treating the system as it were a homogeneous electron gas of the same density $\rho(\boldsymbol{r})$, that

$$V_{xc}^{LDA} = \int v_{xc}[\rho(\boldsymbol{r})]\rho(\boldsymbol{r}) d\boldsymbol{r}, \tag{2.4}$$

where the term $v_{xc}[\rho(\boldsymbol{r})]$ is the exchange-correlation per particle and can be computed using the data from the QMC calculations from Ref. [79] for the ground state of an electron gas. This approximation works fine in systems weakly correlated, that is, when the density varies slowly like in group-IV semiconductors. Otherwise, the results are very inaccurate, like for Mott insulators. Until now we have not mention how to get the energies of excited states. From DFT we get only the ground state of a system. The functional of excited states cannot be obtained using the ground state functional because this can lead to inaccurate results. One way to solve this issue, is to expand the zero order LDA approximation to higher orders using perturbation theory as described in Ref. [80].

2.1.2 LDA+U and GGA+U

When the system is highly correlated, it is convenient to use LDA or GGA + U approaches with an extra term to the LDA to model "explicitly" the strong electron-electron inter-

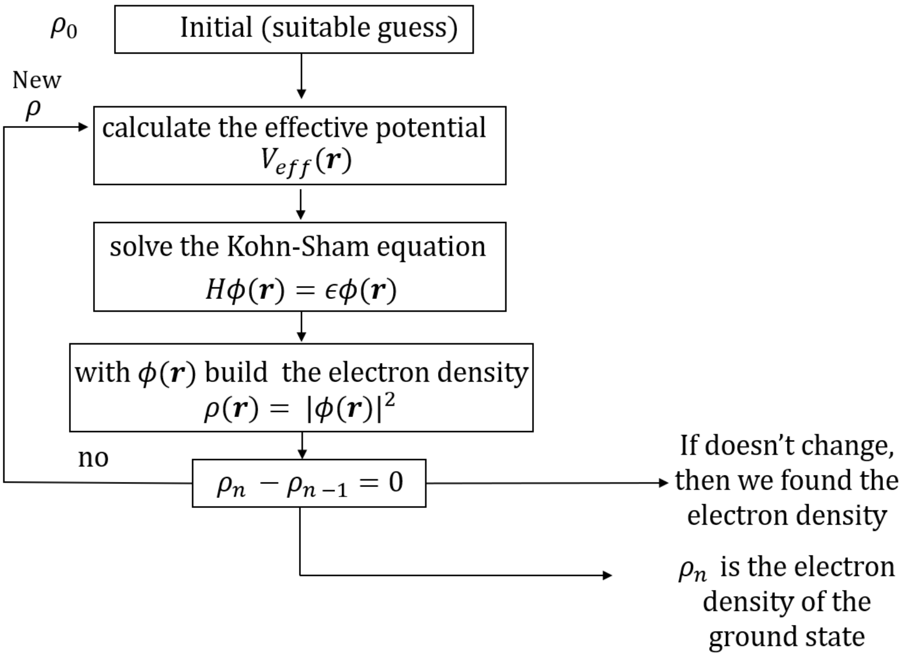

Figure 2.2: Chart showing the self consistent process needed to find the minima of $E[\rho]$. Chart adapted from Ref. [84]

action in this kind of systems, generally referred in the literature as "U". This method is inspired by the Hubbard model and its implementation in usual DFT codes do not demand significant effort, or significant computational power. The U term can be obtained from *ab initio* calculations or empirically from experimental data [81]. This method is appropriate to treat systems such as complex oxides like in Refs. [63], [82] and [83].

2.2 Tight-binding approach

In this section we discuss the tight-binding technique, the backbone of this thesis, and derive the dispersion energy equation for a pure graphene infinite sheet. For pedagogical purposes we show how is built the graphene nanoribbon tight-binding Hamiltonian and compare the results obtained for different edge terminations with simulations from the transport calculation python package Kwant [85]. The tight-binding technique is an approximation used to describe the behavior of electrons in crystalline lattices. Developed in 1928 by Bloch, the technique approximates the electronic band structure by superposing the wave functions of each atom. It neglects the particular atomic structure of the atoms that compose the crystal, as well as, the electron-electron interactions. Its use is appropriate in materials where the electrons are tightly bound to their atoms, like in semiconductors or insulators. The energy of the tight-binding wave function in crystal $\psi_{\vec{k}}$ can be obtained using the Schrödinger equation, thus

$$H\psi_{\vec{k}} = E\psi_{\vec{k}} \tag{2.5}$$

Using the bra-ket notation, it is easy to see that the energy is obtained after the diagonalization of the Hamiltonian H

$$\langle \phi_n | H | \psi_{\vec{k}} \rangle = E \langle \phi_n | \psi_{\vec{k}} \rangle, \tag{2.6}$$

where ϕ_n is the valence orbital of the n atom. Due to its accuracy, and the fact that the tight-binding Hamiltonian parameters can be obtained from experiments or adjusted from first principles calculations, the TB method can be used on a great variety of systems, what have made it so popular.

2.2.1 Tight-binding description of graphene

Let us consider the following Hamiltonian for a spinless graphene

$$H = \sum_{\alpha} \epsilon_\alpha | \phi_\alpha \rangle \langle \phi_\alpha | + \sum_{\alpha\beta} t_{\alpha\beta} | \phi_\alpha \rangle \langle \phi_\beta |, \tag{2.7}$$

where ϵ represents the onsite energy, $t_{\alpha\beta}$ is the hopping energy. The corresponding tight-binding wave function is:

$$\psi_{\vec{k}}(\vec{r}) = \frac{1}{\sqrt{N}} \sum_j e^{i(\vec{k}\cdot\vec{\delta}_j)} (c_1 \phi^A(\vec{r} - \vec{\delta}_j) + c_2 \phi^B(\vec{r} - \vec{\delta}_j)), \tag{2.8}$$

where $\phi^{A(B)}(\vec{r} - \vec{\delta}_j) = \langle \vec{r} - \vec{\delta}_j | \phi^{A(B)} \rangle$, N is the number of unit cells in the crystal, j runs over the nearest neighbors δ and A and B denote the graphene sublattices. Supposing without loss of generality $\epsilon_\alpha = 0$ and $t_{\alpha\beta} = t$, the Schrödinger equation gives

$$\begin{aligned} \langle \phi^A | H | \psi_{\vec{k}} \rangle &= E \langle \phi^A | \psi_{\vec{k}} \rangle \\ \langle \phi^B | H | \psi_{\vec{k}} \rangle &= E \langle \phi^B | \psi_{\vec{k}} \rangle, \end{aligned} \tag{2.9}$$

for the graphene nearest neighbors (Eq. (1.31))

$$\begin{aligned} -tc_1 \left(e^{-i\vec{r}\cdot\vec{\delta}_1} + e^{-i\vec{r}\cdot\vec{\delta}_2} + e^{-i\vec{r}\cdot\vec{\delta}_3} \right) &= Ec_2 \\ -tc_2 \left(e^{i\vec{r}\cdot\vec{\delta}_1} + e^{i\vec{k}\cdot\vec{\delta}_2} + e^{i\vec{r}\cdot\vec{\delta}_3} \right) &= Ec_1, \end{aligned} \tag{2.10}$$

so the tight-binding Hamiltonian can be written as

$$H(k_x, k_y) = \begin{pmatrix} 0 & e^{-iak_x} + 2e^{\frac{iak_x}{2}} \cos\left(\frac{\sqrt{3}a}{2} ak_y \right) \\ e^{iak_x} + 2e^{-\frac{iak_x}{2}} \cos\left(\frac{\sqrt{3}a}{2} ak_y \right) & 0 \end{pmatrix}, \tag{2.11}$$

whose eigenenergies are given by the following energy dispersion:

$$E(k_x, k_y) = \pm t\sqrt{1 + 4\cos\frac{\sqrt{3}a}{2}k_x \cos\frac{a}{2}k_y + 4\cos^2\frac{a}{2}k_y},$$

the same result as in equation Eq. (1.33)

Graphene nanoribbon

Graphene nanoribbons present boundaries in one direction and translational symmetry in the other, i.e. is periodic. In the direction of translation symmetry, the Bloch theorem is applicable, so the hoppings in this direction should be multiplied by a phase of the form $e^{i\vec{k}\cdot\vec{d}}$. The graphene edge terminations changes the band structure of the system, that is why, as we will see, the Hamiltonian is different for armchair and zigzag edges. To prove this, let us consider the graphene lattices from Fig. 2.3. Both systems are small, but the implementation of a bigger system is straightforward.

Note that in Fig. 2.3(a) we can link along the translational symmetry the sites whose positions follow the equations $4n$ and $4n-1$, for $n = 1, 2, 3, ..., N$. In our case $N = 10$, then the extra factor should be added to the sites 4 and 3, 7 and 8, as well as to their reciprocal values, thus the Hamiltonian can be expressed as:

$$H = \begin{array}{cc}
\begin{array}{cccccccccc} \mathbf{1} & \mathbf{2} & \mathbf{3} & \mathbf{4} & \mathbf{5} & \mathbf{6} & \mathbf{7} & \mathbf{8} & \mathbf{9} & \mathbf{10} \end{array} & \\
\begin{pmatrix}
0 & t & 0 & t & 0 & 0 & 0 & 0 & 0 & 0 \\
t & 0 & t & 0 & 0 & 0 & 0 & 0 & 0 & 0 \\
0 & t & 0 & te^{ik_x} & 0 & t & 0 & 0 & 0 & 0 \\
t & 0 & te^{-ik_x} & 0 & t & 0 & 0 & 0 & 0 & 0 \\
0 & 0 & 0 & t & 0 & t & 0 & t & 0 & 0 \\
0 & 0 & t & 0 & t & 0 & t & 0 & 0 & 0 \\
0 & 0 & 0 & 0 & 0 & t & 0 & te^{ik_x} & 0 & t \\
0 & 0 & 0 & 0 & t & 0 & te^{-ik_x} & 0 & t & 0 \\
0 & 0 & 0 & 0 & 0 & 0 & 0 & t & 0 & t \\
0 & 0 & 0 & 0 & 0 & 0 & t & 0 & t & 0
\end{pmatrix} &
\begin{array}{c} \mathbf{1} \\ \mathbf{2} \\ \mathbf{3} \\ \mathbf{4} \\ \mathbf{5} \\ \mathbf{6} \\ \mathbf{7} \\ \mathbf{8} \\ \mathbf{9} \\ \mathbf{10} \end{array}
\end{array} \tag{2.12}$$

The diagonalization of this Hamiltonian gives us the band structure of an armchair graphene nanoribbon of 5 atoms width (semi-metallic behavior) shown in Fig. 2.4(a).

For the zigzag edges case, the linking along the translational symmetric direction is trickier due to graphene lattice geometry. Note that the extra factor is added when one needs to link a site in one boundary to a site in the opposite boundary respecting the symmetry of the lattice. For the zigzag graphene nanoribbon of Fig. 2.3(b) where N=8, the sites 1 and 2 are linked by a hopping t, but they are as well boundary sites, so a link is possible. One can see that site 1 is equivalent to site γ, that makes necessary to add in

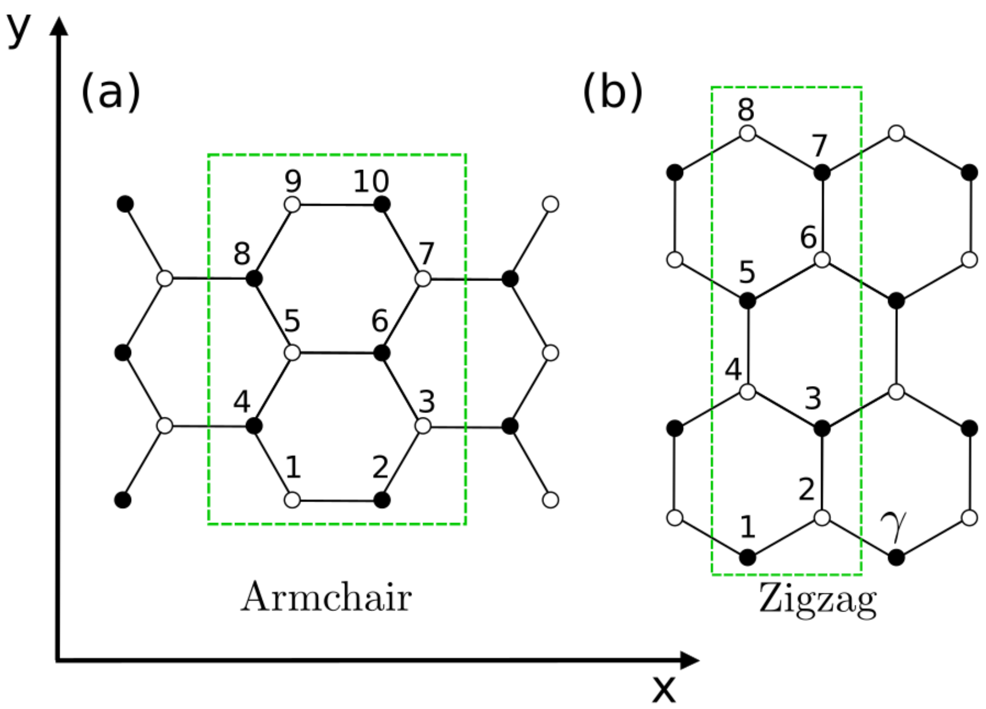

Figure 2.3: (a) unit cell of an armchair graphene nanoribbon of width 5 atoms. (b) unit cell of a zigzag graphene nanoribbon. The black circles (open circles) represent atoms of sublattice A (B). The direction of translation symmetry for both nanoribbons is along x.

its Hamiltonian the extra factor when linking site 1 and 2. Thus, the factor e^{-ik_x} should be added to the sites whose positions follow $2n-1$ and $2n$, i.e. for sites 1 and 2, 3 and 4, 5 and 6, 7 and 8, so we can write the Hamiltonian as:

$$H = \begin{array}{ccccccccc}
\mathbf{1} & \mathbf{2} & \mathbf{3} & \mathbf{4} & \mathbf{5} & \mathbf{6} & \mathbf{7} & \mathbf{8} & \\
0 & t+te^{ik_x} & 0 & 0 & 0 & 0 & 0 & 0 & \mathbf{1} \\
t+te^{-ik_x} & 0 & t & 0 & 0 & 0 & 0 & 0 & \mathbf{2} \\
0 & t & 0 & t+te^{ik_x} & 0 & 0 & 0 & 0 & \mathbf{3} \\
0 & 0 & t+te^{-ik_x} & 0 & t & 0 & 0 & 0 & \mathbf{4} \\
0 & 0 & 0 & t & 0 & t+te^{ik_x} & 0 & 0 & \mathbf{5} \\
0 & 0 & 0 & 0 & t+te^{-ik_x} & 0 & t & 0 & \mathbf{6} \\
0 & 0 & 0 & 0 & 0 & t & 0 & t+te^{ik_x} & \mathbf{7} \\
0 & 0 & 0 & 0 & 0 & 0 & t+te^{-ik_x} & 0 & \mathbf{8}
\end{array} \tag{2.13}$$

When diagonalized this Hamiltonian gives the band structure shown in Fig. 2.4(b).

2.3 Tight-binding model for graphene with proximity induced magnetism

In this work we propose a tight-binding Hamiltonian that fits the band structure obtained from a DFT method. We show how proximity magnetic effects are included in the tight-

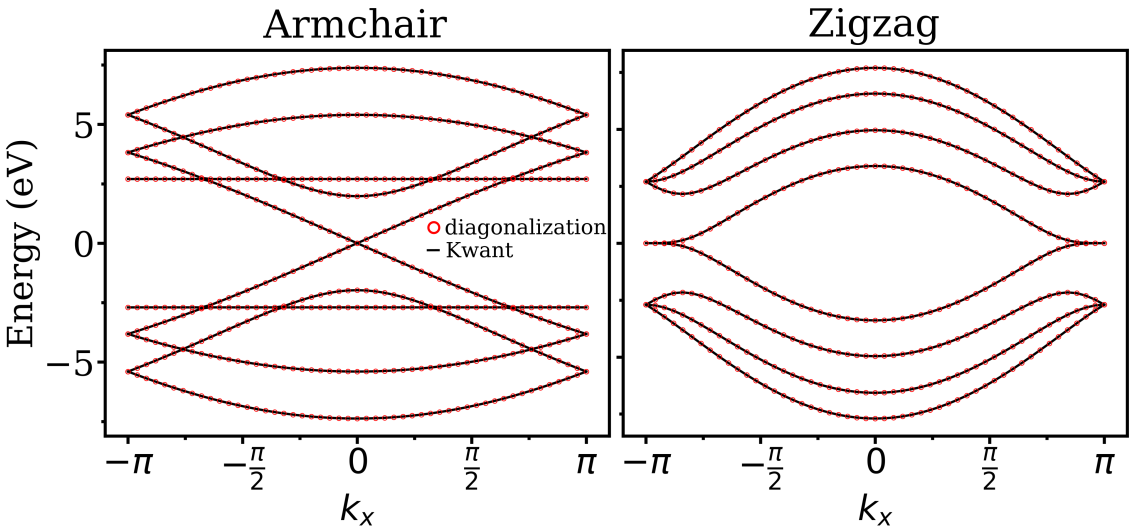

Figure 2.4: Band structure for the graphene nanoribbons of Fig. 2.3 for a system with (a) armchair edges and (b) zigzag edges. The figure shows a comparison between the solid line (black) bands that were obtained using the python package Kwant and the open circle (red) bands that were obtained from direct diagonalization of the matrices from Eq. (2.12) and Eq. (2.13).

binding Hamiltonian. In order to derive it, for pedagogical reasons, let us consider the band structure from Fig. 2.5(a). An infinite graphene sheet do not have gap and the spin up and spin down bands are degenerate. The presence of a magnet on top of graphene, breaks the spin bands degeneracy and depending on the properties of the neighboring magnetic material, it can open a band gap. To build the Hamiltonian it is necessary to take into account the following band parameters: the Dirac cone energy with respect the Fermi energy E_D, the energy gap E_G, the spin up band splitting $\varDelta_\uparrow$, the spin down band splitting $\varDelta_\downarrow$, the electrons band splitting δ_e and the holes band splitting δ_h. All these parameters have been sketched in Fig. 2.5. It is easy to show that

$$\begin{aligned} E_G = \varDelta_\downarrow - \delta_e &= \varDelta_\uparrow - \delta_h \\ \varDelta_\downarrow - \varDelta_\uparrow &= \delta_e - \delta_h, \end{aligned}$$

so, there are only 4 independent parameters. From Fig. 2.5(a) it is possible to obtain the following set of equations:

$$E_{e\downarrow} - E_{h\uparrow} = \varDelta_\downarrow \tag{2.14}$$

$$E_{e\uparrow} - E_{h\downarrow} = \varDelta_\uparrow \tag{2.15}$$

$$E_{e\downarrow} - E_{e\uparrow} = \delta_e \tag{2.16}$$

$$E_{h\uparrow} - E_{h\downarrow} = \delta_h, \tag{2.17}$$

where $E_{e\uparrow(\downarrow)}$, $E_{h\uparrow(\downarrow)}$ are the energy minima of the up(down) spin electron band and

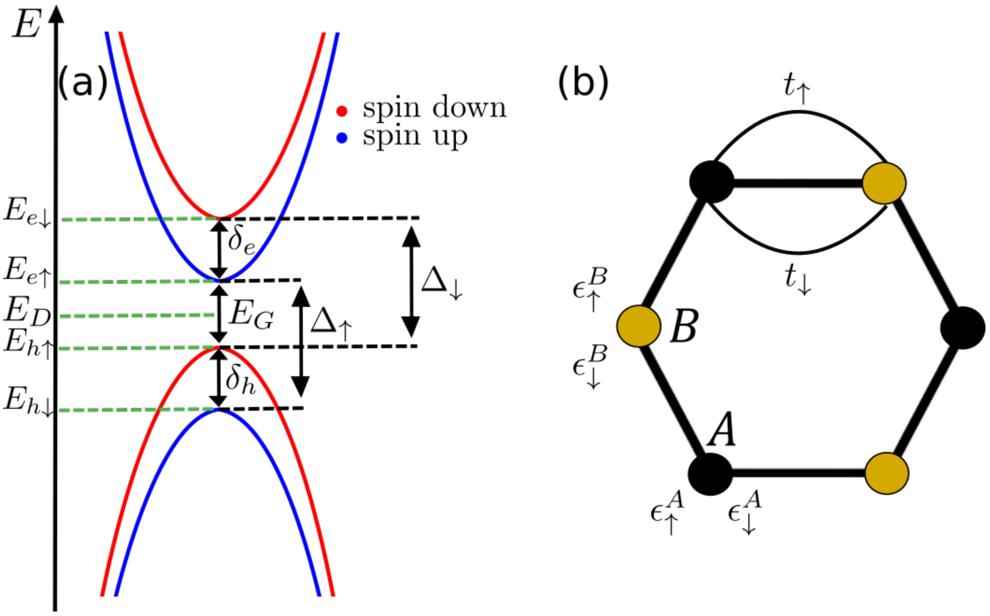

Figure 2.5: (a) Sketch of a magnetic graphene band structure. E_D is the Dirac energy, E_G is the gap energy, $\varDelta_\uparrow$, $\varDelta_\downarrow$ is the gap energy of the spin up band and spin down band respectively. δ_e, δ_h is the spin splitting of the the electrons band and holes band respectively. (b) Diagram showing the spin dependent components ($\epsilon_\uparrow$ and $\epsilon_\downarrow$) of the sublattice potentials and the spin dependent hoppings of a graphene hexagon.

the up(down) spin hole band, respectively. Solving for $E_{e\uparrow}$, $E_{e\downarrow}$, $E_{h\uparrow}$, $E_{h\downarrow}$, we get

$$\begin{aligned} E_{e\downarrow} &= \frac{1}{2}(\varDelta_s + \delta + \varDelta_\delta) \\ E_{e\uparrow} &= \frac{1}{2}(\varDelta_s - \delta - \varDelta_\delta) \\ E_{h\uparrow} &= \frac{1}{2}(-\varDelta_s + \delta - \varDelta_\delta) \\ E_{h\downarrow} &= \frac{1}{2}(-\varDelta_s - \delta + \varDelta_\delta), \end{aligned} \tag{2.18}$$

where we have defined

$$\delta = \frac{\delta_e + \delta_h}{2} \tag{2.19}$$

$$\varDelta_s = \frac{\varDelta_\uparrow + \varDelta_\downarrow}{2} \tag{2.20}$$

$$\varDelta_\delta = \frac{\delta_e - \delta_h}{2} = \frac{\varDelta_\downarrow - \varDelta_\uparrow}{2}. \tag{2.21}$$

δ can be interpreted as the strength of the exchange spin splitting, $\varDelta_s$ is the strength of the spin dependent staggered sublattice potential and $\varDelta_\delta$ can be interpreted as the strength of the spin-sublattice interaction. Using these parameters we can write a continuous

Hamiltonian for the band structure of Fig. 2.5(a) as:

$$H(q) = \left(v_f \boldsymbol{\sigma}\cdot\boldsymbol{q} + \frac{\delta}{2}(\boldsymbol{s}\cdot\boldsymbol{m}) + \frac{\Delta_s}{2}\sigma^z\right)\otimes \mathbb{1} + \frac{\Delta_\delta}{2}\sigma^z \otimes (\boldsymbol{s}\cdot\boldsymbol{m}), \tag{2.22}$$

v_f is the Fermi velocity, σ is a spin operator that acts on the sublattice space, $\boldsymbol{s}$ is a vector of Pauli matrices that acts on the spin space and $\boldsymbol{m}$ is the magnetization vector. The first term corresponds to the kinetic energy which is of Dirac type, i.e. describes massless fermions and $\boldsymbol{q}$ is the momentum measured relative to the Dirac point. Let us now discretize Eq. (2.22) in order to obtain the Hamiltonian of a finite system, then

$$H = t\sum_{\langle i,j\rangle\sigma} c^\dagger_{i\sigma}c_{j\sigma} + H.c. + \sum_{n\in A}\sum_{\sigma,\sigma'} V^A_{\sigma,\sigma'}c^\dagger_{n\sigma}c_{n\sigma'} + \sum_{n\in B}\sum_{\sigma,\sigma'} V^B_{\sigma,\sigma'}c^\dagger_{n\sigma}c_{n\sigma'}, \text{ with} \tag{2.23}$$

$$V^A = E_D\mathbb{1} + \frac{\Delta_s}{2}\mathbb{1} + \left(\frac{\Delta_\delta}{2} + \frac{\delta}{2}\right)(\boldsymbol{s}\cdot\boldsymbol{m})$$

$$V^B = E_D\mathbb{1} - \frac{\Delta_s}{2}\mathbb{1} + \left(-\frac{\Delta_\delta}{2} + \frac{\delta}{2}\right)(\boldsymbol{s}\cdot\boldsymbol{m}),$$

where t is the hopping parameter, $c^\dagger_{i\sigma}$ ($c_{i\sigma}$) creates (annihilates) an electron with spin σ in the site i. V^A and V^B are the spin dependent sublattice onsite potential, that appears as a consequence of the neighboring magnetic material. In the systems considered in this thesis, the hoppings found to fit the bands are spin dependent, so changes in the Hamiltonian of Eq. (2.23) have to be included in order to take into account this feature. Fig. 2.5(b) shows a diagram representing on a graphene hexagon the spin dependent components ($\epsilon_\uparrow$ and $\epsilon_\downarrow$) of the sublattice potentials V^A and V^B and the spin dependent hoppings $t_\uparrow$ and $t_\downarrow$. Note that we have the following 4 degrees of freedom $A\uparrow$, $A\downarrow$, $B\uparrow$, $B\downarrow$, so the hopping for any pair of sites should look like:

$$\begin{array}{cc}
\begin{array}{cccc} A\uparrow & A\downarrow & B\uparrow & B\downarrow \end{array} & \\
\begin{pmatrix} 0 & 0 & t_\uparrow & 0 \\ 0 & 0 & 0 & t_\downarrow \\ t_\uparrow & 0 & 0 & 0 \\ 0 & t_\downarrow & 0 & 0 \end{pmatrix} & \begin{array}{c} A\uparrow \\ A\downarrow \\ B\uparrow \\ B\downarrow \end{array}
\end{array}$$

A Hamiltonian that reproduce the previous values is:

$$H_1 = \sum_\sigma t_\sigma c^\dagger_{1\sigma}c_{0\sigma} + H.c., \tag{2.24}$$

where σ can be either ↑ or ↓, $c^\dagger_{\mu\sigma}$ ($c_{\mu\sigma}$) creates (annihilates) an electron of the type A ($\mu = 0$) or B ($\mu = 1$) with spin σ, and t_σ is a spin dependent hopping that connects nearest neighbors sites. In addition to the spin dependent hopping, there are cases where one needs to use anisotropic hoppings in order to model properly the band structure, therefore this Hamiltonian can be expressed as:

$$H_1 = \sum_{i\sigma} \sum_{l} t_{l\sigma} c^{\dagger}_{(i+l)1\sigma} c_{i0\sigma} + H.c., \tag{2.25}$$

where $t_{l\sigma}$ represents the anisotropic hopping connecting unit cells i to their nearest neighbors cells $i+l$. The full Hamiltonian of our system is then:

$$\begin{aligned} H = \sum_{i\sigma} \sum_{l} t_{l\sigma} c^{\dagger}_{(i+l)1\sigma} c_{i0\sigma} + H.c. + \sum_{i\sigma\sigma'} \sum_{\mu=0}^{1} \left[\delta + (-1)^{\mu} \Delta_{\delta}\right] c^{\dagger}_{i\mu\sigma} [\vec{m}.\vec{\sigma}]_{\sigma\sigma'} c_{i\mu\sigma'} \\ + \sum_{i\sigma} \sum_{\mu=0}^{1} \left[E_D + (-1)^{\mu} \Delta_s\right] c^{\dagger}_{i\mu\sigma} c_{i\mu\sigma}, \end{aligned} \tag{2.26}$$

2.4 Transport formalism

In this section we discuss the scattering matrix method, as well as its mathematical properties. Later, we present the Landauer formalism where we derive the conductance formula for transport in mesoscopic systems. In the last part, we present a brief description of Kwant and how this package is employed for the calculation of the transport properties of systems using the scattering matrix method and the Landauer formula.

2.4.1 Scattering matrix

In a coherent conductor whose dimensions are smaller than its mean free path ℓ, the transmission function can be calculated solving the Schrödinger equation at each energy. This process can be characterized by relating the incoming and outgoing modes through a matrix known as scattering matrix (S-matrix). Without loss of generality, let us consider a 1D system, as the depicted in Fig. 2.6, where the electron wave function Ψ_1 can be written as:

$$\Psi_1(x,y) = \sum_{n=1}^{N_{ch}} (a_n^+ \psi_n^+(x,y) + a_n^- \psi_n^-(x,y)) \tag{2.27}$$

with

$$\psi_n^{\pm}(x,y) = \phi_n(y) e^{\pm i k_n x} \tag{2.28}$$

where N_{ch} is the total number of channels, k_n is the wave vector and $+$ $(-)$ indicates if the wave moves to the right(left). Similarly Ψ_2:

$$\Psi_2(x,y) = \sum_{n=1}^{N_{ch}} (b_n^- \psi_n^-(x,y) + b_n^+ \psi_n^+(x,y)) \tag{2.29}$$

Rearranging the incoming(outgoing) modes

$$c^{in} = (a_1^+, a_2^+, ...b_{N_{ch}}^+, b_1^-, b_2^-, ...b_{N_{ch}}^-) \tag{2.30}$$

$$c^{out} = (a_1^-, a_2^-, ...b_{N_{ch}}^-, b_1^+, b_2^+, ...b_{N_{ch}}^+) \tag{2.31}$$

so that c^{in} and c^{out} can be related using the matrix S as follows:

$$c^{in} = Sc^{out}, \tag{2.32}$$

where S has the block structure

$$S = \begin{pmatrix} r & t' \\ t & r' \end{pmatrix} \tag{2.33}$$

The S-matrix is a $2N_{ch} \times 2N_{ch}$ matrix, where N_{ch} represents the number of channels in the system. The matrices t and r are both $N_{ch} \times N_{ch}$ and represent the transmission and reflection amplitudes, respectively [86]. They differ from the primed matrices t' and r' on the wavefunction propagation direction. From the S-matrix construction it is easy to see that the t and r matrices represent the amplitudes of the wavefunction propagates from left to right, while t' and r' that from right to left.

Figure 2.6: Sketch of incoming(outgoing) waves moving toward(away) a scattering region. The sign $+(-)$ indicates that the wave moves to the right(left).

Scattering matrix properties

In order to preserve the current conservation equation, it is required the scattering matrix S to be unitary, so that

$$S^\dagger S = SS^\dagger = \mathbb{1}, \text{ and} \tag{2.34}$$

$$\sum_{m=1}^{N_{ch}} |S_{mn}|^2 = \sum_{m=1}^{N_{ch}} |S_{nm}|^2 = 1, \tag{2.35}$$

2.4.2 Landauer formula for conductance

The conductance of mesoscopic systems cannot be described with the ohmic law $G = \sigma W/L$, because as the dimensions of the system become smaller, the conductance stops following a linear behavior as a function the width W and becomes independent of the

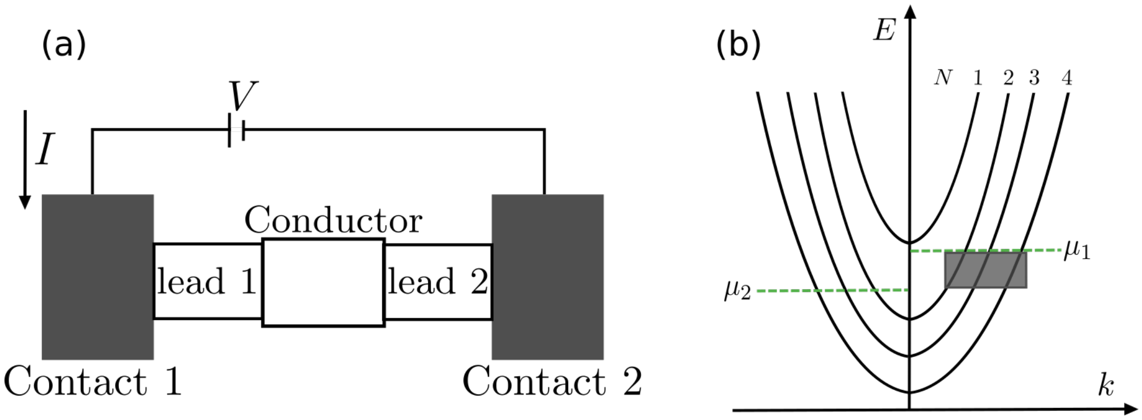

Figure 2.7: (a) Conductor attached to two leads which are connected to two reservoirs (contacts 1 and 2). The contacts have different chemical potentials so there is current I flowing through the conductor. (b) Bands in a narrow conductor. The square indicates the states that can carry current. The number of modes in this hypothetical system are the number of intersections of the energies μ_1 and μ_2 with the bands, in this case both have 3 modes. Figures adapted from [72].

length L [72]. Let us consider a narrow conductor attached to two leads at zero temperature, and consider this system in the ballistic regime, i.e., there is no scattering. Connected to the leads there are two contacts considered reflectionless, it is, the electrons from the contacts enter or exit to the leads without reflection and do not suffer scattering. This situation is depicted in Fig. 2.7(a), where μ_1 and μ_2 are chemical potentials in lead 1 and 2, respectively. Considering N_{ch} as the number of modes in the lead and an applied bias $\mu_1 - \mu_2$ between the contacts, the current from the lead 1 can be expressed as:

$$I_1^+ = \frac{2e^2}{h} N_{ch} \frac{(\mu_1 - \mu_2)}{e} \tag{2.36}$$

where number of modes N_{ch} depends on the dimensionality of the system, so

$$N_{ch} = \left.\frac{S}{\lambda_F^2/2\pi}\right|_{3D} = \left.\frac{W}{\lambda_F/2}\right|_{2D}, \tag{2.37}$$

where λ_F is the Fermi wavelength. For 3D conductors the number of modes N_{ch} is directly proportional to their transversal section S, while in 2D conductors it is directly proportional to their width W. Graphically, the modes can be much better understood when depicted in a band structure. Fig. 2.7(b) shows three active modes of a hypothetical conductor at energies μ_1 and μ_2, according to the number of bands between them.

When the conductor and leads of a system are treated as waveguides for the electrons, it is possible to describe the transport properties of a device by solving a scattering problem. In this approach, we can write the outflow current from the conductor as:

$$I_2^+ = \frac{2e^2}{h} N_{ch} T(E) \frac{(\mu_1 - \mu_2)}{e}, \text{ with } T(E) \in \mathbb{R}^+ \tag{2.38}$$

where $T(E)$ is the transmission probability of an electron with energy E going from lead 1 to lead 2. The reflected current in the conductor that goes back to the contact 1 can be written as:

$$I_1^- = \frac{2e^2}{h} N_{ch}(1 - T(E))\frac{(\mu_1 - \mu_2)}{e}, \tag{2.39}$$

so that the net current at any point in the device becomes:

$$I = I_1^+ - I_1^- = \frac{2e^2}{h} N_{ch} T(E)\frac{(\mu_1 - \mu_2)}{e}. \tag{2.40}$$

The conductance $G = I/V$ can be expressed then:

$$G = \frac{2e^2}{h} N_{ch} T(E), \tag{2.41}$$

which is the famous Landauer formula for spin-degenerate systems. This expression assumes that the transmission in all N_{ch} channels is the same, in a more general way we can write the previous equation as:

$$G = \frac{2e^2}{h} \sum_{n}^{N_{ch}} T_n(E), \tag{2.42}$$

where we sum the transmission of each mode N_{ch}. The transmission function is a quantity that allows describing the current passing through a conductor and can be obtained using different methods, for example using Green functions or the scattering matrix formalism. For the latter, the transmission can be obtained using the following formula:

$$T = Tr(tt^\dagger), \tag{2.43}$$

where t is a coefficient of the S-matrix from Eq. (2.33) and $t^\dagger$ its conjugate transpose.

2.4.3 Kwant formalism

In this work to perform transport calculations we used the python package Kwant. This numerical calculation tool aims to solve the scattering problem of physical systems that can be described by a tight-binding model in a robust and efficient way [85]. Kwant has embedded various methods to calculate the conductance, such as scattering matrix and non-equilibrium Green functions. Both methods are equivalent, but the non-equilibrium Green's function is less stable, and due to this fact Kwant is based on the wave function approach.

A structure to model transport is composed by a scattering region and leads with translational symmetry. An arbitrary system modeled with Kwant is shown in Fig. 2.8.

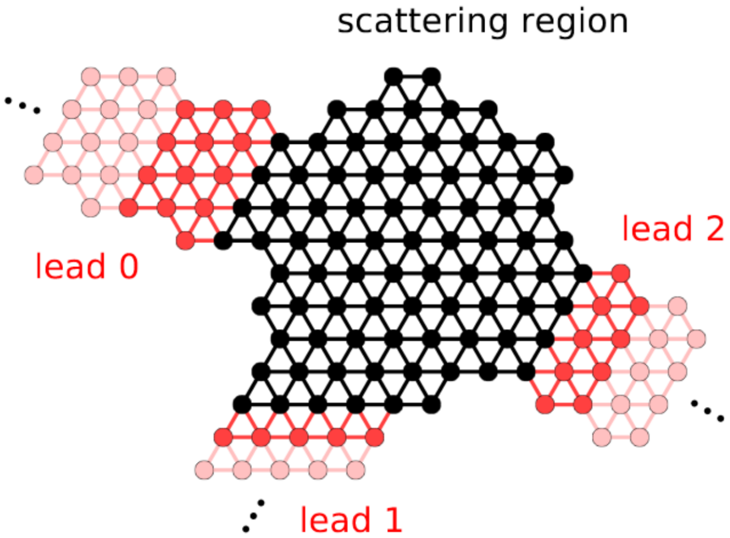

Figure 2.8: Tight-binding system modeled using Kwant. The semi-infinite lead are represented by using red dots and the scattering region by black dots. Figure taken from Ref. [85].

Without loss of generality, let us consider a scattering problem where there is only one lead attached to the system. A solution for two leads systems can be found in [87]. The generalization to systems with more leads is straightforward. A Hamiltonian composed by one semi-infinite lead and a scattering region has the following form:

$$H = \begin{pmatrix} \ddots & V_L & 0 & \cdots \\ V_L^\dagger & H_L & V_L & \\ 0 & V_L^\dagger & H_L & V_{LS} \\ & & V_{LS}^\dagger & H_S \end{pmatrix}, \tag{2.44}$$

where H_S and H_L are the Hamiltonians of the scattering region and lead respectively. V_L connects internally the neighboring unit cells in the lead and V_{LS} is the hopping matrix that connects the closest unit cell of the lead to the scattering region. The eigenvectors of this Hamiltonian has the form $(..., \psi^L(2), \psi^L(1), \psi^L(0), \psi^S)$, where $\psi^L(i)$ is the wave function in the i-th unit cell of the lead and ψ^S represents the wave function in the scattering region. Making use of the translational symmetry of the lead, let us expand the eigenstates as

$$\phi_n(j) = (\lambda_n)^j \chi_n, \tag{2.45}$$

in order to make them obey the Schrödinger equation

$$(H_L + V_L \lambda_n^{-1} + V_L^\dagger \lambda_n)\chi_n = E\chi_n, \tag{2.46}$$

where χ_n indicates the n-th lead unit cell eigenvector, and λ_n is the n-th eigenvalue. Let us now find the eigenvectors by introducing the following auxiliary vector

$$\chi'_n \equiv \lambda_n^{-1} V_L \chi_n, \tag{2.47}$$

so that Eq. (2.46) can be written in matricial form as:

$$\begin{pmatrix} H_L - E & \mathbb{1} \\ V_L & 0 \end{pmatrix} \begin{pmatrix} \chi_n \\ \chi'_n \end{pmatrix} = \lambda_n \begin{pmatrix} -V_L^\dagger & 0 \\ 0 & \mathbb{1} \end{pmatrix} \begin{pmatrix} \chi_n \\ \chi'_n \end{pmatrix}, \tag{2.48}$$

Note that $\lambda_n = e^{ik_n}$ because of the Bloch theorem, where k_n is the longitudinal momentum of the mode n. With this, previous equation can be easily solved by means of numerical algorithms. Because of the wave function normalization $|\lambda_n| \leq 1$. For $|\lambda_n| < 1$ the modes will be evanescent and propagating for $|\lambda_n| = 1$. The group velocity, for the n-th mode can be written as:

$$v_n = \frac{-2}{\hbar} Im(\chi_n^\dagger V_L \lambda_n \chi_n). \tag{2.49}$$

The modes are incoming if $v_n > 0$, outgoing if $v_n < 0$ and evanescent if $v_n = 0$. Let us now expand the scattering states of the lead for each type of mode:

$$\psi_n^L(i) = \phi_n^{in}(i) + \sum_m S_{mn} \phi_m^{out}(i) + \sum_p \tilde{S}_{pn} \phi_p^{ev}(i), \tag{2.50}$$

where ϕ_n^{in}, ϕ_m^{out}, ϕ_p^{in} are the eigenstates for the incoming, outcoming and evanescent modes, respectively. S_{mn} is the scattering matrix and $\tilde{S}_{pn}$ represents a non unitarian matrix proportional to the scattering matrix S_{mn} [72]. The scattering matrix and the wave function in the scattering region can be obtained by solving $H\psi_n = E\psi_n$, for Eq. (2.48). This gives the following set of equations:

$$V_{LS}^\dagger \psi_n^L(0) + (H_S - E)\psi_n^S = 0 \tag{2.51}$$

$$V_L^\dagger \psi_n^L(1) + (H_L - E)\psi_n^L(0) + VLS\psi_n^S = 0. \tag{2.52}$$

By substituting Eq. (2.50) into Eq. (2.52)

$$\begin{gathered} V_L^\dagger \left(\phi_n^{in}(1) + \sum_m S_{mn} \phi_m^{out}(1) + \sum_p \tilde{S}_{pn} \phi_p^{ev}(1) \right) + \\ (H_L - E) \left(\phi_n^{in}(0) + \sum_m S_{mn} \phi_m^{out}(0) + \sum_p \tilde{S}_{pn} \phi_p^{ev}(0) \right) + V_{LS}\psi_n^S = 0, \end{gathered} \tag{2.53}$$

using the definition $\phi_n(j) = (\lambda_n)^j \chi_n$ and rearranging the terms we get:

$$\begin{split}\left(V_L^\dagger \chi_n^{in} + (H_L - E)\chi_n^{in}\right) + \left(V_L^\dagger \sum_m S_{mn}\lambda_m^{-1}\chi_m^{out} + (H_L - E)\sum_m \tilde{S}_{mn}\chi_m^{out}\right) + \\ \left(V_L^\dagger \sum_p \tilde{S}_{pn}\lambda_p^{-1}\chi_p^{ev} + (H_L - E)\sum_p \tilde{S}_{pn}\chi_p^{ev}\right) + V_{LS}\psi_n^S = 0.\end{split} \tag{2.54}$$

Using Eq. (2.46) to rewrite each term inside the parenthesis, we then get:

$$-\lambda_n^{-1}V_L\chi^{in} - V_L\sum_m S_{mn}\lambda_m^{-1}\chi_m^{out} - V_L\sum_p \tilde{S}_{pn}\lambda_p^{-1}\chi_p^{ev} + V_{LS}\psi_n^S = 0, \tag{2.55}$$

note that the first three terms of this expression resembles Eq. (2.50), so after using Eq. (2.45) we get:

$$V_{LS}\psi_n^S = V_L\psi_n^L(-1). \tag{2.56}$$

Using Eq. (2.50) to evaluate $\psi_n(-1)$ and substituing Eq. (2.47) we get finally:

$$V_{LS}\psi_n^S = \chi_n'^{in} - \sum_m S_{mn}\chi_m'^{out} - \sum_p \tilde{S}_{pn}\chi_p'^{ev} \tag{2.57}$$

Using Eq. (2.57) and Eq. (2.51), and substituting $\psi_n^L(0) = \chi_n^{in} + \sum_m S_{mn}\chi_m^{out} + \sum_p \tilde{S}_{pn}\chi_p^{ev}$ we can build for each mode n a matrix of the form

$$\begin{pmatrix} H_S - E & V_{LS}^\dagger\chi^{out} & V_{LS}^\dagger\chi^{ev} \\ V_{LS}\chi_n^{out} & -\chi'^{out} & -\chi'^{ev}\end{pmatrix}\begin{pmatrix}\psi_n^S \\ S_n \\ \tilde{S}_n\end{pmatrix} = \begin{pmatrix} -V_{LS}^\dagger\chi_n^{in} \\ \chi_n'^{in}\end{pmatrix}, \tag{2.58}$$

where we have defined $\chi^\eta = (\chi_1^\eta, \chi_2^\eta, ..., \chi_N^\eta)$, with $\eta = in, out, ev$ modes. Here $N = N_p$ for incoming and outgoing modes and $M = N_{ev}$ for evanescent ones, so in total there are $M_T = N_p + N_{ev}$ modes in the lead with $S_n = (S_{1n}, S_{2n}, ..., S_{N_p n})$ and $\tilde{S}_n = (\tilde{S}_{1n}, \tilde{S}_{2n}, ..., \tilde{S}_{N_{ev} n})$. Accounting for all the modes in the system, the full scattering matrix S is of $N_p \times N_p$ size, $\tilde{S}$ has dimensions $N_{ev} \times N_p$, while ψ^S is of $N_s \times N_p$ size, where N_s is the number of sites of the scattering region. The scattering matrix S and the scattering region wave function ψ^S are the main outputs obtained with Kwant.

2.5 Observables

In order to investigate the spin transport properties of a lateral graphene-based spintronic device, we analyzed five physical quantities: conductance, charge current density, spin density, spin current density and spin transfer torque. The expectation values of each quantity were obtained using the scattering matrix formalism. All these quantities were obtained using Kwant, so for each quantity the corresponding Kwant function will be presented.

2.5.1 Conductance G

Our system has spin structure, and it is necessary therefore to include this feature in the scattering matrix from Eq. (2.48), i.e.

$$\begin{pmatrix} r_{\uparrow\uparrow} & r_{\uparrow\downarrow} & t'_{\uparrow\uparrow} & t'_{\uparrow\downarrow} \\ r_{\downarrow\uparrow} & r_{\downarrow\downarrow} & t'_{\downarrow\uparrow} & t'_{\downarrow\downarrow} \\ t_{\uparrow\uparrow} & t_{\uparrow\downarrow} & r'_{\uparrow\uparrow} & r'_{\uparrow\downarrow} \\ t_{\downarrow\uparrow} & t_{\downarrow\downarrow} & r'_{\downarrow\uparrow} & r'_{\downarrow\downarrow} \end{pmatrix} \tag{2.59}$$

where $t_{\sigma\sigma'}$ are $N_{ch} \times N_{ch}$ matrices, composed by the transmission amplitudes between σ and σ' states [86]. At zero temperature conductance can be calculated using Eq. (2.42) can be used. When $T \neq 0$ K one needs to sum up over all the energies according to

$$G = \frac{e^2}{h} \sum_{\sigma} \int T^{\sigma} \left(-\frac{\partial f}{\partial E} \right) dE, \tag{2.60}$$

where $f = 1/(e^{(E-\mu)/k_B T} + 1)$ is the Fermi-Dirac distribution and T^{σ} is the spin dependent transmission, which can be expressed as:

$$T^{\uparrow} = |t_{\uparrow\uparrow}|^2, \qquad\qquad T^{\downarrow} = |t_{\downarrow\downarrow}|^2. \tag{2.61}$$

These formulas are valid for collinear magnetic configurations, but not for the non-collinear case. Let us discuss another very important case, when spin-orbit coupling is included. The presence of SOC mix the spin channels, so it is not possible to separate each spin contribution, moreover, it is necessary to add spin mixing terms to correctly calculate the transmission. A meaningful physical quantity for this kind of systems is the total transmission, that can be calculated using the formula:

$$T^{tot} = |t_{\uparrow\uparrow}|^2 + |t_{\downarrow\downarrow}|^2 + |t_{\downarrow\uparrow}|^2 + |t_{\uparrow\downarrow}|^2, \tag{2.62}$$

where the last two terms correspond to the added spin mixing terms.

In Kwant the transmission for each energy can be calculated as follows, after building the tight-binding Hamiltonian of the system, the scattering matrix is calculated using the function kwant.smatrix. With this result in hand, the second and final step is to calculate the transmission for an energy E, to do so, it is necessary to use the function transmission. A snippet of how this code look is showed below, for more information please see Kwant documentation from Ref. [88]

```
# Energy window of interest
energies = np.linspace(-1.2,1,300)
# Hf is the Hamiltonian of the system
smatrices = [kwant.smatrix(Hf, energy) for energy in energies]
gs_AP.append([smatrix.transmission((1,0),(0,0)) for smatrix in smatrices])
```

2.5.2 Charge density response ρ_c and spin density response ρ_{s_z}

We can define the response function η_{res} of a quantity ζ at the site i with energy μ as follows:

$$\eta_{res} = \frac{d\zeta_i(\mu)}{d\mu} = \sum_{\sigma,\sigma'} \psi^{S\dagger}_{i\sigma}(\mu) M_{\sigma,\sigma'} \psi^{S}_{i\sigma'}(\mu), \tag{2.63}$$

where $\psi_i^S(\mu)$ is an eigenstate of the Hamiltonian and M is a quantum operator. In order to calculate this quantity, it is necessary to find the scattering wave function of the system. First, let us from now on, simplify the notation of the scattering wave function ψ^S by removing the S upper script, so ψ will be the always the wave function unless mentioned otherwise. Kwant gives the wave function for a given system with the function kwant.wave_function, that returns the desired quantity for each mode for a given lead. For our purposes it is just necessary to calculate the wave function in one of the leads. A code snippet is shown below:

```
# Hf is the Hamiltonian of the system and EE is the energy of interest
wf = kwant.wave_function(Hf, energy=EE)
# 0 indicates the lead number and itinerant i the mode desired
phiw = wf(0)[i]
```

The n-th mode of the charge density response at energy μ for a system with spin degree of freedom is written as:

$$\rho_n(\mu) = e \sum_i |\psi^n_{i\uparrow}(\mu)|^2 + |\psi^n_{i\downarrow}(\mu)|^2$$

so, the total charge density response is

$$\rho_c(\mu) = e \sum_n \rho_n(\mu). \tag{2.64}$$

Note that in this case the quantum operator $M = \mathbb{1}$. The units of this quantity are coulombs per unit of energy.

In order to obtain the spin density response a similar procedure is followed. To obtain, the z-projected spin density response, we should replace M by the Pauli matrix σ^z. In a general form we have:

$$\rho^n_{s_M}(\mu) = \sum_i \begin{pmatrix} \psi^{n\dagger}_{i\uparrow}(\mu) \\ \psi^{n\dagger}_{i\downarrow}(\mu) \end{pmatrix}^T M \begin{pmatrix} \psi^{n}_{i\uparrow}(\mu) \\ \psi^{n}_{i\downarrow}(\mu) \end{pmatrix} \tag{2.65}$$

To calculate the z-projected spin density by replacing $M = \sigma^z$ we get:

$$\rho^n_{s_z}(\mu) = \sum_i |\psi^n_{i\uparrow}(\mu)|^2 - |\psi^n_{i\downarrow}(\mu)|^2, \tag{2.66}$$

the total z-projected spin density is then

$$\rho_{s_z}(\mu) = \sum_n \rho^n_{s_z}(\mu) \tag{2.67}$$

where we have to sum up over all n modes of the lead. For the spin density response in x and y direction the procedure is the same, but M should be replaced by σ^x in the former one and σ^y in the latter. This quantity is measured in units of inverse energy.

In Kwant the charge density and spin density response are easily calculated using the function kwant.operator.Density, that gives an object from which these quantities can be calculated. A code snippet is shown below.

```
# Hf is the Hamiltonian of the system and sz is a Pauli matrix
spin_z = kwant.operator.Density(Hf,sz)
# phiw is a scattering wave function from a determined lead and mode
ress_z = spin_z(phiw)
```

2.5.3 Spin current per unit energy j^s

In order to obtain the spin current expression, let us consider the time dependent Schrödinger equation, as well as its complex conjugate, so:

$$i\hbar\partial_t\psi_i = \sum_j H_{ij}\psi_j \tag{2.68}$$

$$-i\hbar\partial_t\psi_i^\dagger = \sum_j \psi_j^\dagger H_{ji}. \tag{2.69}$$

Multiplying Eq. (2.68) by $\psi_i^\dagger\boldsymbol{\sigma}$ and Eq. (2.69) by $\boldsymbol{\sigma}\psi_i$ we get

$$i\psi_i^\dagger\boldsymbol{\sigma}\hbar\partial_t\psi_i = \sum_j \psi_i^\dagger\boldsymbol{\sigma}H_{ij}\psi_j \tag{2.70}$$

$$-i\hbar\partial_t\psi_i^\dagger\boldsymbol{\sigma}\psi_i = \sum_j \psi_j^\dagger H_{ji}\boldsymbol{\sigma}\psi_i, \tag{2.71}$$

and by substracting Eq. (2.70) and Eq. (2.71), we find [89]:

$$(\psi_i^\dagger\boldsymbol{\sigma}\partial_t\psi_i + \partial_t\psi_i^\dagger\boldsymbol{\sigma}\psi_i) = \frac{1}{i\hbar}\sum_j(\psi_i^\dagger\boldsymbol{\sigma}H_{ij}\psi_j - \psi_j^\dagger H_{ji}\boldsymbol{\sigma}\psi_i), \tag{2.72}$$

where $\boldsymbol{\sigma} = (\sigma^x, \sigma^y, \sigma^z)$ is a vector composed by the Pauli matrices. This equation is the starting point to calculate the spin transfer torque, but for the moment let us consider only the right side of it, which is the spin current. Rewriting this expression we get

$$j_{ab}^{s_M}(\mu) = \frac{1}{i}\sum_n \left(\psi_a^{n\dagger}(\mu) M H_{ab}\psi_b^n(\mu) - \psi_b^{n\dagger}(\mu) H_{ba} M \psi_a^n(\mu)\right), \tag{2.73}$$

where we have summed up over all the modes of ψ. $j_{ab}^{s_M}$ is the M-projected spin current per unit energy from site b to site a. In the simplest cases M is a Pauli matrix. Remember that $\psi_a^{n\dagger}(\mu) = \left(\psi_{a\uparrow}^{n\dagger}(\mu), \psi_{a\downarrow}^{n\dagger}(\mu)\right)$ and $\psi_a^n(\mu) = \left(\psi_{a\uparrow}^n(\mu), \psi_{a\downarrow}^n(\mu)\right)^T$. Considering the spin current in along the y-direction without loss of generality, the components of the total spin current per unit energy through the region of interest are:

$$j_{xy}^s = \sum_{b,a} j_{ab}^{s_x}, \qquad j_{yy}^s = \sum_{b,a} j_{ab}^{s_y} \qquad \text{and} \qquad j_{zy}^s = \sum_{b,a} j_{ab}^{s_z}, \tag{2.74}$$

where j_{ij}^s are the components of the tensor j^s with $i = x, y, z$ running in spin space and $j = x, y, z$ in real space. Note that this quantity is unitless. In Kwant the total spin current per unit energy per spin projection is obtained using the function kwant.operator.Current. A code snippet is shown below.

```
# Hf is the Hamiltonian of the system and sz is a Pauli matrix
cur_z = kwant.operator.Current(Hf, sz)
# phiw is a scattering wave function from a determined lead and mode
curs_z = cur_z(phiw)
```

2.5.4 Spin transfer torque τ and generalization to spin dependent hoppings

In the steady state the spin density does not depend on time so the “usual” spin transfer equation can be written as [89, 90]:

$$\sum_{M,i'} (j_{i'}^{s_M} - j_{i'-1}^{s_M})\hat{e}_M = 2J\sum_{i'}(\boldsymbol{m}_{i'} \times \boldsymbol{S}_{i'}), \tag{2.75}$$

where $j_i^{s_M}$ is the M-projected spin current per unit energy between the site i and $i-1$, J is the magnetic exchange, $\boldsymbol{m}_i$ is the magnetization of the site i and $\boldsymbol{S}_i$ is the spin density response vector at the site i. This equation needs to be modified for a system with spin dependent hoppings, as in our case. In this section we derive in detail the STT equation of a linear chain with spin dependent hoppings and in Chapter 5 it will be generalized for a graphene system with spin dependent hoppings and sublattice potential considered in this thesis.

The left part of Eq. (2.72) can be obtained from $\partial_t(\psi_i^\dagger(\boldsymbol{\sigma}\cdot\boldsymbol{m}_i)\psi_i)$. So, let us define the spin density in the site i' as $\boldsymbol{S}_{i'} = \psi^\dagger_{i'}\boldsymbol{\sigma}\psi_{i'}$. For this section, we will use second quantization notation, i.e. $\psi^\dagger_i = (c^\dagger_{i\uparrow}, c^\dagger_{i\downarrow})$ and $\psi_i = (c_{i\uparrow}, c_{i\downarrow})^T$, where $c^\dagger_{i\sigma}$ $(c_{i\sigma})$ creates (annihilates) an electron with spin σ in the site i. The time derivative can be easily solved using the Ehrenfest theorem that states that $\partial_t A = \frac{1}{i\hbar}[A, H]$, so let's do it!

Linear chain with spin dependent hoppings

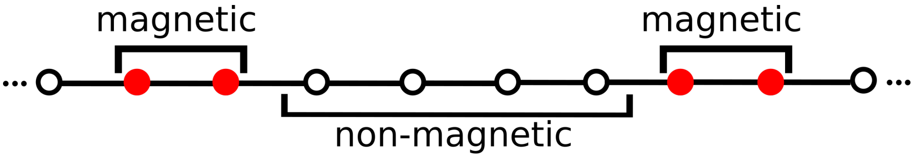

Figure 2.9: Infinite linear chain system composed by two magnetic regions separated by a non-magnetic region. The magnetic sites are represented in red and the non-magnetic ones are represented with black open circles.

In order to derive the extra terms from the spin current conservation equation when the system has spin dependent hoppings, let us consider the simplest possible system, the linear chain shown in Fig. 2.9, where the black (open) circles are non-magnetic sites and the red circles are magnetic sites that have magnetization $\boldsymbol{m}$. Because we are interested in the STT we are going to consider that the magnetizations of both magnetic regions are non-collinear. In this configuration we can write the system's Hamiltonian as:

$$H = H_0 + H_1 + H_2 + H_3 \tag{2.76}$$

with,

$$\begin{aligned} H_0 &= \sum_{i\alpha} \epsilon_i c^\dagger_{i\alpha} c_{i\alpha} \\ H_1 &= J \sum_{i\alpha\beta} c^\dagger_{i\alpha} (\boldsymbol{\sigma}\cdot\boldsymbol{m}_i)_{\alpha\beta} c_{i\beta} \\ H_2 &= t \sum_{\langle ij\rangle\alpha} c^\dagger_{i\alpha} c_{j\alpha} + c.c. \\ H_3 &= t' \sum_{\langle ij\rangle\alpha\beta} c^\dagger_{i\alpha} (\boldsymbol{\sigma}\cdot\boldsymbol{m}_i)_{\alpha\beta} c_{j\beta} + c.c., \end{aligned}$$

where H_0 is the onsite Hamiltonian and ϵ_i is the onsite potential in the site i, H_1 is the s-d Hamiltonian and J is magnetic exchange, H_2 is hopping Hamiltonian and t is the usual hopping term and H_3 is a Hamiltonian that models the spin dependent effects in the system, being t' the magnitude of the effect. Let us calculate now the commutator of the spin density $\boldsymbol{S}_{i'}$ for each term in Eq. (2.76). The commutator with H_0 is zero because both operators commute. Considering $\boldsymbol{\sigma} = \sigma^x\hat{e}_x + \sigma^y\hat{e}_y + \sigma^z\hat{e}_z$ and $\boldsymbol{m}_i = m^x_i\hat{e}_x + m^y_i\hat{e}_y + m^z_i\hat{e}_z$, we get:

$$[S_{i'}, H] = [S_{i'}, H_1] + [S_{i'}, H_2] + [S_{i'}, H_3].$$

The commutator of the first term on the right hand side is:

$$[S_{i'}, H_1] = \left[\sum_{\alpha'\beta'} c^\dagger_{i'\alpha'} \sigma_{\alpha'\beta'} c_{i'\beta'}, J \sum_{i\alpha\beta} c^\dagger_{i\alpha} (\boldsymbol{\sigma} \cdot \boldsymbol{m}_i)_{\alpha\beta} c_{i\beta} \right]. \tag{2.77}$$

Using the identity $[AB, CD] = A[B, C]D + [A, C]BD + CA[B, D] + C[A, D]B$ and considering, without loss of generality, only the first term of the spin density along the x direction we can expand Eq. (2.77) as:

$$\begin{aligned} \sum_{i\alpha'\beta'\alpha\beta} & c^\dagger_{i\alpha} \sigma^x_{\alpha'\beta'} [c_{i'\alpha'}, c^\dagger_{i\alpha} (\boldsymbol{\sigma} \cdot \boldsymbol{m}_i)_{\alpha\beta}] c_{i\beta} + [c^\dagger_{i\alpha'} \sigma^x_{\alpha'\beta'}, c^\dagger_{i\alpha} (\boldsymbol{\sigma} \cdot \boldsymbol{m}_i)_{\alpha\beta}] c_{i'\beta'} c_{i\beta} + \\ & + c^\dagger_{i\alpha} (\boldsymbol{\sigma} \cdot \boldsymbol{m}_i)_{\alpha\beta} c^\dagger_{i\alpha'} \sigma^x_{\alpha'\beta'} [c_{i'\beta'}, c_{i\beta}] + c^\dagger_{i\alpha} (\boldsymbol{\sigma} \cdot \boldsymbol{m}_i)_{\alpha\beta} [c^\dagger_{i\alpha'} \sigma^x_{\alpha'\beta'}, c_{i\beta}] c_{i'\beta'}. \end{aligned} \tag{2.78}$$

To solve these commutators, let us consider the fermionic commutator relations:

$$\begin{aligned} &[a_i, a^\dagger_j] = \delta_{ij}, \\ &[a^\dagger_i, a^\dagger_j] = [a_i, a_j] = 0. \end{aligned} \tag{2.79}$$

The second and third terms of Eq. (2.78) are zero and the rest give Kronecker deltas, then

$$\begin{aligned} =& J \sum_{i\alpha'\beta'\alpha\beta} c^\dagger_{i\alpha} \sigma^x_{\alpha'\beta'} \delta_{i',i} \delta_{\beta'\alpha} (\boldsymbol{\sigma} \cdot \boldsymbol{m}_i)_{\alpha\beta} c_{i\beta} - c^\dagger_{i\alpha} (\boldsymbol{\sigma} \cdot \boldsymbol{m}_i)_{\alpha\beta} \sigma^x_{\alpha'\beta'} \delta_{i',i} \delta_{\alpha',\beta} c_{i'\beta'} \\ =& J \sum_{\alpha'\alpha\beta} c^\dagger_{i'\alpha'} \sigma^x_{\alpha'\alpha} (\boldsymbol{\sigma} \cdot \boldsymbol{m}_{i'})_{\alpha\beta} c_{i'\beta} - c^\dagger_{i'\alpha'} (\boldsymbol{\sigma} \cdot \boldsymbol{m}_{i'})_{\alpha'\alpha} \sigma^x_{\alpha\beta} c_{i'\beta}. \end{aligned} \tag{2.80}$$

Remembering that $\boldsymbol{\sigma} \cdot \boldsymbol{m}_{i'} = m^x_{i'} \sigma^x + m^y_{i'} \sigma^y + m^z_{i'} \sigma^z$, one can express Eq. (2.80) in matrix form:

$$J \psi^\dagger_{i'} \{ \hat{e}_x (\sigma^x (m^x_{i'} \sigma^x + m^y_{i'} \sigma^y + m^z_{i'} \sigma^z) - (m^x_{i'} \sigma^x + m^y_{i'} \sigma^y + m^z_{i'} \sigma^z) \sigma^x) \} \psi_{i'} \tag{2.81}$$

and using the Pauli's matrices identity $[\sigma^a, \sigma^b] = 2i\epsilon_{abc}\sigma^c$, we get:

$$\psi^\dagger_{i'} \{ 2iJ \hat{e}_x (m^y_{i'} \sigma^z - m^z_{i'} \sigma^y) \} \psi_{i'}, \tag{2.82}$$

so finally, we can write

$$\begin{aligned}&[S_{i'}, H_1] = 2iJ\hat{e}_x \cdot (\boldsymbol{m}_{i'} \times \boldsymbol{S}_{i'}), \text{ or more generally}\\&[S_{i'}, H_1] = 2iJ(\boldsymbol{m}_{i'} \times \boldsymbol{S}_{i'}).\end{aligned} \tag{2.83}$$

To obtain $[S_{i'}, H_2]$ a similar procedure is followed. Let us consider again the spin density along the x direction:

$$[S_{i'}, H_2] = \left[\sum_{\alpha'\beta'} c^\dagger_{i'\alpha'}\sigma^x_{\alpha'\beta'}c_{i'\beta'}, t\sum_{\langle ij\rangle\alpha} c^\dagger_{i\alpha}c_{j\alpha} + c.c.\right], \tag{2.84}$$

following the steps of Eq. (2.78), we get

$$\begin{aligned}=&t\sum_{\alpha'\beta'}\sum_{\langle ij\rangle\alpha} c^\dagger_{i\alpha}\sigma^x_{\alpha'\beta'}[c_{i'\alpha'}, c^\dagger_{i\alpha}]c_{j\beta} + [c^\dagger_{i\alpha'}\sigma^x_{\alpha'\beta'}, c^\dagger_{i\alpha}]c_{i'\beta'}c_{j\beta}+\\&+ c^\dagger_{i\alpha}c^\dagger_{i\alpha'}\sigma^x_{\alpha'\beta'}[c_{i'\beta'}, c_{j\beta}] + c^\dagger_{i\alpha}[c^\dagger_{i\alpha'}\sigma^x_{\alpha'\beta'}, c_{j\beta}]c_{i'\beta'}.\end{aligned} \tag{2.85}$$

Using the commutator relations of Eq. (2.79) we get:

$$=t\left(\sum_{\alpha\alpha'} c^\dagger_{i'\alpha'}\sigma^x_{\alpha'\alpha}c_{j\alpha} - \sum_{\alpha\beta'} c^\dagger_{i\alpha}\sigma^x_{\alpha\beta'}c_{i'\beta'} + c.c.\right). \tag{2.86}$$

Defining the spin current $j^{s_d}_n$ as $j^{s_d}_n = it(\sum_{\alpha\beta} c^\dagger_{n\alpha}\sigma^d_{\alpha\beta}c_{n-1\beta} + c.c.)$ and considering $i = i' - 1$ we get

$$[S_{i'}, H_2] = \frac{1}{i}(j^{s_x}_{i'} - j^{s_x}_{i'-1}). \tag{2.87}$$

Let us solve the last commutator

$$[S_{i'}, H_3] = \left[\sum_{\alpha'\beta'} c^\dagger_{i'\alpha'}\sigma_{\alpha'\beta'}c_{i'\beta'}, t'\sum_{\langle ij\rangle\alpha\beta} c^\dagger_{i\alpha}(\boldsymbol{\sigma}\cdot\boldsymbol{m}_i)_{\alpha\beta}c_{j\beta}\right].$$

Following the steps of Eq. (2.77) we get:

$$\begin{aligned}[S_{i'}, H_3] =&t'\sum_{\alpha'\beta'}\sum_{\langle ij\rangle\alpha\beta} c^\dagger_{i\alpha}\sigma_{\alpha'\beta'}[c_{i'\alpha'}, c^\dagger_{i\alpha}(\boldsymbol{\sigma}\cdot\boldsymbol{m}_i)_{\alpha\beta}]c_{j\beta} + [c^\dagger_{i\alpha'}\sigma_{\alpha'\beta'}, c^\dagger_{i\alpha}(\boldsymbol{\sigma}\cdot\boldsymbol{m}_i)_{\alpha\beta}]c_{i'\beta'}c_{j\beta}+\\&+ c^\dagger_{i\alpha}(\boldsymbol{\sigma}\cdot\boldsymbol{m}_i)_{\alpha\beta}c^\dagger_{i\alpha'}\sigma_{\alpha'\beta'}[c_{i'\beta'}, c_{j\beta}] + c^\dagger_{i\alpha}(\boldsymbol{\sigma}\cdot\boldsymbol{m}_i)_{\alpha\beta}[c^\dagger_{i\alpha'}\sigma_{\alpha'\beta'}, c_{j\beta}]c_{i'\beta'},\end{aligned} \tag{2.88}$$

Using the fermionic commutator relations of Eq. (2.79) and after some algebra we get:

$$[S_{i'}, H_3] = t'\left(c^\dagger_{i'\alpha'}\sigma_{\alpha'\alpha}(\boldsymbol{\sigma}\cdot\boldsymbol{m}_{i'})_{\alpha\beta}c_{j\beta} - c^\dagger_{i\alpha}(\boldsymbol{\sigma}\cdot\boldsymbol{m}_{i'})_{\alpha\alpha'}\sigma_{\alpha'\beta'}c_{i'\beta'} + c.c.\right). \tag{2.89}$$

Let us rewrite the right part of Eq. (2.89) in matrix notation and ignore for the moment the constant t', so

$$\psi_{i'}^{\dagger}\boldsymbol{\sigma}(\boldsymbol{\sigma}\cdot\boldsymbol{m}_{i'})\psi_i - \psi_i^{\dagger}(\boldsymbol{\sigma}\cdot\boldsymbol{m}_{i'})\boldsymbol{\sigma}\psi_{i'} + h.c. \tag{2.90}$$

The matrices inside the fermionic operators do not commute, so cannot be directly used the spin current expression. In addition, they cannot be combined because the fermionic operators act on different sites. The trick to overcome this issue is to realize that

$$[(\boldsymbol{\sigma}\cdot\boldsymbol{m}_{i'}),\boldsymbol{\sigma}] = (\boldsymbol{\sigma}\cdot\boldsymbol{m}_{i'})\boldsymbol{\sigma} - \boldsymbol{\sigma}(\boldsymbol{\sigma}\cdot\boldsymbol{m}_{i'}) = -2i(\boldsymbol{m}_{i'}\times\boldsymbol{\sigma}), \tag{2.91}$$

so we can rewrite Eq. (2.90) as:

$$\psi_{i'}^{\dagger}\boldsymbol{\sigma}(\boldsymbol{\sigma}\cdot\boldsymbol{m}_{i'})\psi_i - \psi_i^{\dagger}\boldsymbol{\sigma}(\boldsymbol{\sigma}\cdot\boldsymbol{m}_{i'})\psi_{i'} + \psi_i^{\dagger}(2i(\boldsymbol{m}_{i'}\times\boldsymbol{\sigma}))\psi_{i'} + h.c. \tag{2.92}$$

where the first two terms corresponds to a spin current along the direction $\boldsymbol{\sigma}(\boldsymbol{\sigma}\cdot\boldsymbol{m}_{i'})$ that we will name as j^{s_λ}. The third term is very similar to what we found in Eq. (2.83), but this time the spin density depends on different sites of the magnetic region. Then we can write:

$$[S_{i'}, H_3] = \frac{1}{i}(j_{i'}^{s_\lambda} - j_{i'-1}^{s_\lambda}) + 2it'\sum_i(\boldsymbol{m}_{i'}\times\boldsymbol{S}_{ii'}). \tag{2.93}$$

Summing up all the values obtained for H_1, H_2 and H_3, finally we get that

$$\begin{aligned}\frac{1}{i\hbar}[S_{i'}, H] = \frac{2J}{\hbar}(\boldsymbol{m}_{i'}\times\boldsymbol{S}_{i'}) - \frac{1}{\hbar}\sum_M(j_{i'}^{\sigma_M} - j_{i'-1}^{\sigma_M})\hat{e}_M - \\ \frac{1}{\hbar}\sum_\lambda(j_{i'}^{s_\lambda} - j_{i'-1}^{s_\lambda})\hat{e}_\lambda + \frac{2t'}{\hbar}\sum_i(\boldsymbol{m}_{i'}\times\boldsymbol{S}_{ii'}).\end{aligned} \tag{2.94}$$

When summing over all the i' sites in the magnetic regions and its boundaries, to obtain the total torque, the term $\sum_{\lambda,i'} j_{i'}^{s_\lambda} - j_{i'-1}^{s_\lambda}$ goes to zero because it depends on $m_{i'}$ and outside the ferromagnets this term is zero, so we can disregard it, then

$$\frac{1}{i\hbar}\sum_{i'}[S_{i'}, H] = \frac{2J}{\hbar}\sum_{i'}(\boldsymbol{m}_{i'}\times\boldsymbol{S}_{i'}) - \frac{1}{\hbar}\sum_M(j_{i'}^{\sigma_M} - j_{i'-1}^{\sigma_M})\hat{e}_M + \frac{2t'}{\hbar}\sum_{i,i'}(\boldsymbol{m}_{i'}\times\boldsymbol{S}_{ii'}). \tag{2.95}$$

If the spin density is constant, it is $\partial_t S = 0$, we find the following equation

$$\boldsymbol{\tau} = \sum_{M,i'}(j_{i'}^{\sigma_M} - j_{i'-1}^{\sigma_M})\hat{e}_M = 2J\sum_{i'}(\boldsymbol{m}_{i'}\times\boldsymbol{S}_{i'}) + 2t'\sum_{i,i'}(\boldsymbol{m}_{i'}\times\boldsymbol{S}_{ii'}), \tag{2.96}$$

that relates spin transfer torque $\boldsymbol{\tau}$ calculated using the spin current per voltage with that one using the spin density response. When there is not spin dependent hopping the second term in the right is zero and it is obtained the usual STT expression.

Because both terms are equivalent, its calculation in Kwant can be done using any of them. If is chosen to get the torque using the spin current responses equation, the currents should be calculated using the function kwant.operator.Current. Conversely if it is used the equation with the spin density response, this quantity most be calculated using the function kwant.operator.Density and then perform the cross product with the magnetization m. Both results have to be exactly the same. The torque found with any of these methods is energy-dependent and unitless.

2.6 Spin dynamics, LLG equation

When applied an electrical current to a spin valve whose magnetic layers have non-collinear magnetizations as shown in Figure 2.10(a), the system will experience a torque due to the uncompensated component acquired when the electron changes its polarization when passing successively through the ferromagnets. This effect will be described in more detail in Chapter 4 and here we will just focus on the dynamical description of this effect. These torques are important for applications because depending on its magnitude, it allows to alter the magnetization direction by electrical means. In order to describe this process let us consider the Landau-Lifshitz-Gilbert (LLG) equation

$$\frac{\partial \boldsymbol{M_2}}{\partial t} = \boldsymbol{M_2} \times \frac{1}{\hbar S_0}\frac{\partial E}{\partial \boldsymbol{M_2}} + \alpha \boldsymbol{M_2} \times \frac{\partial \boldsymbol{M_2}}{\partial t} + \frac{I}{eS_0} g(\boldsymbol{M_2} \cdot \boldsymbol{M_1}) \boldsymbol{M_2} \times (\boldsymbol{M_1} \times \boldsymbol{M_2}), \tag{2.97}$$

where e is the electron charge, I the current flowing through the system, α is the Gilbert damping parameter and S_0 the total spin of the magnet considered. E is the magnetic energy, $\boldsymbol{M_1}$ and $\boldsymbol{M_2}$ are the magnetization of the magnetic layers and $g(\boldsymbol{M_2} \cdot \boldsymbol{M_1})$ is a function that mimics the torque created in the system. The first term is related to the external effects that have to be taken into account in the system, like an external electric field, anisotropy, demagnetization, etc. That is why we can replace the magnetic energy time derivative by an effective field H_{eff}, with $H_{eff} = \frac{1}{\hbar S_0}\frac{\partial E}{\partial \boldsymbol{M_2}}$. This substitution permits to obtain the usual expression of the LLG equation. The second term is a phenomenological damping term that takes into account the dissipation in the system and the last term is the well-known Slonczewski's spin transfer torque (STT) term and models the damping-like torque.

Figure 2.10(b) shows the direction of the different terms of Eq. (2.97). It shows that the STT is collinear to the damping term and that the effective field generate a term which is orthogonal to both. The STT direction depends on the direction of the current applied to the system. If the STT is in the same direction as the dumping term, the magnetic moments will shortly precess and rapidly decay to a more stable state. If the current is such that the STT is opposite to the dumping term but smaller than it, the magnetic moments will precess again but its decaying to a more stable state will take

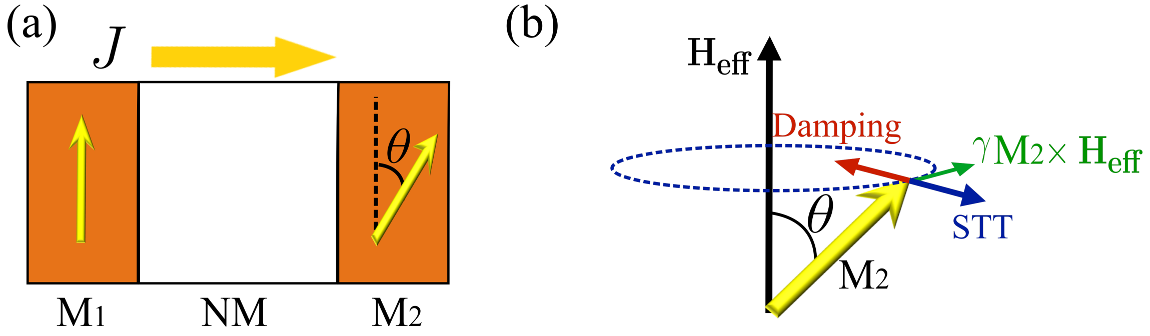

Figure 2.10: (a) Schematic representation of a spin valve with whose magnets have non-collinear magnetization. (b) Magnetic moment subject to a magnetic field and an electrical current. The STT term is collinear to the damping term and that the effective field generate a term which is orthogonal to both

longer. If both terms equilibrate each other, the system will reach a stable precession state, very useful for the generation of high frequency signals. If the STT term is bigger than the dumping term, then the system will precess in a sphere and the direction of the magnetic moments can be reversed completely. This property is very useful to achieve magnetic moment switching, a vital effect for the development of MRAM memories.

CHAPTER 3

Spin-dependent transport in lateral device with collinear magnetizations

---

In this chapter we present the results obtained for a graphene-based spintronic device. We demonstrate the existence of the proximity magnetoresistance (PMR) effect in graphene for four different MIs: YIG, CFO, EuO, EuS and the possibility of tuning this PMR by changing the electrical polarization of the multiferroic BFO. We found that in the case of MIs the systems are robust with respect to size dimensions and edge type termination and that the Rashba spin-orbit coupling does not significantly affect the results found for the Rashba parameters found in the literature. When considered BFO, we demonstrate that it is possible to tune the PMR by changing the electrical polarization of the material as well as, that the spin-orbit coupling do not affect greatly the PMR phenomena.

3.1 State of the art

Recent studies on inducing magnetism in graphene by proximity effects have shown that magnetic insulators (MI) are very suitable for this task. MIs are materials that exhibit some sort of magnetic ordering and are bad electrical conductors. The first work in this direction proposed the use of europium oxide (EuO) to induce ferromagnetism on graphene. H. Haugen and coworkers studied the conductance of a spin dependent square barrier, in order to mimic the presence of a MI on top of graphene and predicted a spin splitting value of 5meV [91]. EuS possesses a wide band gap around 1.65 eV and large exchange coupling $J \sim 10$ meV [66], that makes it a suitable material to induce ferromagnetism in graphene. The first experimental integration of EuO on graphene was achieved by molecular beam epitaxy using EuO layers with (001) orientation [92]. Even though, it was missing the demonstration of the actual spin splitting on graphene due to EuO that would confirm the graphene magnetization. The interest has been reinforced after a first principles calculations work on the spin-dependent properties of graphene in contact with EuO. H. X. Yang and coworkers found a bigger exchange splitting than the predicted of about 36 meV [63]. In addition, they found that the band structure preserved the linear band structure behavior of graphene, as well as, that depending on gating potential (Fermi energy position) the spins could be fully polarized what would give rise to a half metallic system. The experimental realization of the system Graphene/EuS showed that effectively graphene gets magnetized by EuS and field exchange values up to 100 T were reported. In addition, Shubnikov–de Haas oscillations proved the presence of quantum Hall states in the system, indicating a well-preserved Dirac band structure [66].

Other MIs attracted attention from the scientific community. For instance $Y_3Fe_5O_{12}$ (Yttrium iron garnet) has attracted significant attention. YIG is a ferrimagnetic compound that has a high Curie temperature, along with an intrinsic chemical stability at atmospheric conditions, what make it very suitable for the development of spintronic devices. Leutenantsmeyer and coworkers found changes in the non-local resistance of a graphene spin valve using Hanle precession and spin transport modulated with an in-plane exchange field that allow them to quantify a exchange splitting in graphene of 0.2 T [67]. In 2017 Hallal and coworkers published a systematic first principles study on magnetism induction in graphene by proximity effects, considering four MIs and their impact on the graphene band structure. The MIs considered were EuO, $CoFe_2O_4$ (cobalt ferrite), EuS (europium sulfite) and YIG. They found that all these materials can induce exchange splitting in graphene and presented magnitudes that ranges from tens to hundreds meV. In addition, they demonstrated the independence of the chalcogenides's spin splittings with respect to their thicknesses [82]. The spin splittings, energy gaps, and dopings reported in Ref. [82] were used in this work to create a mathematical model, that later was applied to a graphene spin valve to simulate electronic transport on it. We present the results of this calculation in section 3.2.2.

Other approaches to induce magnetism via proximity effects include the use of usual magnets and screen their conductivity interposing boron nitride layers (hBN). In Ref. [64] a first principles study of Gr/insulator/FM structures were proposed. Two different ferromagnets were considered, Cobalt (Co) and Nickel (Ni), as well as a different number of hBN layers. They found that this configuration also gives rise to spin splitting and reported that a spin switch as a function of the electric field, when Co is considered and is separated by two layers of hBN from graphene. The control of this switching can lead to the development of novel spintronic devices exploiting this phenomenon.

Another material of interest to consider is the multiferroic BFO, which has been possible to grow on graphene and for which has been found experimentally proximity exchange fields up to hundreds of Tesla [93]. In addition, tunability of the graphene-BFO system by adjusting the magnetic field was also demonstrated [94]. In our group this material has been studied to elucidate the role of the electric polarization in graphene-based spintronic devices. DFT calculations were performed to study the impact of BFO in the graphene band structure and transport calculations were performed to study electronic control of magnetic properties of this material. In this chapter we present the corresponding transport calculations to demonstrate a concept of multi-resistive device tunable via ferroelectric and magnetic control.

3.2 Proximity magnetoresistance induced by magnetic insulators on graphene

The advantage of using MIs over metallic ferromagnets to induce ferromagnetism, is due to conductivity mismatch present in magnetic metallic substrates that influences the spin injection and hamper the design of novel types of spin switches [82]. In this section we present the results corresponding to four different magnetic insulators: YIG, CFO, EuO and EuS. YIG is a ferrimagnetic material with low dumping and Curie temperature around 560 K. CFO is a ferrite with strong coercivity and is arranged in cubic spinel structure. It is a ferrimagnet and has a Curie temperature of 790 K. Both YIG and CFO present magnetic phase transition above room temperature. EuO has a crystal structure with a face centered cubic (FCC) and present ferromagnetism for temperatures below 77 K. EuS is arranged in a face centered cubic lattice like EuO and has a ferromagnetic behavior below 16.6 K. In Ref. [82] a graphene layer on top of any of the aforementioned materials is considered and it is necessary therefore increase the number of graphene unit cells in order to deal with the lattice mismatch. For a 2×2 EuO cell and a $\sqrt(3) \times \sqrt(3)$ EuS cell 3×3 graphene unit cell was considered. To fit a 1×1 YIG cell a 7×7 graphene unit cell and for a 1×1 CFO cell a 5×5 graphene unit cell were used. These values will be very important in order to fit correctly the DFT band structures reported in Ref. [82] and for our tight-binding model. Side views and top views of a graphene layer on top of the MIs under consideration with their respective number of cells is shown in Fig. 3.1.

3.2.1 Band structure fitting

The proof that graphene has been magnetized, is evidenced by spin splitting in its band structure. Hallal and coworkers demonstrated the possibility of achieving this by considering four different MIs: EuO and EuS that are low Curie temperature chacolgenides and two high Curie temperature ferrimagnetic insulators YIG and CFO [82]. They reported the different band structures obtained with its respective bands parameters, i.e. the energy separation of the spin up and spin down gaps, the spin splitting of the electron and hole bands and the doping energy. To fit their bands, let us first of write down the

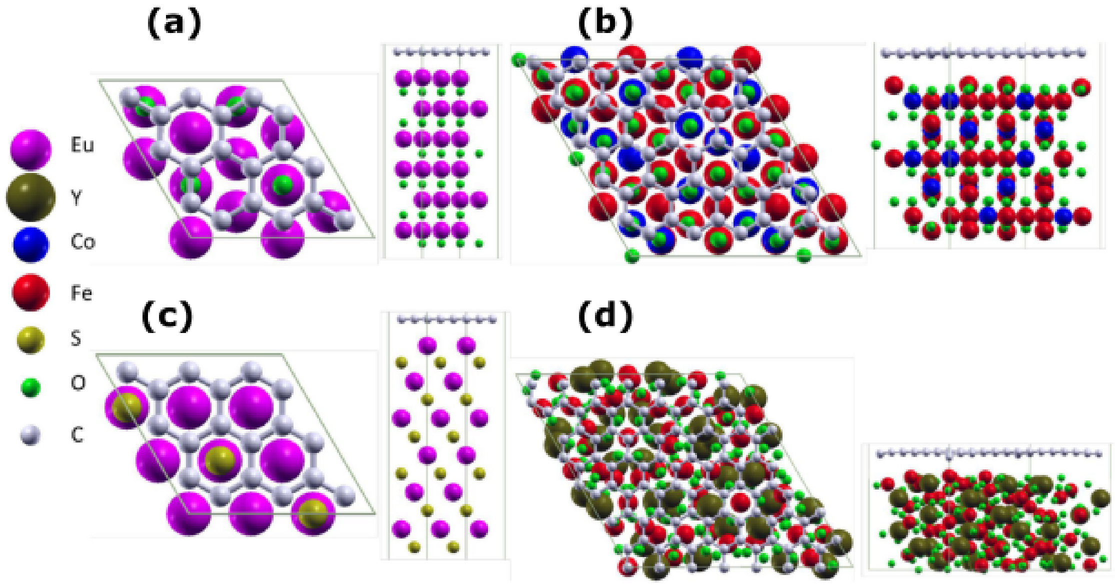

Figure 3.1: Side and top views of the system graphene MI using (a) EuO, (b) $CoFe_2O_4$ (c) EuS and (d) $Y_3Fe_5O_{12}$. Figure taken from Ref. [82].

Hamiltonian

$$\begin{split} H = \sum_{i\sigma}\sum_{l} t_{l\sigma} c^\dagger_{(i+l)1\sigma} c_{i0\sigma} + H.c. + \sum_{i\sigma\sigma'}\sum_{\mu=0}^{1} \left[\delta + (-1)^\mu \Delta_\delta\right] c^\dagger_{i\mu\sigma}[\vec{m}.\vec{\sigma}]_{\sigma\sigma'} c_{i\mu\sigma'} \\ + \sum_{i\sigma}\sum_{\mu=0}^{1}\left[E_D + (-1)^\mu \Delta_s\right] c^\dagger_{i\mu\sigma} c_{i\mu\sigma}, \end{split} \tag{3.1}$$

It is the same Hamiltonian presented in Eq. (2.26). Parameters δ, Δ_δ, Δ_s are defined via exchange spin-splittings δ_e (δ_h) of the electrons (holes) and spin-dependent band gaps Δ_σ, E_D indicates the Dirac cone position with respect to the Fermi level. $\delta = \frac{\delta_e+\delta_h}{2}$, $\Delta_s = \frac{\Delta_\downarrow+\Delta_\uparrow}{2}$ and $\delta = \frac{\delta_e-\delta_h}{2} = \frac{\Delta_\downarrow-\Delta_\uparrow}{2}$. The corresponding parameters for all the MIs considered are summarized in Table 3.1. $c^\dagger_{i\mu\sigma}$ ($c_{i\mu\sigma}$) creates (annihilates) an electron of type $\mu = 0$ for A and $\mu = 1$ for B sites on the unit cell i with spin $\sigma =\uparrow$ ($\downarrow$) for up (down) electrons. $\vec{m}$ and $\vec{\sigma}$ respectively represent a unit vector that points in the direction of the magnetization and the vector of Pauli matrices, so that $\vec{m}\cdot\vec{\sigma} = m_x\sigma^x + m_y\sigma^y + m_z\sigma^z$. The anisotropic hopping $t_{l\sigma}$ connects the i cell with its nearest neighbor one $i + l$ with spin σ.

It is important to mention that in order to get the correct value for the hoppings it is necessary to consider separately each spin contribution, so the hoppings are spin dependent. For the particular case of graphene on top of CFO, it is necessary to consider presence of superficial tension in the interface between graphene and CFO, that creates anisotropy in the hoppings, so they will depend on the hopping direction. Besides the number of graphene cells and its lattice parameter for each magnetic insulator, it is important to include units conversion from SIESTA's default units (Bohr units) to angstroms

Table 3.1: Extracted energy gaps and exchange splitting from Ref. [82]. $\varDelta_\uparrow$ and $\varDelta_\downarrow$ are the spin up and spin down gaps, δ_e and δ_h are the spin splitting of the electron and hole bands. E_D is the doping of the bands.

Structure	$\varDelta_\uparrow$ (eV)	$\varDelta_\downarrow$ (eV)	δ_e (eV)	δ_h (eV)	E_D (eV)	Package	Scale factor
Gr/EuS	0.192	0.16	0.023	-0.01	-1.3	SIESTA	$3 \times 1.889 \times 2.445$
Gr/EuO	0.134	0.098	0.084	-0.048	-1.37	SIESTA	$3 \times 1.889 \times 2.42$
Gr/YIG	0.116	0.052	-0.052	-0.115	-0.78	SIESTA	$7 \times 1.889 \times 2.54$
Gr/CFO	0.012	0.008	-0.045	-0.049	0.49	VASP	$5 \times 1 \times 2.46$

(1 Å= 0.5292 Bohrs). Finally, the scale factor for the bands obtained with SIESTA (EuS, EuO, YIG) is $N_{cells} \times U_{factor} \times a'_{cc}$, where N_{cells} is one side of the graphene cell units, U_{factor} is the conversion factor from inverse Bohr units to inverse angstroms equal to 1.889 and a'_{cc} is the graphene lattice constant found after relaxation. For the band structure obtained using VASP (CFO) $U_{factor} = 1$. This information is summarized as well in Table 3.1. Taking this into account it is possible to get the correct velocities of the electrons and the corresponding hoppings used in Hamiltonian of Eq. (3.1) which are reported in Table 3.2. Because the hopping parameters in YIG, EuS and EuO are not anisotropic in the Hamiltonian from Eq. (3.1) the subindex l can be disregarded and consider $t_{l\sigma} = t_\sigma$. By other hand, CFO has anisotropic hoppings, so for each nearest neighbor we have a different hopping parameter that we represent as t_1, t_2 and t_3. A cartoon showing the different hoppings in a graphene lattice is shown in the inset from Fig. 3.2(b).

Table 3.2: Hopping parameters used in Eq. (3.1) for each magnetic insulator considered.

Material	Hopping direction	spin up (eV)	Average R-squared	spin down (eV)	Average R-squared
YIG	t	3.6	0.971	3.8	0.966
CFO	t_1	1.38	0.946	1.44	0.962
	t_2	$1.41e^{-i0.01}$		$1.48e^{-i0.01}$	
	t_3	$1.36e^{-i0.02}$		$1.44e^{-i0.02}$	
EuS	t	4.5	0.985	4.8	0.985
EuO	t	4.9	0.958	4.3	0.958

The results of the fitting are shown in Fig. 3.2 for (a) YIG, (b) CFO, (c) EuS, (d) EuO. It can be seen a good agreement with respect to the bands obtained with DFT (dotted bands). The corresponding error analysis will be presented in the next subsection.

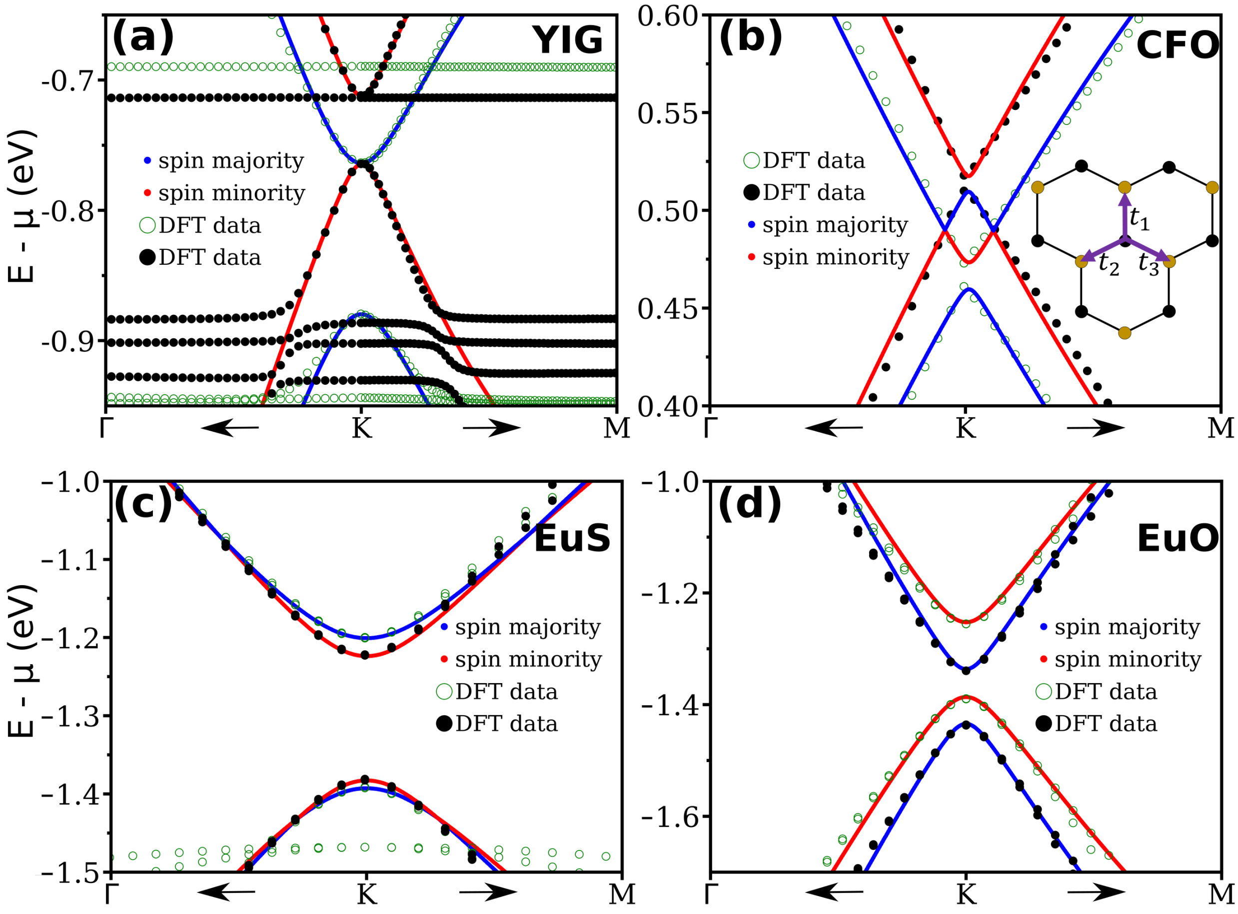

Figure 3.2: Band structure obtained using the tight-binding Hamiltonian defined by Eq. (3.1) (solid lines) fitted to the band structure from DFT spin-majority (green open circles) and spin-minority (black filled circles) data for the cases with (a) YIG, (b) CFO, (c) EuS, and (d) EuO from Ref. [82]. The inset in (b) shows the anisotropic hoppings reported in Table 3.1.

Error analysis

In order to quantify the fitting quality we calculated the R-squared value for each curve and averaged over the same spin species. Having R^2 close to 1 indicates good fit. On the contrary if it is close to 0 the fitting is not good at all. Mathematically this coefficient is defined as:

$$R^2 = 1 - \frac{\sum_i (y_i - y_i^f)^2}{\sum_i (y_i - \bar{y})^2}, \tag{3.2}$$

where y are the theoretical values, y^f are the fitted ones and $\bar{y}$ is the average of the y values. The corresponding R^2 values obtained for each material and spin species are presented in Table 3.2.

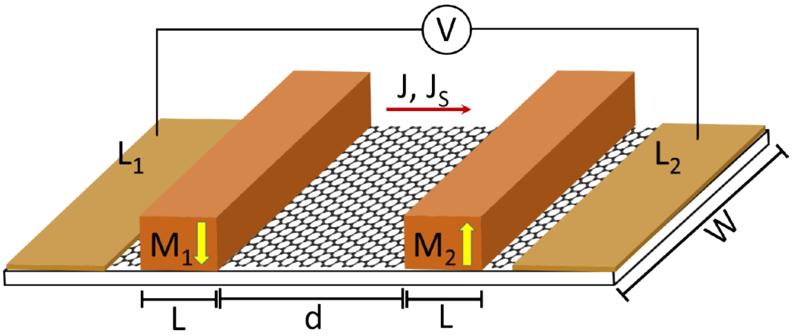

Figure 3.3: Lateral spintronic device comprising two magnetic insulators on top of a graphene sheet. The magnetic graphene regions have a length L, width W, and they are separated by a distance d.

3.2.2 Towards proximity magnetoresistance (PMR) effect

In order to be able to use graphene in spintronics, it is crucial to achieve methods to magnetize it, without harming its high conductivity or its long spin relaxation time and lengths. The method should be robust, preserve the integrity of the graphene lattice structure and the magnetization produced should be uniform. In addition, it is desired to induce a suitable SOC interaction into the system, essential for the spin manipulation. All these conditions can be met using MI proximity induced magnetism and this is the only mechanism considered in this thesis. We will now explore this proximity induced magnetism in order to propose a novel type of transport phenomenon called proximity magnetoresistance.

Proximity magnetoresistance (PMR) [95] is demonstrated and studied in the graphene-based lateral valve shown in Figure 3.3. The system comprises two identical proximity-induced magnetic regions of width W and length L resulting from insulators with magnetizations M_1 and M_2, separated by a distance d of the non-magnetic region of a graphene sheet with armchair edges. Both magnetic graphene regions are separated from the leads L_1 and L_2 by a small pure graphene region.

In order to simulate the system shown in Fig. 3.3, we employ Kwant for the different MIs under consideration. It is important to take into account the different energy ranges for which our Hamiltonian is valid, which is close to the Fermi energy. Second, when one wants to calculate the conductance at different temperatures it is essential to remember that each material has different Curie temperatures for which below it the materials still induce magnetism on graphene. With the aim to calculate the conductance for temperatures different from zero we use Eq. 2.60

$$G = \frac{e^2}{h}\sum_{\sigma}\int T^{\sigma}_{P(AP)}\left(-\frac{\partial f}{\partial E}\right) dE,$$

where $T^{\sigma}_{P(AP)}$ indicates the spin-dependent transmission probability for parallel(antiparallel) magnetization configurations. In Figure 3.4 presents the band structure, the transmission at $T = 0$ K and the corresponding conductance for different temperatures, considering temperatures below the Curie temperature of (a1-a3) YIG (b1-b3) CFO (c1-c3) EuS and (d1-d3) EuO. The band structures were calculated considering fully magnetized semi-infinite systems (a1-d1), while the transmissions and conductances were obtained considering a system with dimensions $L = 49.2$ nm, $W = 39.6$ nm, and $d = 1.5$ nm, for two different magnetic configurations, parallel (P) and antiparallel (AP) was considered. One can see that in the energy range between -0.88 and -0.78 eV there is no majority-spin state present and the only contribution to transmission is $T^{\downarrow}_{P}$ from the minority-spin channel. Similarly, between -0.72 and -0.75 eV, but this time the only contribution $T^{\uparrow}_{P}$ is from the majority-spin channel. This transmission behavior corresponds to the band structure calculated showed in Fig. 3.4(a1). The corresponding conductances for the parallel (G_P) and antiparallel (G_{AP}) magnetic configurations at T = 300 K are shown in Fig. 3.4(a3). Since the gaps are much smaller for both spin channels in CFO resulting in much narrower/vanishing regions with half-metallic behavior in contrast with YIG case as seen in Fig. 3.4(b1-b2) for zero temperature. At room temperature the smearing makes these half-metallic regions vanish similar to YIG as seen in Fig. 3.4(b3). For the EuS, the transmission in the energy range from -1.22 to -1.37 eV shows no any contribution to conductance (Fig. 3.4(c2)) in agreement with band structure in Fig. 3.4(c1). The temperature chosen to calculate the conductance is 16 K, very close to the Curie temperature of the material. One can see that the corresponding conductance look similar to that at 0 K as shown in Fig. 3.4(c3). For the EuO case, presented in Fig. 3.4(d2), the minority-spin channel $T^{\downarrow}_{P}$ does not contribute to the transmission in the energy range between -1.34 and -1.42 eV. Similarly, in the energy range between -1.26 and -1.38 the majority-spin channel $T^{\uparrow}_{P}$ does not contribute to the transmission. In the cross-section of both regions (from -1.34 to -1.38 eV) there is no transmission because there is a gap, that can be seen as well in the band structure in Fig. 3.4(d1). When considered the conductance at temperature T= 70 K, one can see that the conductance smoothened and that both parallel and antiparallel conductances (G_P and G_{AP}) conserve its zero value around the gap.

Using these findings, we can now introduce the proximity magnetoresistance as a function of energy comparing for all this cases in Fig. 3.5 at T=0 K and at T=300 K for YIG and CFO, 16 and 70 K for EuS and EuO, respectively. This quantity is defined using conductances from the parallel and antiparallel case according to the following definition:

$$\mathrm{PMR} = \left(\frac{G_P - G_{AP}}{G_P + G_{AP}}\right) \times 100\% \tag{3.3}$$

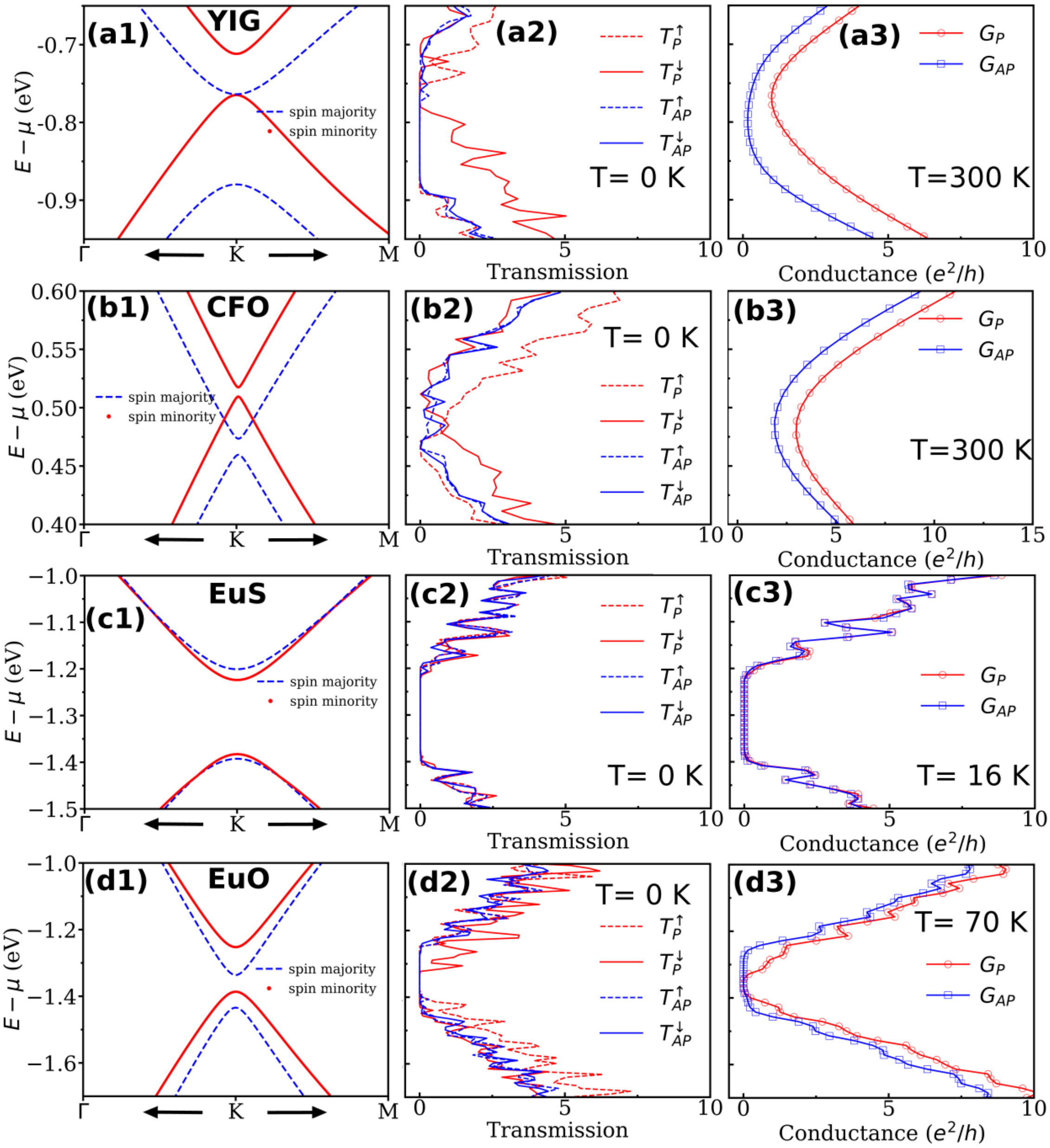

Figure 3.4: Comparison of band structures, transmissions and conductances for (a1)-(a3) YIG, (b1)-(b3) CFO, (c1)-(c3) EuS and (d1)-(d3) EuO. The band structures were reproduced using the DFT parameters from Ref. [82] for graphene in proximity to the MI under consideration. The transmission probabilities for majority (dashed lines) and minority (solid) spin channel for parallel (red) and antiparallel (blue) magnetization configurations were calculated for a system with dimensions L = 49.2 nm, W = 39.6 nm, and d = 1.5 nm at T = 0 K. The conductance was for a system at 300 K for YIG and CFO and 16 K and 70 K for EuS and EuO respectively. The parallel and antiparallel magnetization configurations are presented in red circles and blue squares respectively.

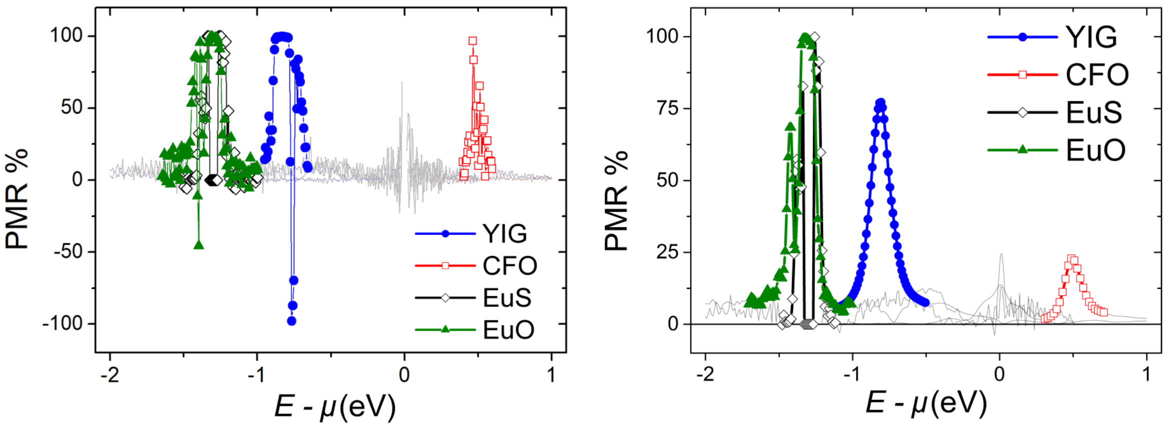

Figure 3.5: Proximity magnetoresistance defined by Eq. 3.3 as a function of energy with respect to the Fermi level for YIG (blue circles), CFO (red squares), EuS (black diamonds), and EuO (green triangles) at (a) $T = 0$ K and (b) using temperature smeared conductances at T = 300, 300, 16, and 70 K, respectively. System dimensions are L = 49.2 nm, W = 39.6 nm, and d = 1.5 nm.

At T= 0 K all cases present a value close to 100 % at energies showing half-metallic behavior discussed above as shown in Fig. 3.5(a). Only EuS and EuO conserved their maximum value due to the fact that the temperature is still low as seen in Fig. 3.5(b). At room temperature, for a YIG-based structure we found a maximum PMR value of 77%, while for CFO it is 22%. We can conclude that among all materials considered, YIG represents the most suitable candidate for lateral spintronic applications due to both high Curie temperature and a considerably large PMR value at room temperature. In order to demonstrate the PMR robustness with respect to system dimensions, in the next subsection we will present results regarding the influence of the length L the separation d and the width W on the PMR.

Robustness of PMR with respect to system dimensions

It is well-known that the size of the graphene nanoribbon affects its electronic behavior, that is why this study is mandatory in order to understand the limit of our predictions. In Fig. 3.6 we present the PMR dependences with respect to length L, width W, and separation d for a system with armchair edges for (a1)-(a3) YIG, (b1)-(b3) CFO, (c1)-(c3) EuS and (d1)-(d3) EuO. When L is increased the PMR has a clear tendency to increase for all cases until it saturates. With respect to the width W the PMR present oscillations, but they vanish for wide enough systems. These oscillations depend on edge termination type, and they are more pronounced for a system with armchair edges compared to zigzag or rough edges (not shown). These oscillations are due to quantum confinement, so it is expected to have smaller oscillations for larger W as can be clearly seen in the figure. On the contrary, the PMR shows almost constant behavior as a function of separation between the magnets d due to the fact that transport is in a ballistic regime. In Fig. 3.6(a4-d4), we summarize this dependencies at energies when PMR is maximum as a function of L, W and d. These energy values are highlighted by the dashed line presented in the panels and are for (a4) YIG at -0.81 eV, for (b4) CFO at 0.49 eV, for (c4) EuS at -1.286 eV and for (d4) EuO at -1.286 eV. Of vital importance is the green square in each figure that denotes the region where the PMR is independent of the system dimensions. This statement is valid for bigger systems limited by the spin diffusion length of graphene.

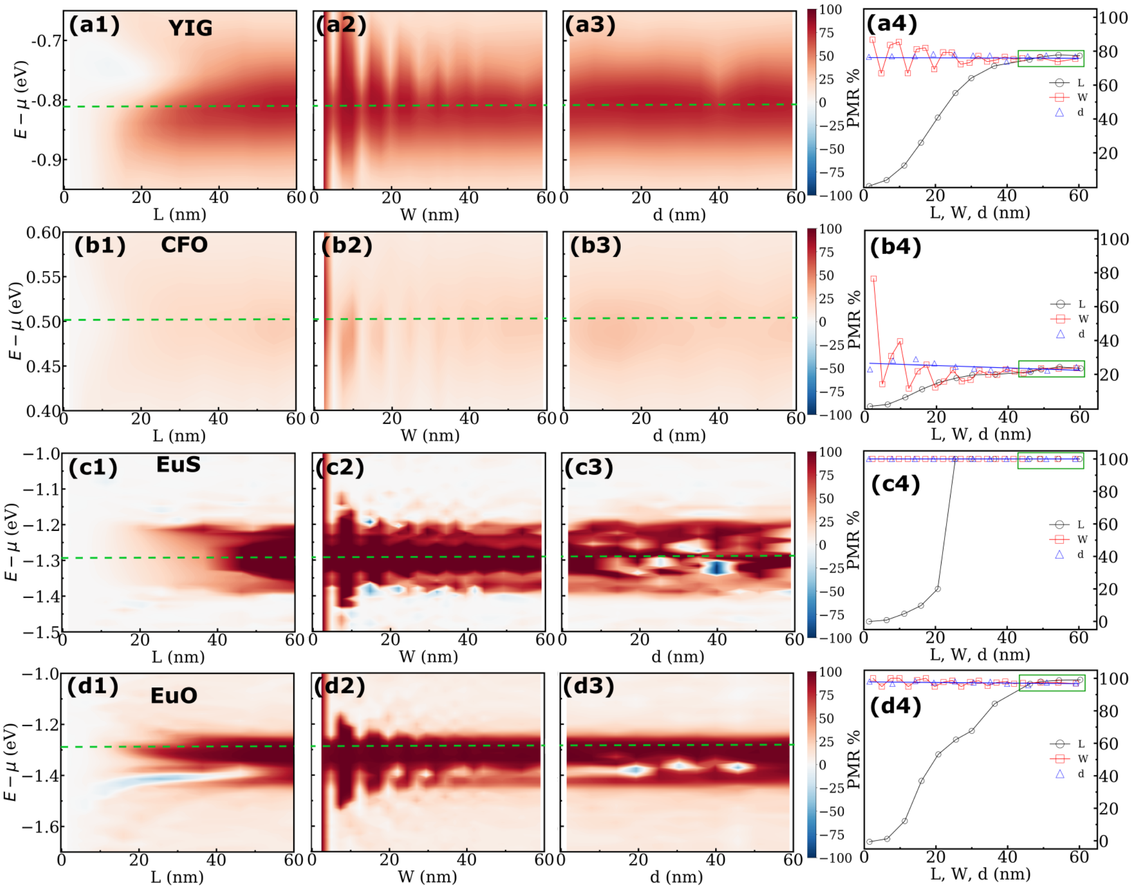

Figure 3.6: PMR profiles as a function of L, W, and d for a system with armchair edges, as well as, the dependence of PMR for the energy outlined by a dashed line as a function of L (black circles), W (red squares), and d (blue triangles) for (a1)-(a4) YIG (b1)-(b4) CFO (c1)-(c4) EuS and (d1)-(d4) EuO. The green square highlights the region where PMR becomes independent of system dimensions.

Robustness of PMR with respect to edge terminations and spin-orbit coupling SOC

Now that we have demonstrated the robustness of the PMR with respect to system dimensions, another important aspect to take into account is edge termination, which is a well-known feature that modifies the graphene electronic behavior as has been already presented in section 1.4.1. In addition, we consider the impact of spin-orbit coupling on the PMR. Despite weak SOC within graphene, the proximity of adjacent materials can induce the interfacial Rashba SOC [39]. As a matter of simplicity and to highlight its potential for applications, we will focus our study on the PMR spin valve system with magnets made of YIG. Fig. 3.7(a) shows the dependence of PMR with respect to armchair, rough and zigzag edges. To create the rough edges we randomly removed the atoms at the edges and averaged over 20 different systems. The PMR maximum value shifts with respect to the edge termination is the result of the influence of the edge on the conductance of the system. It is clear that the maximum PMR value does not present a significant variation, maintaining for all three cases PMR values around 75%. With this result at hand, we can claim that the PMR is indeed robust with respect to edge termination type.

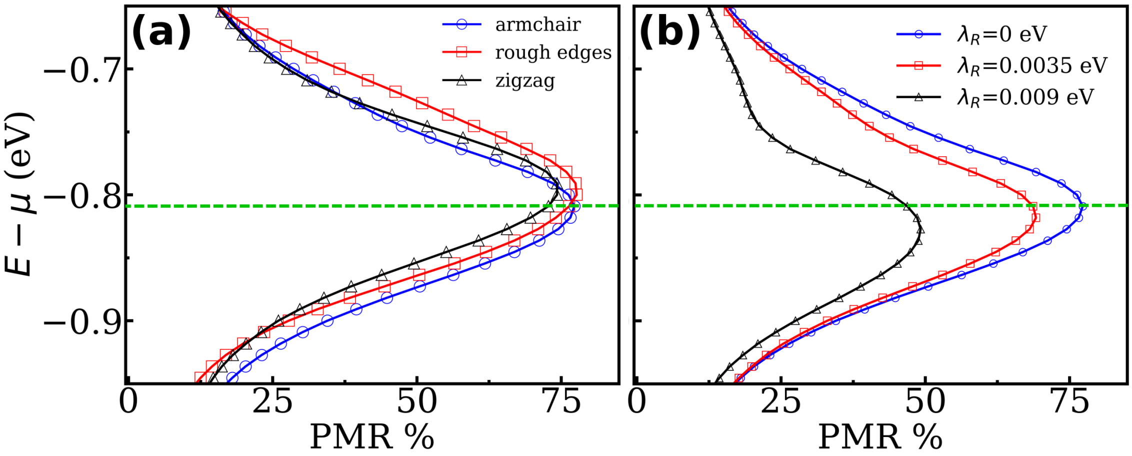

Figure 3.7: (a) PMR for a device of dimensions $L = 49.2$ nm, $W = 39.6$ nm and $d = 1.5$ nm with armchair (blue circles), rough (red squares) and zigzag (black triangles) graphene edge termination. (b) PMR dependencies for three values of Rashba SOC parameter λ_R defined by Eq. (3.4) for YIG-based system with armchair edges. The dashed line is a guide to the eye that shows the maximum value when $\lambda_R = 0$ eV.

SOC is a key effect for spin manipulation, i.e. for the generation of spin current from charge current and vice versa through Edelstein effects [96, 97]. Different materials have been considered to enhance the SOC strength in graphene and the variety ranges from metals [98, 99], semiconductors like the transition metals dichalcogenides (TMDCs) [100–102] and even topological insulators [103–105]. Due to its high Curie temperature, YIG is a very promising material and experimentally it has been found an enhanced SOC parameter $\lambda_R < 12$ meV [106]. In order to calculate the effect of Rashba SOC into our system it is necessary to add to our Hamiltonian from Eq. 2.26 the following term:

$$H_{SO} = i\lambda_R \sum_{i\sigma\sigma'} \sum_{l} c^{\dagger}_{(i+l)1\sigma}[\sigma^x_{\sigma\sigma'} d^x_l - \sigma^y_{\sigma\sigma'} d^y_l] c_{i0\sigma'} + H.c., \tag{3.4}$$

where λ_R is the Rashba spin-orbit coupling strength and the vector $\vec{d_l} = (d_l^x, d_l^y)$ connects the two nearest neighbors. The values of λ_R generally lie in the range between 1-10 meV (see, for instance, in Ref. [107]). Keeping in mind this information, we present in in Fig. 3.7(b) the PMR dependences for three values of Rashba SOC. One can see that increasing the strength of SOC λ_R lower the PMR. This behavior is expected and could be attributed to the fact that Rashba SOC mixes the spin channels. These dependencies allows us to conclude that PMR is quite robust also against SOC and even in the worst scenario remains of the order of 50 %, what make it very suitable for the experimental realization of the system proposed.

3.3 Multiferroic control of transport: proximity electro- (PER), magneto- (PMR) and multiferroic (PMER) resistances

By definition multiferroic materials combine a ferroic characteristic as ferromagnetism, which is the spontaneous magnetization ordering and whose orientation can be changed with a magnetic field, ferroelectricity, which is the spontaneous ordering of electric dipoles and can be changed by an electrical current, and ferroelasticity, which is the presence of spontaneous strain in the material and whose phase can be changed by applying stress [108]. Just a while ago, it was thought that using this kind of materials to create magnetic tunnel junction (MTJs), devices comprising two magnetic materials separated by an insulator, were not possible due to size device discrepancy as a result of the typical dimensions where occurs the quantum tunneling and the ferroelectricity [109]. However, recent studies have demonstrated the possibility of having ferroelectricity phenomenon at atomic scales, permitting the realization of MFTJ devices and attracting attention for its use in other kind of devices.

In this thesis we considered BFO, a multiferroic that presents ferromagnetism as well as ferroelectricity. BFO is a material arranged in perovskite type structure and both ferromagnetism and ferroelectricity phases are present above room temperature. It is an antiferromagnetic material whose Néel temperature is 643 K and its ferroelectricity properties can be conserved up to 1100 K [108]. In BFO the antiferromagnetism appears because of the unpaired electrons of the d shells of the iron atoms (Fe^{3+}). The ferroelectricity is the result of the existing shift of the Fe^{3+} atoms with respect to the Bi^{3+} in the unit cell [110]. Our aim is to study the multiferroic-induced proximity effect (MFPE) in graphene in the same system configuration from Fig. 3.3 used for the MIs. The use of this kind of spintronic devices opens the possibility of manipulating electrons through the intrinsic electric polarization present in the multiferroic, gaining another degree of freedom.

To obtain the DFT band structure for BFO in contact with graphene is necessary to proceed carefully. In order to simulate both electrical polarization states (up and down), one graphene sheet was placed at the bottom and upper interfaces perpendicular to the BFO electrical polarization as shown in Fig. 3.8(a). When considered the a BFO (111) the mismatch found between the lattice parameters of graphene and BFO was around 1.5%. For the sake of assuring no interaction between graphene layers and to maintain the polarization in the ferroelectric slabs, a thick BFO slab was considered [83]. In this configuration it is possible to obtain simultaneously the band structure for both electrical polarizations by performing only one calculation. For more details on the DFT calculations, please see reference [83].

Before starting the modeling our spintronic device we need to find first the best fitting parameters for our tight-binding model, exactly the same procedure followed in the previous section. The bands to fit are presented in Fig. 3.8 (b) in the shaded region. The top shaded region corresponds to the tail graphene layer while the bottom one to the head graphene region. From this figure it is possible to see the spin splitting caused by the presence of BFO. Both graphene sheets have negative doping due to the accumulation of negative charges as a response to the positive bound charges at both BFO interfaces. The electrostatic interaction of the head interface is stronger than that of the tail interface, this is reflected by the doping value found for the former one. In the next subsection we present the tight-binding band fitting of the DFT results.

3.3.1 Band structure fitting

Our Hamiltonian model is once again given by Eq. (2.26):

$$\begin{aligned} H = \sum_{i\sigma}\sum_{l} t_{l\sigma} c^{\dagger}_{(i+l)1\sigma} c_{i0\sigma} + H.c. + \sum_{i\sigma\sigma'}\sum_{\mu=0}^{1} \left[\delta + (-1)^{\mu} \Delta_{\delta}\right] c^{\dagger}_{i\mu\sigma} [\vec{m}.\vec{\sigma}]_{\sigma\sigma'} c_{i\mu\sigma'} \\ + \sum_{i\sigma}\sum_{\mu=0}^{1} \left[E_D + (-1)^{\mu} \Delta_{s}\right] c^{\dagger}_{i\mu\sigma} c_{i\mu\sigma}, \end{aligned} \tag{3.5}$$

where parameters δ, Δ_δ, Δ_s are defined via exchange spin-splittings δ_e (δ_h) of the electrons (holes) and spin-dependent band gaps Δ_σ, E_D indicates the Dirac cone position with respect to the Fermi level. $\delta = \frac{\delta_e+\delta_h}{2}$, $\Delta_s = \frac{\Delta_\downarrow+\Delta_\uparrow}{2}$ and $\delta = \frac{\delta_e-\delta_h}{2} = \frac{\Delta_\downarrow-\Delta_\uparrow}{2}$ as in the previous section.

In order to simulate spin-orbit coupling in the system will be used again Eq. 3.4

$$H_{SO} = i\lambda_R \sum_{i\sigma\sigma'}\sum_{l} c^{\dagger}_{(i+l)1\sigma} [\sigma^x_{\sigma\sigma'} d^x_l - \sigma^y_{\sigma\sigma'} d^y_l] c_{i0\sigma'} + H.c.,$$

Fig. 3.9 shows the fitting of our tight-binding model for both Gr$_{P.tail}$ and Gr$_{P.head}$ without SOC (a) and (b), and with SOC (c) and (d), respectively. One can see that

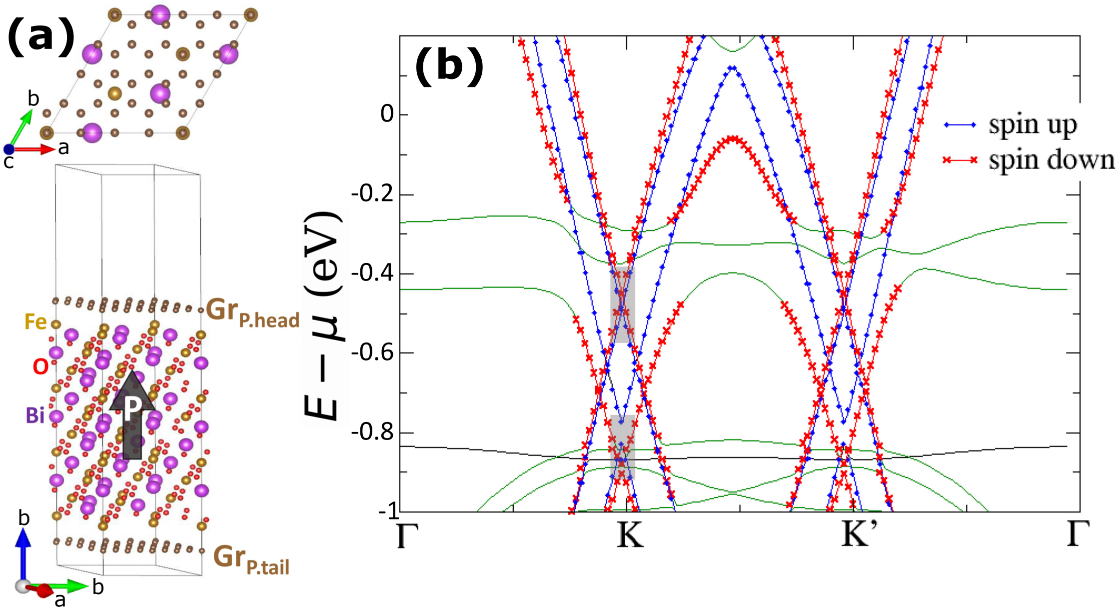

Figure 3.8: (a) Top view and lateral view of the $Gr_{P.head}$/BFO/$Gr_{P.tail}$ supercell. The magenta, gold and red balls designate Bi, Fe and oxigen atoms. (b) Band structure calculated of the $Gr_{P.head}$/BFO/$Gr_{P.tail}$ supercell without spin-orbit coupling. The cones that appear one on top of the other in the shaded region are a consequence of the presence of the two graphene layers at the interfaces of the BFO slab. The top and bottom shaded regions correspond to $Gr_{P.tail}$ and $Gr_{P.head}$, respectively.

Gr$_{P.tail}$ band in (a) conserves its linear band structure behavior, while Gr$_{P.head}$ in (b) do not. This behavior is due to its proximity with the BFO slab. In addition, another signature of this proximity is the fact that in order to fit the Gr$_{P.head}$ bands, we needed to include anisotropic hoppings, that indicates a strong influence of the BFO slab on it. When SOC is included the main feature we see is the additional band gap opening shown in (c) and (d) that we denote by γ_{SOC} at the spin up/spin down crossings. The gaps values 4 and 5 meV for Gr$_{P.head}$ and Gr$_{P.tail}$ correspond to a Rashba spin-orbit strength of 8.7×10^{-3} and 7.5×10^{-3}, respectively. The fitted values are presented in Table 3.3 for Gr$_{P.head}$ and Gr$_{P.tail}$, as well as, when SOC is included. The values obtained permitted to get a good agreement to the DFT bands reflected by the average R-squared (R^2) found for each using Eq. 3.2 whose values are reported in Table 3.4. With these results in hands, let us now perform transport calculations in our spin valve.

3.3.2 Proximity induced phenomena: Proximity magnetoresistance (PMR), proximity electroresistance (PER) and proximity multiferroic resistance (PMER)

To properly use Kwant to calculate the conductance of multiferroic spintronic device, we need to include the new degree of freedom besides the effect of the temperature at which

	E_G	$\varDelta_\uparrow$	$\varDelta_\downarrow$	δ_e	δ_h	E_D	γ_{soc}
Gr$_{P.head}$	-4.86×10^{-2}	5.5×10^{-2}	2.6×10^{-2}	1.04×10^{-1}	7.5×10^{-2}	-0.85	4×10^{-3}
Gr$_{P.tail}$	-3.4×10^{-2}	6×10^{-3}	1.5×10^{-3}	-3.5×10^{-2}	-4×10^{-2}	-0.47	5×10^{-3}

Table 3.3: DFT extracted energy gaps and exchange splitting parameters of $Gr_{P.head}$ and $Gr_{P.tail}$ at Dirac point for Gr/BFO/Gr heterostructure. E_G is the band-gap of the Dirac cone, $\varDelta_\uparrow$ and $\varDelta_\downarrow$ are the spin-up and spin-down gaps respectively. δ_e and δ_h are the spin-splitting of the electron and hole bands at the Dirac cone respectively. E_D is the Dirac cone position with respect to Fermi level. γ_{soc} denotes the spin-orbit band opening at the avoided crossing of the spin-up and spin-down bands. All the values presented are given in eV.

Material	Hopping direction	spin up (eV)	Average R-squared	spin down (eV)	Average R-squared	λ_R
Gr$_{P.head}$	t_1	2.66	0.985	2.3	0.883	8.7×10^{-3}
	t_2	2.66		2.28		
	t_3	2.61		2.32		
Gr$_{P.tail}$	t	2.42	0.984	2.5	0.985	7.5×10^{-3}

Table 3.4: Hopping parameters used to fit the tight-binding Hamiltonian to the DFT calculated band structure. $t_\uparrow$ and $t_\downarrow$ are the spin up and spin down contributions. Gr$_{P.head}$ have directional dependent hoppings and its three values are listed. λ_R is the strength of the Rashba spin-orbit coupling obtained from fitting. All the values are given in eV.

we desire to calculate the conductances. In Fig. 3.10 we present calculated conductances at room temperature using a generalized version of Eq. 2.60 that includes the electric polarization degree of freedom.

$$G^{\sigma,\sigma'}_{\alpha,\alpha'} = \frac{e}{h}\sum_{\sigma}\int T^{\sigma,\sigma'}_{\alpha,\alpha'}\left(\frac{-\partial f}{\partial E}\right)dE, \tag{3.6}$$

where $T^{\sigma,\sigma'}_{\alpha,\alpha'}$ indicates spin-dependent transmission probability with (α,α') and (σ,σ') being, respectively, the relative polarization and magnetization configurations in the multiferroic regions, $f = \frac{1}{e^{(E-\mu)/k_BT}+1}$ is the Fermi-Dirac distribution in which μ and T indicate electrochemical potential and temperature, respectively. Note in Fig. 3.10(a) the different notations used to indicate the different magnetic states and electrical polarizations of the system. P$\alpha\beta$ indicates an electrical polarization α in the magnet M_1 and β in magnet M_2. Similarly, M$\alpha\beta$ indicates a magnetization α in the magnet M_1 and β in the magnet M_2. For all the systems considered it was used the same doping energy, in order to be able to compare the results obtained. Experimentally this can be achieved by gating the device.

In total, 16 combinations of electrical polarizations and magnetizations, but 8 of them

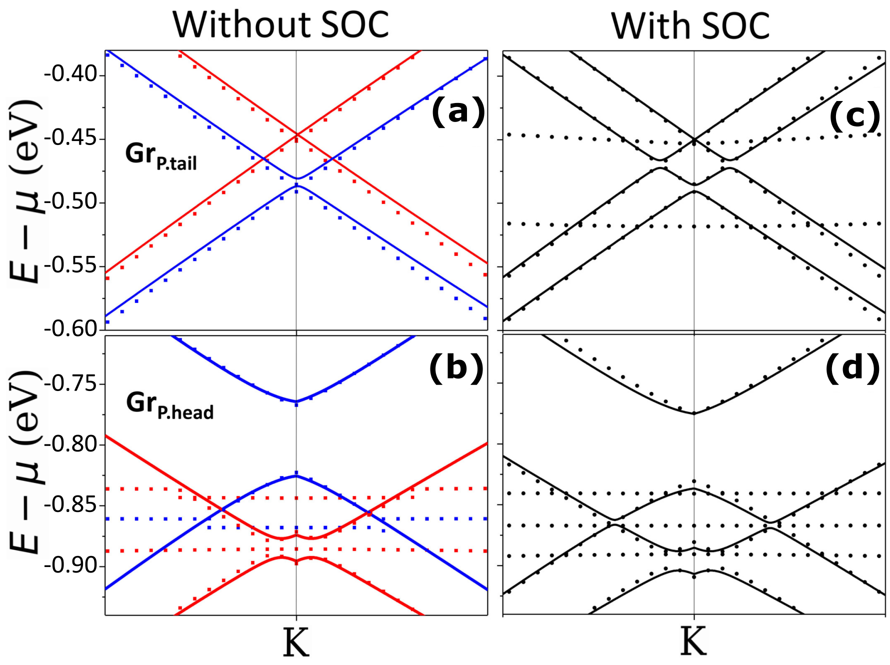

Figure 3.9: Fitted band structure for (a) Gr$_{P.tail}$ and (b) Gr$_{P.head}$ layers without spin-orbit. (c) and (d) are the bands calculated including spin-orbit coupling for Gr$_{P.tail}$ and Gr$_{P.head}$, respectively.

are complete equivalents. The different combinations give rise to three different types of proximity resistances: proximity electroresistance (PER), where the magnetizations are fixed and the electrical polarization are changed, proximity magnetoresistance (PMR), where the electrical polarization is fixed and the magnetizations are changed and proximity multiferroic resistance(PMER) in which the electrical polarization and magnetization remain the same in one of the magnets while in the other both quantities are changed simultaneously. These quantities can be defined mathematically as:

$$PER_{\alpha}^{\sigma,\sigma'} = \frac{G_{\alpha,\alpha}^{\sigma,\sigma'} - G_{\alpha,-\alpha}^{\sigma,\sigma'}}{G_{\alpha,\alpha}^{\sigma,\sigma'} + G_{\alpha,-\alpha}^{\sigma,\sigma'}} \tag{3.7}$$

$$PMR_{\alpha,\alpha'}^{\sigma} = \frac{G_{\alpha,\alpha'}^{\sigma,\sigma} - G_{\alpha,\alpha'}^{\sigma,-\sigma}}{G_{\alpha,\alpha'}^{\sigma,\sigma} + G_{\alpha,\alpha'}^{\sigma,-\sigma}} \tag{3.8}$$

$$PMER_{\alpha}^{\sigma} = \frac{G_{\alpha,\alpha}^{\sigma,\sigma} - G_{\alpha,-\alpha}^{\sigma,-\sigma}}{G_{\alpha,\alpha}^{\sigma,\sigma} + G_{\alpha,-\alpha}^{\sigma,-\sigma}}, \tag{3.9}$$

where $G_{\alpha,\alpha'}^{\sigma,\sigma'}$ indicates the conductance from the magnet M_1 with electrical polarization α and magnetization σ to M_2 with has electrical polarization α' and magnetization σ'. With this notation it is possible to create 16 states, of particular interest note that $G_{\alpha,\alpha'}^{\sigma,-\sigma} = G_{\alpha,\alpha'}^{-\sigma,\sigma}$ and $G_{\alpha,-\alpha}^{\sigma,\sigma'} = G_{-\alpha,\alpha}^{\sigma,\sigma'}$ and, consequently, we end up with six conductance states $G_{\alpha,\alpha'}^{\sigma,\sigma'}$.

Fig 3.10(b)-(d) show the calculated PER, PMR and PMER. The filled symbols cor-

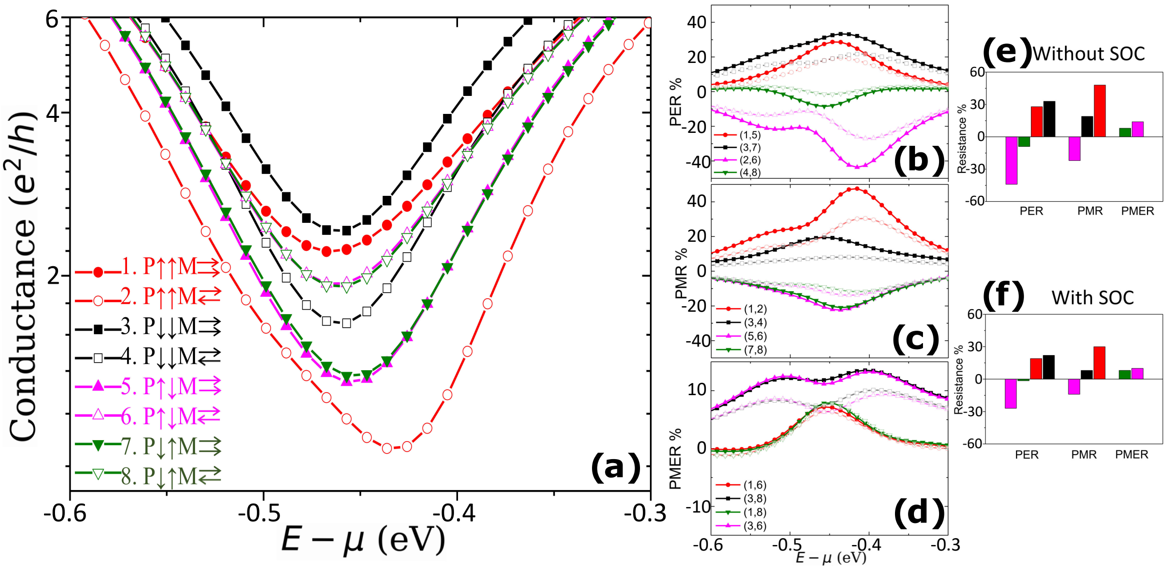

Figure 3.10: (a) Conductances for a system without SOC with two identical proximity induced multiferroic regions of length $L = 49.2$nm, width $W = 39.6$ nm separated a distance $d = 1.6$ nm. (b), (c) and (d) correspond to the calculated proximity electro (PER), magneto (PMR) and multiferroic (PMER) magnetoresistances. The filled symbols corresponds to a calculation without considering SOC and the open symbols corresponds to the system where SOC was included. The maximum values of the PER, PMR and PMER are presented for a system with SOC (e) and without SOC (f).

responds to a calculation without considering SOC and the open symbols corresponds to the system where SOC is included. As a consequence of the extra two degenerate conductance states, we obtain one (two) degenerate PMR (PMER) curves, correspondingly. We found that the PER values range from -44% to $+33\%$, PMR has values from -22% to $+48\%$, whereas PMER ranges between $+7\%$ and $+13\%$. As for the case of MIs we found that including SOC change the conductance values but its magnitude is not enough to change qualitatively the maximum values of the different proximity resistances as can be seen in Fig. 3.10(e) and (f).

Robustness of PMR, PER and PMER with respect to system dimensions

As expected the PMR behavior using multiferroics is very similar to what was found for MIs, being its main difference that when both electrical polarizations are parallel, the PMR is positive according to Fig. 3.11 (a1)-(b4), while when they are antiparallel, PMR values are negative as can be seen in Fig. 3.11 (c1)-(d4) independently of the value of the multiferroic length L, multiferroic width W or the separation between the multiferroic regions d. Four different ferroelectric polarization configurations where considered (a) (1,2) the up parallel configuration, (b) (3,4) the down parallel configuration, (c) (5,6) the up-down antiparallel configuration and (d) (7,8) the down-up antiparallel configuration, following the notation of Fig. 3.10. The dashed lines indicate the energy chosen to plot

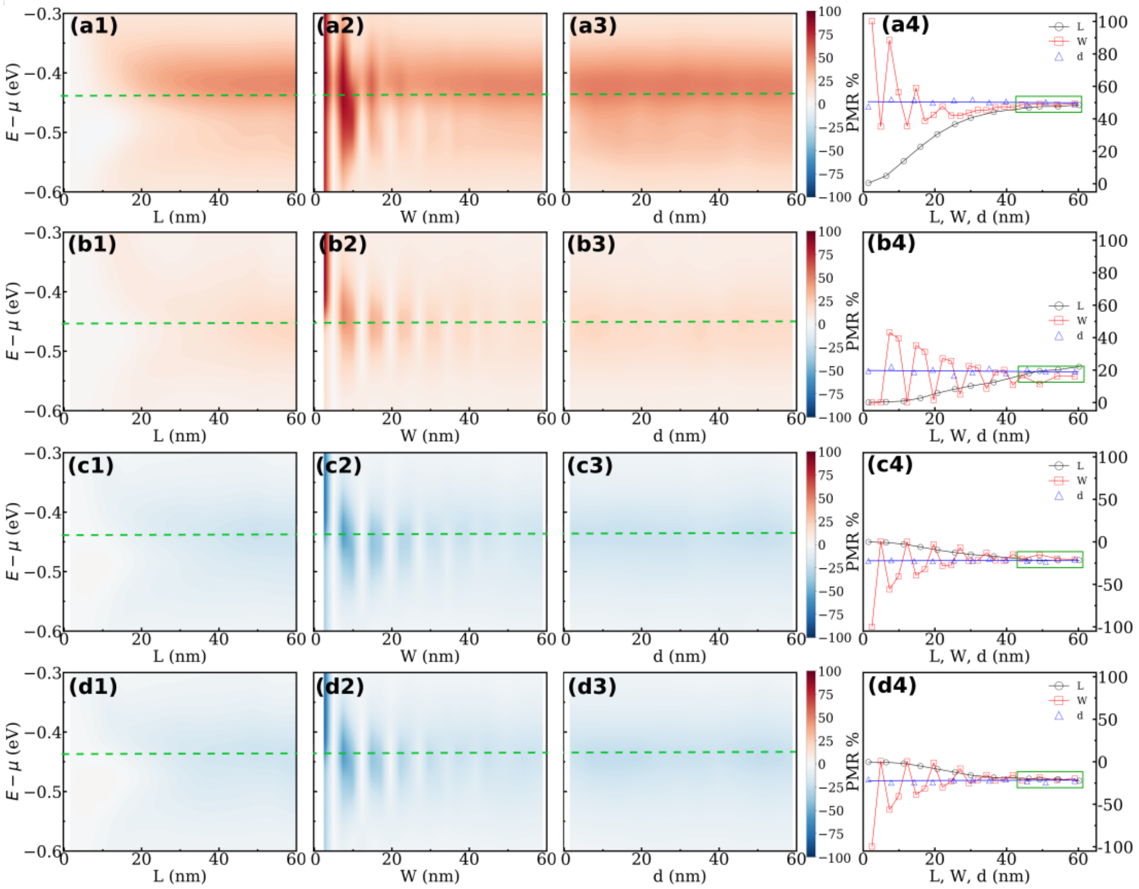

Figure 3.11: PMR profiles as a function of the multiferroic length L, its width W, and the separation among multiferroic regions d for a spintronic device with armchair edges for the system configurations of Fig. 3.10 (a1)-(a3) (1,2) (b1)-(b3) (3,4) (c1)-(c3) (5,6) and (d1)-(d3) (7,8). The dashed line shows the energy chosen to plot the dependence of PMR as a function of L (black circles), W (red squares), and d (blue triangles) in Figs. (a4), (b4), (c4), (d4). The green square highlights the region where PMR becomes independent of system dimensions.

PMR dependence with respect to the dimensions of the system shown in the rightmost panels, i.e. In Fig. 3.11(a4) $E = -0.453$, (b4) $E = -0.441$, (c4) $E = -0.416$ and (d4) $E = -0.465$ eV. For all the cases considered PMR increases as a function of the multiferroic length L increase until it saturates. PMR oscillates as a function of W for narrow systems and becomes constant for wide enough systems. These oscillations depend on edge termination type, and they are more pronounced for a system with armchair edges compared to zigzag or rough edges (not shown). The PMR exhibits an almost constant behavior as the separation between the multiferroic regions d increase. In order to have a size-independent PMR, it is necessary to develop systems of the order of those sizes enclosed in the green box of Figs. 3.11(a4), (b4), (c4), (d4) or bigger. With this we conclude that in multiferroics PMR is robust as well, with respect to the dimensions of the system.

Similar behavior are found for PER and PMER as a function of the dimensions of the

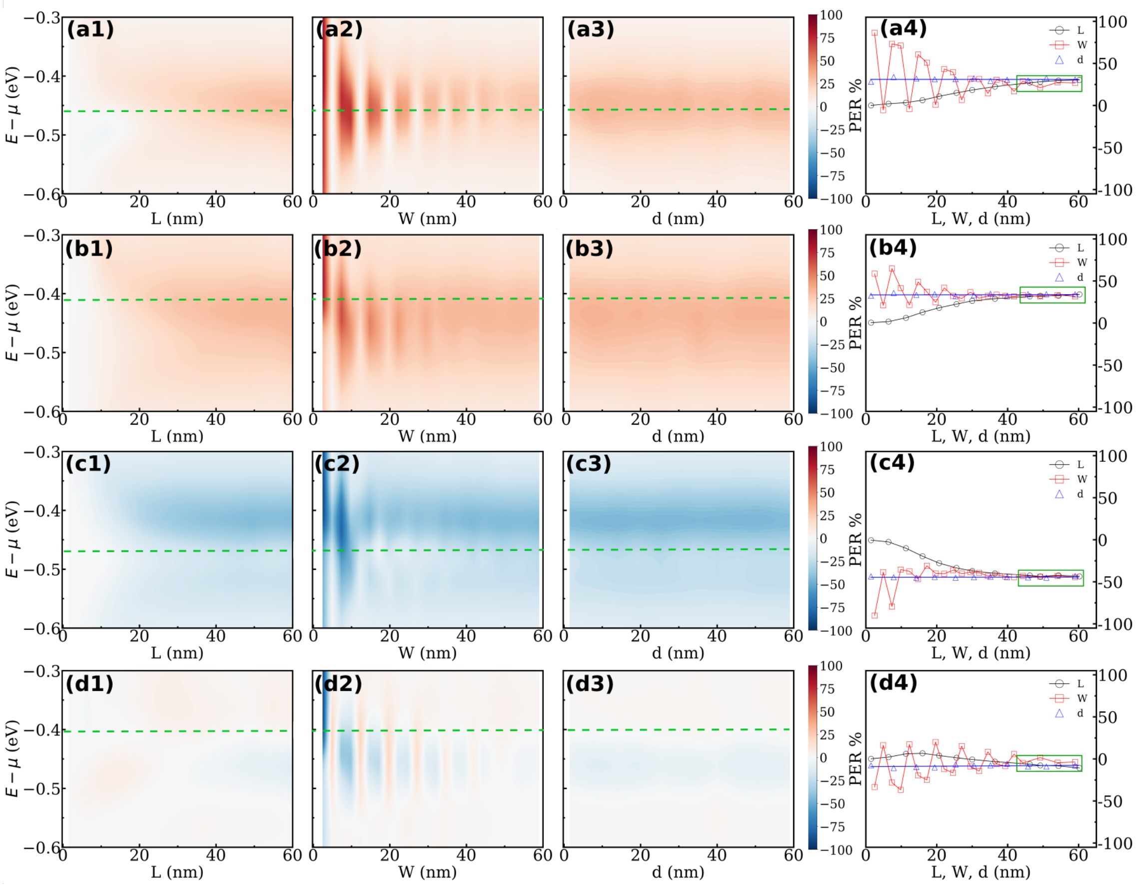

Figure 3.12: PER profiles as a function of the multiferroic length L, its width W, and the separation among multiferroic regions d for a spintronic device with armchair edges for the system configurations of Fig. 3.10 (a1)-(a3) (1,5) (b1)-(b3) (3,7) (c1)-(c3) (2,6) and (d1)-(d3) (4,8). The dashed line shows the energy chosen to plot the dependence of PER as a function of L (black circles), W (red squares), and d (blue triangles) in Figs. (a4), (b4), (c4), (d4). The green square highlights the region where PER becomes independent of system dimensions.

device as shown in Figs. 3.12 and 3.13. Similar to PMR, PER present positive values for parallel magnetizations as shown in Figs 3.12(a1)-(b4), while PER present negative values when the magnetizations are antiparallel, as shown in Fig. 3.12 (c1)-(d4). The energy values chosen to plot the rightmost panel highlighted by a dashed line for Fig. 3.12(a4) are $E = -0.459$, (b4) $E = -0.41$, (c4) $E = -0.465$, (d4) $E = -0.404$. Four different magnetic configurations were considered: (a) (1,5) the up parallel configuration, (b) (3,7) the down parallel configuration, (c) (2,6) the up-down antiparallel configuration and (d) (4,8) the down-up antiparallel configuration, following the notation of Fig. 3.10. In contrast to PMR and PER, the PMER shows always positive values for all configurations. The energy values chosen to plot the rightmost panel highlighted by a dashed line in Fig. 3.13 are for (a4) $E = -0.453$ eV, (b4) $E = -0.422$ eV, (c4) $E = -0.441$ eV, (d4) $E = -0.441$ eV. The four different configurations considered in Fig. 3.13 are (a) (1,6), (b) (3,8), (c) (1,8) and (d) (3,6), following the notation of Fig. 3.10. In order to avoid the dependence on the size of the system of PER and PMER, the device should have at least the dimensions of the order of the values enclosed by green square in Figs. 3.12 and 3.13. With this we can claim that PER and PMER as robust with respect to the dimension of the system as well.

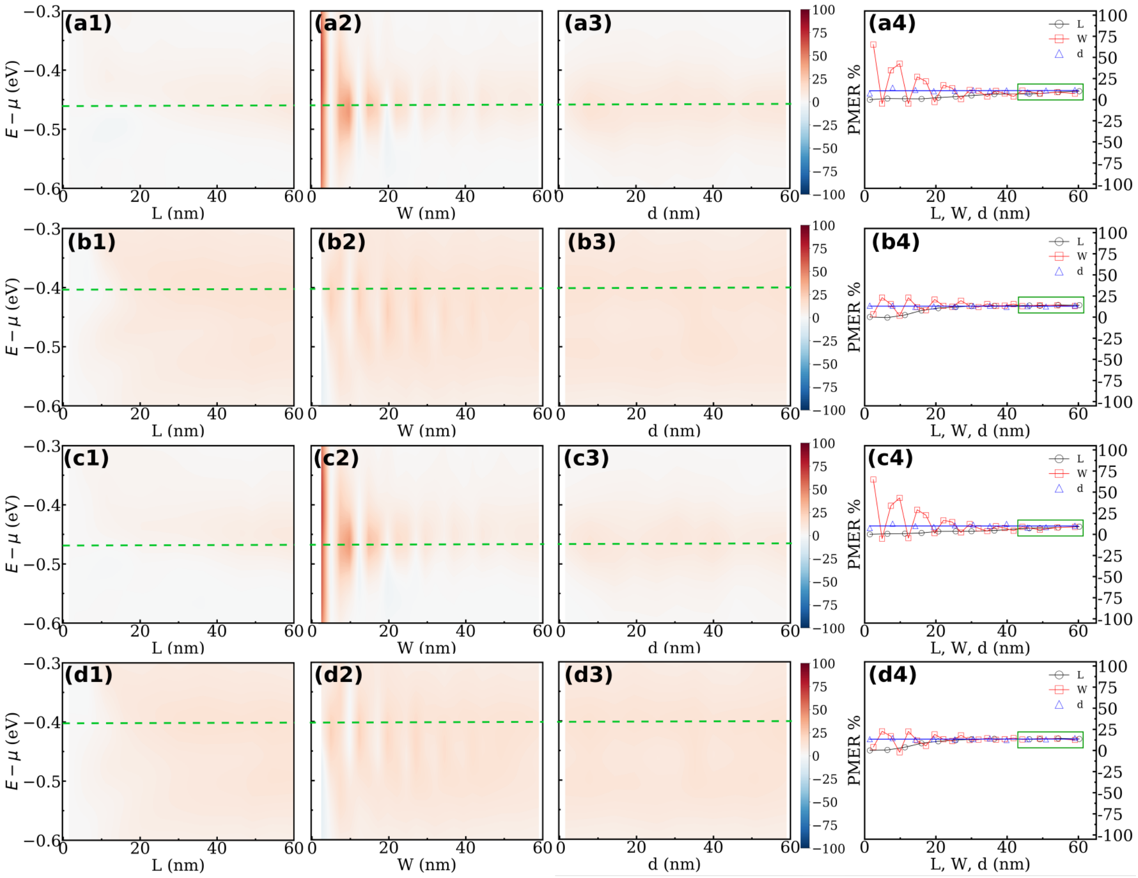

Figure 3.13: PMER profiles as a function of the multiferroic length L, its width W, and the separation among multiferroic regions d for a spintronic device with armchair edges for the system configurations of Fig. 3.10 (a1)-(a3) (1,6) (b1)-(b3) (3,8) (c1)-(c3) (1,8) and (d1)-(d3) (3,6). The dashed line shows the energy chosen to plot the dependence of PMER as a function of L (black circles), W (red squares), and d (blue triangles) in Figs. (a4), (b4), (c4), (d4). The green square highlights the region where PMER becomes independent of system dimensions.

3.4 Conclusion

We presented the proximity-induced phenomena in a graphene-based lateral system comprising regions with proximity-induced magnetism, by four different magnetic insulators: YIG, CFO, EuS and EuO, and later by the multiferroic BFO. For YIG- and CFO-based devices, we found proximity magnetoresistance (PMR) ratios of 77% and 22% at room temperature, respectively. For EuS and EuO based systems, we found PMR values of 100% for both at 16 and 70 K, respectively. Very importantly, we demonstrated that the PMR is robust with respect to system dimensions being limited by the graphene spin diffusion length. Due to its potential for application, the robustness of the PMR with respect to edge-type termination and SOC was analyzed for YIG-based systems, finding it decreasing only by about half even for considerably large SOC strength values.

In the presence of a multiferroic material a new degree of freedom is added to the spin valve: the electrical polarization. We demonstrated that the device is tunable via ferroelectric and magnetic control and studied two quantities, besides PMR, that appear as a consequence of addition of ferroelectric polarization: proximity electroresistance (PER) and proximity multiferroic resistance (PMER). We found values for PMR from -22% to +48%, for PER from -44% to +33% and for PMER from +7% to +13%. In addition, we showed that the SOC does not affect greatly the values of these quantities. PMR, PER and PMER in BFO-based system are robust with respect to system dimensions and present a similar dependence as PMR in MI based ones.

CHAPTER 4

Non-collinear transport calculations

4.1 Physics of spin transfer torque

Until now, we have considered collinear magnetic configurations. The non-collinear orientation of the magnetizations in a spin valve can lead to the appearance of a phenomenon known as spin transfer torque (STT). This effect allows the control and manipulation of magnetic moments and domain walls of a magnetic material by using an electrical current and is essential in different device applications.

The STT can be considered as the inverse effect of GMR, where the magnetic state of the ferromagnet affects the electrical resistance of the system [19]. The first insights on the STT phenomenon appeared from studies on domain walls and magnetic tunnel junctions in the 70's and 80's but the consolidation of the STT concept was only achieved in 1996, when independently, Slonczewski [111] and Berger [112] predicted the spin angular momentum transfer from a spin polarized current to a ferromagnet. The STT was demonstrated experimentally for the first time in cobalt/copper multilayers by Tsoi and coworkers [113]. They found that the resistance variation of the multilayers induced by electrical current was due to magnetic excitations. Other works include studies done on Co/Cu/Co pillars, where it was found that thanks to the STT induced in the pillar under the presence of a magnetic field, switching of one of the magnetic layers is possible as reported in Refs. [114, 115]. Thereafter, STT has been found in other systems, that include metallic spin valves, MTJ's, antiferromagnets, semiconductor devices, among others.

A typical spin valve setup is composed by two ferromagnetic layers separated by a non-magnetic material that can be either an insulator or a metal. In order to fix the magnetization of one of the layers, the layer is grown thicker and/or its magnetization is pinned by exchange bias with an antiferromagnet. This magnetic layer is known in the literature as fixed layer. The other magnetic layer is free to change its magnetization and is known as free layer. These kind of systems have been studied extensively to explain their behavior. Semiclassical approaches include generalizations of the Valet-Fert theory [116] to non-collinear cases as presented in Ref. [117, 118] or a generalization of the Kirchoff's laws as in Refs. [119, 120]. Broader theories to include quantum coherent effects, very important in the ballistic transport regime, have used non equilibrium Green functions like in Refs. [74, 90, 121, 122] and the random scattering matrix theory as reported in Ref. [123].

In order to understand the STT mechanism, let us consider the graphene lateral spin valve shown in Fig. 4.1(a) with the magnetization of M_1 fixed along the z-axis, while the angle θ, that corresponds to the magnetic orientation of M_2, can be rotated between 0 and π. If the current flows in the y direction from L_1 the system charge and longitudinal spin currents in ballistic regime are conserved, while transverse spin current components induce torque on both magnetic layers as depicted in Fig. 4.1(b). Depending on the magnitude of the transferred STT to the magnetic layers, this can change the magnetic orientation of both magnets, but because the magnetization of M_1 is fixed, only M_2 is affected. The switching of the magnetization depends on the intrinsic damping parameter of the system as well as the polarity of the current applied, as was explained in Chapter 2, Sec. 2.6.

What is the physical origin of this torque? Let us look again at the system depicted in Fig. 4.1(a). When the current enters the first magnetic layer (M_1), the flow of electrons will acquire the spin polarization of the ferromagnet. When it reaches the central region it does not change its magnetization, but when it gets to the free layer (M_2), the spins of the electrons interact with the spins of the electrons in this ferromagnet, changing again the polarization of the current. Because the angular momentum should be conserved, the lost component of spin is transferred to the magnets in the form of torque [124].

The first experimental demonstration of STT in a graphene-based systems, was found in a lateral nonlocal spin valve composed of permalloy contacts on top of a graphene sheet as reported in Ref. [125]. For this system, in order to switch the magnetization orientation between parallel and antiparallel configurations, besides the electrical current, it was necessary to apply a suitable in-plane external field. In fact, the switching depends on the magnitude of both quantities.

In this chapter we study the STT phenomena generated in a graphene-based valve using the ferromagnet insulator YIG as a magnet and analyze the robustness of this quantity with respect to the dimension of the system at room temperature. In addition, we investigate the possibility to switch the magnetization's orientation by proximity effects and estimate the current necessary to achieve this.

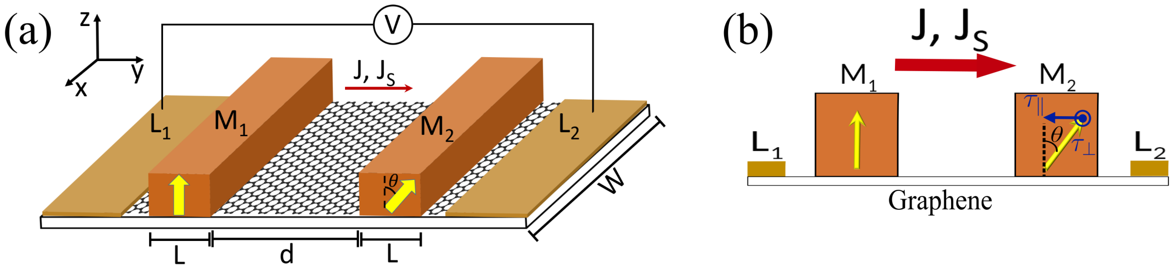

Figure 4.1: (a) Graphene lateral spin valve composed of two magnetic regions M_1 and M_2 with non-collinear magnetizations. The magnetization of M_1 points along the z-direction, while that one of M_2 makes an angle θ with respect to the z-axis. The magnets have width W, length L and are separated a distance d. The spin valve is then connected to two leads L_1 and L_2. (b) Schematic representation of the torque direction with respect to the magnetization of the magnets when a current flows in the graphene sheet. For simplicity, the uncompensated spin angular momentum transferred as torque is only sketched on M_2. The field-like torque $\tau_{||}$ is perpendicular to the magnetization and the out of plane component $\tau_{\perp}$ is perpendicular to both.

4.2 Graphene with spin dependent hoppings and spin dependent sublattice potential

Graphene has two sublattices A and B, that in our proximity induced system, behave differently due to the presence of a magnetic insulator. To calculate the STT in graphene it is necessary to take into account this degree of freedom. The objective of this section is to find the spin current conservation equation for graphene in the presence of the neighboring magnetic material.

In Eq. (2.23) we defined the sublattice potential due to the presence of a magnetic insulator as:

$$V_A = \left(E_D + \frac{\Delta_s}{2}\right)\mathbb{1} + \left(\frac{\delta + \Delta_\delta}{2}\right)(\boldsymbol{\sigma}\cdot\boldsymbol{m})$$
$$V_B = \left(E_D - \frac{\Delta_s}{2}\right)\mathbb{1} + \left(\frac{\delta - \Delta_\delta}{2}\right)(\boldsymbol{\sigma}\cdot\boldsymbol{m}),$$

where the first term of the right represents a regular onsite potential. The second one is a spin dependent term responsible for the changes required for STT equation obtained in Eq. (2.96). Let us ignore for the moment the onsite potential and define:

$$J_A = \frac{\delta + \Delta_\delta}{2} \tag{4.1}$$
$$J_B = \frac{\delta - \Delta_\delta}{2}, \tag{4.2}$$

so we can rewrite our Hamiltonian as:

$$H = H_1 + H_2 + H_3$$

with,

$$\begin{aligned} H_1 &= J_A \sum_{i\alpha\beta} c^{A\dagger}_{i\alpha} (\boldsymbol{\sigma} \cdot \boldsymbol{m}_i)_{\alpha\beta} c^A_{i\beta} + J_B \sum_{i\alpha\beta} c^{B\dagger}_{i\alpha} (\boldsymbol{\sigma} \cdot \boldsymbol{m}_i)_{\alpha\beta} c^B_{i\beta} \\ H_2 &= t \sum_{\langle ij \rangle \alpha} c^{A\dagger}_{i\alpha} c^B_{j\alpha} + c.c. \\ H_3 &= t' \sum_{\langle ij \rangle \alpha\beta} c^{A\dagger}_{i\alpha} (\boldsymbol{\sigma} \cdot \boldsymbol{m}_i)_{\alpha\beta} c^B_{j\beta} + c.c. \end{aligned} \tag{4.3}$$

Note that H_2 and H_3 are not affected by the presence of the spin dependent sublattice potential, so Eqs. (2.87) and (2.93) remain unchanged

$$[S_{i'}, H_2] = \frac{1}{i}(j^{\boldsymbol{\sigma}}_{i'} - j^{\boldsymbol{\sigma}}_{i'-1}) \tag{4.4}$$

$$[S_{i'}, H_3] = \frac{1}{i}(j^{s_\lambda}_{i'} - j^{s_\lambda}_{i'-1}) + 2it' \sum_i (\boldsymbol{m}_{i'} \times \boldsymbol{S}_{ii'}) \tag{4.5}$$

For H_1, we have to calculate the following commutator:

$$[S_{i'}, H_1] = \left[S_{i'}, \left(J_A \sum_{i\alpha\beta} c^{A\dagger}_{i\alpha} (\boldsymbol{\sigma} \cdot \boldsymbol{m}_i)_{\alpha\beta} c^A_{i\beta} + J_B \sum_{i\alpha\beta} c^{B\dagger}_{i\alpha} (\boldsymbol{\sigma} \cdot \boldsymbol{m}_i)_{\alpha\beta} c^B_{i\beta} \right) \right] \tag{4.6}$$

$$= \left[S_{i'}, J_A \sum_{i\alpha\beta} c^{A\dagger}_{i\alpha} (\boldsymbol{\sigma} \cdot \boldsymbol{m}_i)_{\alpha\beta} c^A_{i\beta} \right] + \left[S_{i'}, J_B \sum_{i\alpha\beta} c^{B\dagger}_{i\alpha} (\boldsymbol{\sigma} \cdot \boldsymbol{m}_i)_{\alpha\beta} c^B_{i\beta} \right]. \tag{4.7}$$

Note that

$$S_{i'} = \sum_{\alpha'\beta'} c^{A\dagger}_{i'\alpha'} \sigma_{\alpha'\beta'} c^A_{i'\beta'} + c^{B\dagger}_{i'\alpha'} \sigma_{\alpha'\beta'} c^B_{i'\beta'}. \tag{4.8}$$

Solving the first term of Eq. (4.7) and considering the spin density in the x direction with the same identity as in Eq. (2.78)

$$\begin{aligned} J_A \sum_{i\alpha'\beta'\alpha\beta} & c^{A\dagger}_{i\alpha} \sigma^x_{\alpha'\beta'} [c^A_{i'\alpha'}, c^{A\dagger}_{i\alpha} (\boldsymbol{\sigma} \cdot \boldsymbol{m}_i)_{\alpha\beta}] c^A_{i\beta} + [c^{A\dagger}_{i\alpha'} \sigma^x_{\alpha'\beta'}, c^{A\dagger}_{i\alpha} (\boldsymbol{\sigma} \cdot \boldsymbol{m}_i)_{\alpha\beta}] c^A_{i'\beta'} c^A_{i\beta} \\ & + c^{A\dagger}_{i\alpha} (\boldsymbol{\sigma} \cdot \boldsymbol{m}_i)_{\alpha\beta} c^{A\dagger}_{i\alpha'} \sigma^x_{\alpha'\beta'} [c^A_{i'\beta'}, c^A_{i\beta}] + c^{A\dagger}_{i\alpha} (\boldsymbol{\sigma} \cdot \boldsymbol{m}_i)_{\alpha\beta} [c^{A\dagger}_{i\alpha'} \sigma^x_{\alpha'\beta'}, c^A_{i\beta}] c^A_{i'\beta'}. \end{aligned} \tag{4.9}$$

Using the fermionic relations of Eq. (2.79) and after some algebra we get:

$$J_A \sum_{\alpha'\alpha\beta} c^{A\dagger}_{i'\alpha'} \sigma^x_{\alpha'\alpha} (\boldsymbol{\sigma} \cdot \boldsymbol{m}_{i'})_{\alpha\beta} c^A_{i'\beta} - c^{A\dagger}_{i'\alpha'} (\boldsymbol{\sigma} \cdot \boldsymbol{m}_{i'})_{\alpha'\alpha} \sigma^x_{\alpha\beta} c^A_{i'\beta}. \tag{4.10}$$

Note the similarities with Eq. (2.83) and following a similar procedure we find

$$\left[S_{i'}, J_A \sum_{i\alpha\beta} c_{i\alpha}^{A\dagger}(\boldsymbol{\sigma}\cdot\boldsymbol{m}_i)_{\alpha\beta}c_{i\beta}^{A}\right] = 2iJ_A(\boldsymbol{m}_{i'}\times\boldsymbol{S}_{i'}^{A}), \tag{4.11}$$

and

$$\left[S_{i'}, J_B \sum_{i\alpha\beta} c_{i\alpha}^{B\dagger}(\boldsymbol{\sigma}\cdot\boldsymbol{m}_i)_{\alpha\beta}c_{i\beta}^{B}\right] = 2iJ_B(\boldsymbol{m}_{i'}\times\boldsymbol{S}_{i'}^{B}). \tag{4.12}$$

Finally, gathering all the terms obtained for H_1, H_2 and H_3, we can write the steady state spin conservation equation as:

$$\sum_{i'}(j_{i'}^{\boldsymbol{\sigma}} - j_{i'-1}^{\boldsymbol{\sigma}}) = 2J_A\sum_{i'}(\boldsymbol{m}_{i'}\times\boldsymbol{S}_{i'}^{A}) + 2J_B\sum_{i'}(\boldsymbol{m}_{i'}\times\boldsymbol{S}_{i'}^{B}) + 2t'\sum_{i,i'}(\boldsymbol{m}_{i'}\times\boldsymbol{S}_{ii'}). \tag{4.13}$$

4.3 Spin transfer torque calculation using Kwant

The STT $\boldsymbol{\tau}$ can be obtained using any side of Eq. (4.13). For example the torque τ_x can be obtained as:

$$\tau_x = \sum_{i'}(j_{i'}^{\sigma^x} - j_{i'-1}^{\sigma^x}) \tag{4.14}$$

$$\tau_x = 2J_A\sum_{i'}(\boldsymbol{m}_{i'}\times\boldsymbol{S}_{i'}^{A})\cdot\hat{e}_x + 2J_B\sum_{i'}(\boldsymbol{m}_{i'}\times\boldsymbol{S}_{i'}^{B})\cdot\hat{e}_x + 2t'\sum_{i,i'}(\boldsymbol{m}_{i'}\times\boldsymbol{S}_{ii'})\cdot\hat{e}_x. \tag{4.15}$$

Using Eq. (4.14) in Kwant the spin current can be obtained using the function kwant.operator.Current. Let us consider the lateral spin valve from Fig. 4.1(a). To calculate the torque in M_1, it is necessary to get the contribution from each atomic row and sum them up. The torque in one atomic row is the subtraction of the spin current per voltage that enters a ferromagnetic region, measured at any point in the left side graphene region with respect to M_1 and that one that comes out, measured at any point in the right side graphene region. It does not matter which point is chosen inside of any of the pure graphene regions because the spin current values are the same due to their conservation. Later, the STT contribution from each atomic row in the magnetic region is summed-up and with this we obtain the total STT in M_1. The procedure for the magnet M_2 is exactly the same, but one step is added. Due to the angle between M_2 and the z-axis, the STT value obtained for M_2 should be adjusted with respect to the coordinate system fixed in M_1 using the rotation matrix in spherical coordinates as:

$$R(\theta) = \begin{pmatrix} \cos(\theta) & 0 & -\sin(\theta) \\ 0 & 1 & 0 \\ \sin(\theta) & 0 & \cos(\theta), \end{pmatrix} \tag{4.16}$$

with θ being the angle between the magnetization in M_2 with the z axis. In principle the rotation matrix can have as well the coordinate ϕ, but because we do not consider SOC, that would break the symmetry in ϕ, for simplicity we define $\phi = 0$.

To calculate the STT using Eq. (4.15), several terms should be calculated. All of them include the calculation of the spin density response that in Kwant is obtained using the function kwant.operator.Density. Its first term only takes into account sites from the A sublattice, while in the second term only B sublattice sites are considered. The spin density response is calculated for each site of the sublattice required inside one ferromagnet, let say M_1 and then summed-up to get the total STT. To obtain the third term, the spin density response has to be calculated for neighboring sites inside the ferromagnet without distinction of the sublattice type. Once all terms are calculated the last step is to sum them all the get the STT in the magnet M_1. The STT in M_2 can be calculated applying a similar procedure but it should be adjusted using the rotation matrix from Eq. (4.16).

Let us now test if Eqs. (4.14) and (4.15) give us the same results. First of all, it is important to find the expression for the new spin dependent hoppings, so we can include the effect of the magnetic angle. This new hopping term can be expressed as:

$$t_p = \left(\frac{t_\uparrow + t_\downarrow}{2} \right) \mathbb{1} + \left(\frac{t_\uparrow - t_\downarrow}{2} \right) (\sigma^x m_p^x + \sigma^y m_p^y + \sigma^z m_p^z), \tag{4.17}$$

where the subindex p indicates the magnet under consideration. Fig. 4.2 shows the comparison of the different torque components using both Eqs. (4.14) and (4.15). It can be seen that both curves coincide as expected. This calculation was done for the spin valve from Fig. 4.1 with $L = 49.2$ nm, $W = 39.4$ nm and $d = 1.5$ nm at the energy $E = -0.81$ eV, using magnets made of YIG. Let us define the auxiliary parameter t' as:

$$t' = \frac{t_\uparrow - t_\downarrow}{2} \tag{4.18}$$

The corresponding values of the parameters J_A and J_B from Eqs. (4.1) and (4.2), respectively and t' from Eq. (4.18) for YIG are presented in Table 4.1. The magnitude of the exchange J_B is more than twice the value of that one of J_A, what reflects the effect of the different spin sublattice potential on the torque.

The component along the x axis is known as in-plane or dumping-like torque and is

Table 4.1: parameters J_A, J_B, t' obtained for YIG using Eqs. (4.1), (4.2) and (4.18)

Structure	J_A (eV)	J_B (eV)	t' (eV)
Gr/YIG	-0.026	-0.0575	-0.01

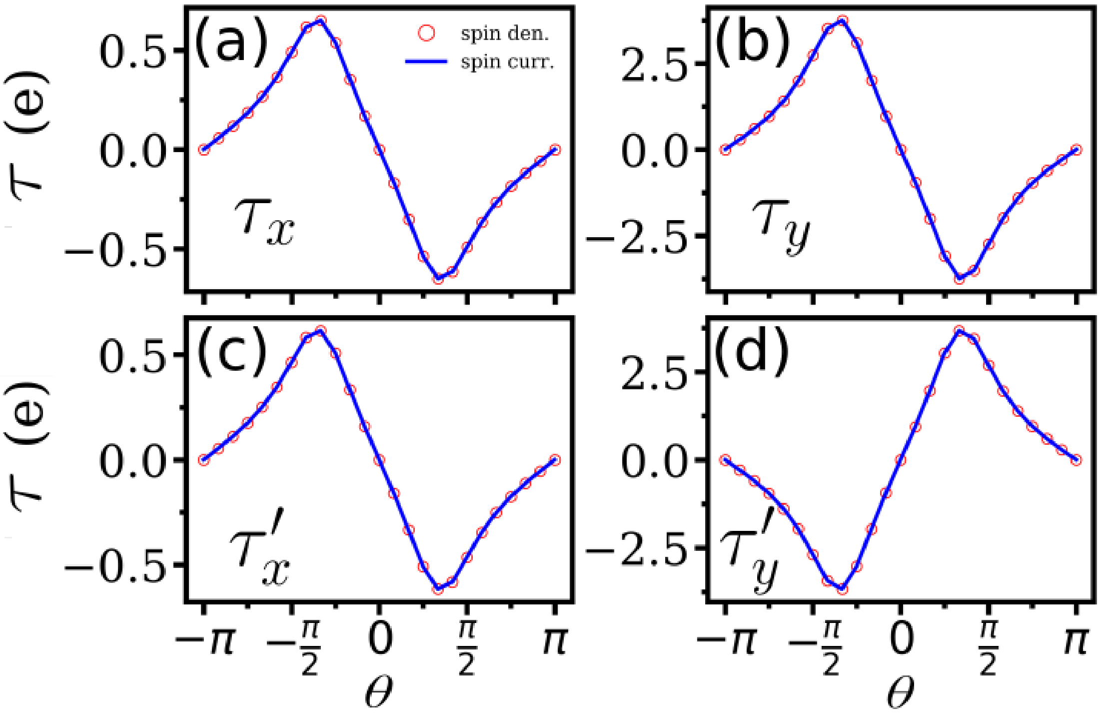

Figure 4.2: STT calculated using Eqs. (4.14) and (4.15) for a system with $L = 49.2$ nm, $W = 39.4$ nm and $d = 1.5$ nm at energy $E = -0.81$ eV. The top figures correspond to the STT in the magnet M_1 as a function of the magnetization angle θ for each non-zero torque component (a) τ_x, (b) τ_y. (c) and (d) show the STT dependence with respect to θ but in the magnet M_2. Note that the STT values in (c) and (d) have been adjusted to the local coordinate system in M_1, so $\tau_x = \tau'_x$ and $\tau_y = -\tau'_y$ as expected [126].

parallel to the plane formed by the magnetizations of M_1 and M_2

$$\boldsymbol{\tau}_{\parallel} \propto \boldsymbol{M_2} \times (\boldsymbol{M_2} \times \boldsymbol{M_1}). \tag{4.19}$$

The component along the y axis is known as out of plane component or field-like torque and is perpendicular to the plane formed by the magnetization of M_1 and M_2

$$\boldsymbol{\tau}_{\perp} \propto \boldsymbol{M_1} \times \boldsymbol{M_2}. \tag{4.20}$$

The proportionality constants depend on the voltage applied to the system, as well as, the properties of the system. For instance, if the system is half-metallic the in-plane torque is linear with the voltage, while the out of plane is purely quadratic in the voltage when both magnets are symmetric. For a wider discussion, please see Ref. [74].

4.4 Spin transfer torque in proximity induced graphene-based spin valve

The purpose of this section is to study the behavior of STT within lateral device shown in Fig. 4.1(a), with proximity induced magnetism based on YIG. We will focus on the dependence of the STT with respect the size of the system on angle between magnetizations and system size dimensions for different energies with respect to splitted graphene bands. For convenience we will start from angular dependence of transmission.

4.4.1 Transmission analysis

To start our analysis, let us look first at a quantity we already understand, the transmission. Fig. 4.3 shows the band structure (a) and corresponding transmission for each spin channel in the collinear magnetic configuration (b) along with the number of channels N_{ch} per spin (c) and that in a pure graphene sheet (d). We consider several energy regions. The green regions (top and bottom) indicates those with contribution from both spin channels, the pink region indicates the region where there is only contribution of the spin minority and while the blank one shows only spin majority contributions according to panel (a). One can note that the higher conductance present for a and d energies from Fig. 4.4 (b) can be understood as a consequence of where the higher number of channels is available that can transmit with respect to the b and c.

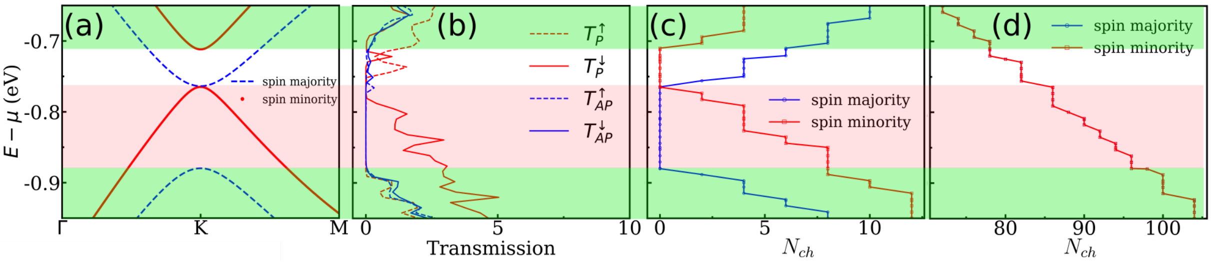

Figure 4.3: (a) YIG band structure, (b) Transmission per spin channel for the collinear case, considering the parallel and antiparallel configuration for the system of Fig.4.1 with L = 49.2 nm, W = 39.4 nm and d = 1.5 nm. (c) and (d) shows the energy as a function of the number of channels N_{ch} for the magnetic system and a pure graphene lead respectively. The green shaded regions correspond to zones where there are contributions from both spin channels according to the band structure in (a). The pink shaded region shows a half-metallic zone where there is only contribution of the minority spin, while the blank region highlights a half-metallic region where there is only contribution from the majority spin.

Let us now calculate the conductance as a function of the angle θ. To get it we need to use Eq. (2.42) and including angular dependence of the hoppings given by Eq. (4.17). Fig. 4.4(a) shows the YIG band structure with four dashed lines crossing aforementioned energy regions in Fig. 4.3 and indicated by italic letters from a to d. For each energy chosen the corresponding conductance as a function of θ at $T = 0$ K is plotted in Fig. 4.4(b). For energies b and c that corresponds to $E = -0.725$ eV and $E = -0.81$ eV, respectively the conductance is smaller, as expected, compared to a and d corresponding to $E = -0.675$ eV and $E = -0.9$ eV respectively. This can be explained by difference in number of available channels for transport (cf. Fig. 4.3). We note, however, another difference in behavior of conductance angular behavior at energies corresponding to half-metallic blank and pink regions vs those regions with both channels open. Namely, it is the absence of expected conductance maximum at $\theta = 0$ according to section 1.2.2 from Chapter 1. So the next step is to understand this unusual behavior of the conductance in these energy regions.

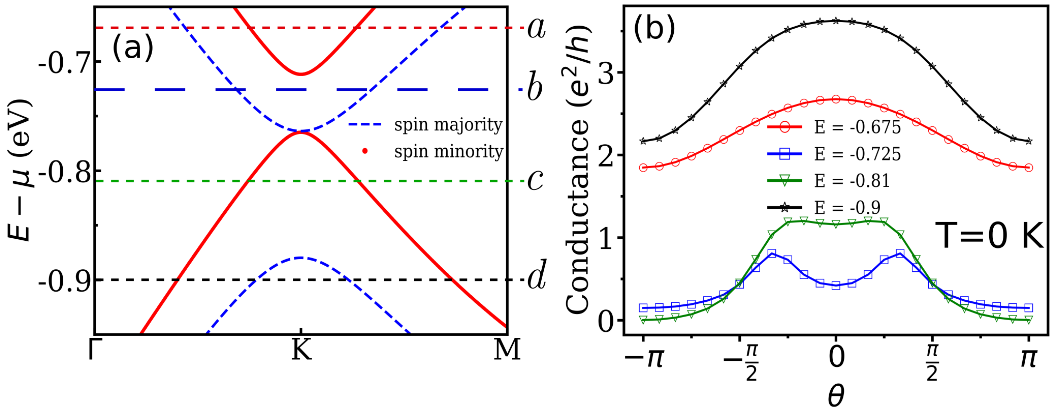

Figure 4.4: (a) YIG band structure where it has been highlighted with dashed lines four energies that corresponds to the different energy zones defined in Fig. 4.3. The energy chosen in a is $E = -0.675$ eV, in b is $E = -0.725$ eV, in is c $E = -0.81$ eV and in d is $E = -0.9$ eV. (b) Conductance as a function of the angle θ at $T = 0$ K, for the 4 different energies highlighted in with dashed lines in (a). Each color correspond to a different energy.

Let us go back to the analysis of the transmissions, and take advantage from the fact that we can obtain the transmission per spin species. Due to the non-collinearity of the system, it is necessary to include in the transmission per spin channel additional terms, defining:

$$T_{\uparrow\uparrow} = |t_{\uparrow\uparrow}|^2, \qquad T_{\downarrow\downarrow} = |t_{\downarrow\downarrow}|^2, \qquad T_{\downarrow\uparrow} = |t_{\downarrow\uparrow}|^2, \qquad T_{\uparrow\downarrow} = |t_{\uparrow\downarrow}|^2, \tag{4.21}$$

where $t_{\sigma\sigma'}$, with $\sigma, \sigma' =\uparrow (\downarrow)$, are the transmission amplitudes from Eq. (2.59) the transmissions per spin channel are:

$$T^{\uparrow} = T_{\uparrow\uparrow} + T_{\uparrow\downarrow} \qquad \text{and} \qquad T^{\downarrow} = T_{\downarrow\downarrow} + T_{\downarrow\uparrow}, \tag{4.22}$$

so the total transmission can be written as:

$$T^{tot} = T^{\uparrow} + T^{\downarrow}. \tag{4.23}$$

With the aim to understand what happens in the half-metallic regions in Fig. 4.5 we plot each spin contribution that comes into play as a function of angle θ, $T_{\uparrow\uparrow}$, $T_{\downarrow\downarrow}$, $T_{\downarrow\uparrow}$ and $T_{\uparrow\downarrow}$, given by Eq. 4.21, for four different energies, (a) $E = -0.675$ eV, (b) $E = -0.725$ eV, (c) $E = -0.81$ eV and (d) $E = -0.9$ eV. We know that experimentally it is not possible to separate each term in Eqs. (4.22) but we do it for analysis purpose. Fig. 4.5(a) and (d) correspond to the case with both spin channel contribution and as expected the dominant spin contribution for the former ones are $T_{\uparrow\uparrow}$ and $T_{\downarrow\downarrow}$. In half-metallic case, with no contribution from the spin up channel and the only non-zero contribution are $T_{\downarrow\downarrow}$ and $T_{\uparrow\downarrow}$ (Fig. 4.5(c)). The shape of these two curves perfectly explain the behavior of the corresponding conductance in Fig. 4.4(b). Fig. 4.5(b) displays unexpected non half-metallic behavior because in the energy region it is located (blank region in Fig. 4.3) there should be no transmission to the spin down channel according to the band structure in Fig. 4.3(a). Nevertheless, there are still some contributions from this channel that might be due to tunneling to evanescent states minority states due to its much smaller band gap as seen in Fig. 4.3. The shape of conductance in Fig. 4.5(b) can then be easily understood if one looks at the energy chosen. The spin majority electrons transport tunnel is affected by the tunneling effect, evidenced in the huge value of $T_{\uparrow\downarrow}$ and the non-zero transmission of $T_{\uparrow\uparrow}$ at $\theta = \pi$ (antiparallel magnetic configuration), contrary to what happens in (c) with $T_{\downarrow\downarrow}$. The tunneling probability through a minority band gap is not vanishing here as this gap is smaller compared to that in Fig. 4.5(c), with majority band gap twice larger compared to the minority one case of Fig. 4.5(b). The existence of four different energy regions will serve understanding of the torque behavior in this section.

4.4.2 Numerical results

For lateral spin valve proximity device shown in Fig. 4.1 we calculated the STT by using Eq. (4.14) at $T = 0$ K. Fig. 4.6 shows the torque response transferred to M_2 as a function of the angle θ for four characteristic energies for chosen energies in the YIG band structure presented again in Fig. 4.6(a) for convenience. In Fig. 4.6(b) and (c) we present the STT in-plane and out of plane components, respectively. One can see that the in-plane component has an usual sinus-like behavior and that the out of plane component shows more complicated behavior. While the curves corresponding to a and d display a normal angular dependence as well, the other two curves present higher torque values and behave differently from the rest. They correspond to the energies $E = -0.725$ eV and $E = -0.81$ eV (b and c cases in Fig. 4.6(a)). As we have already noted in previous section, this case is a particular one lying in a region where the system is a half-metal

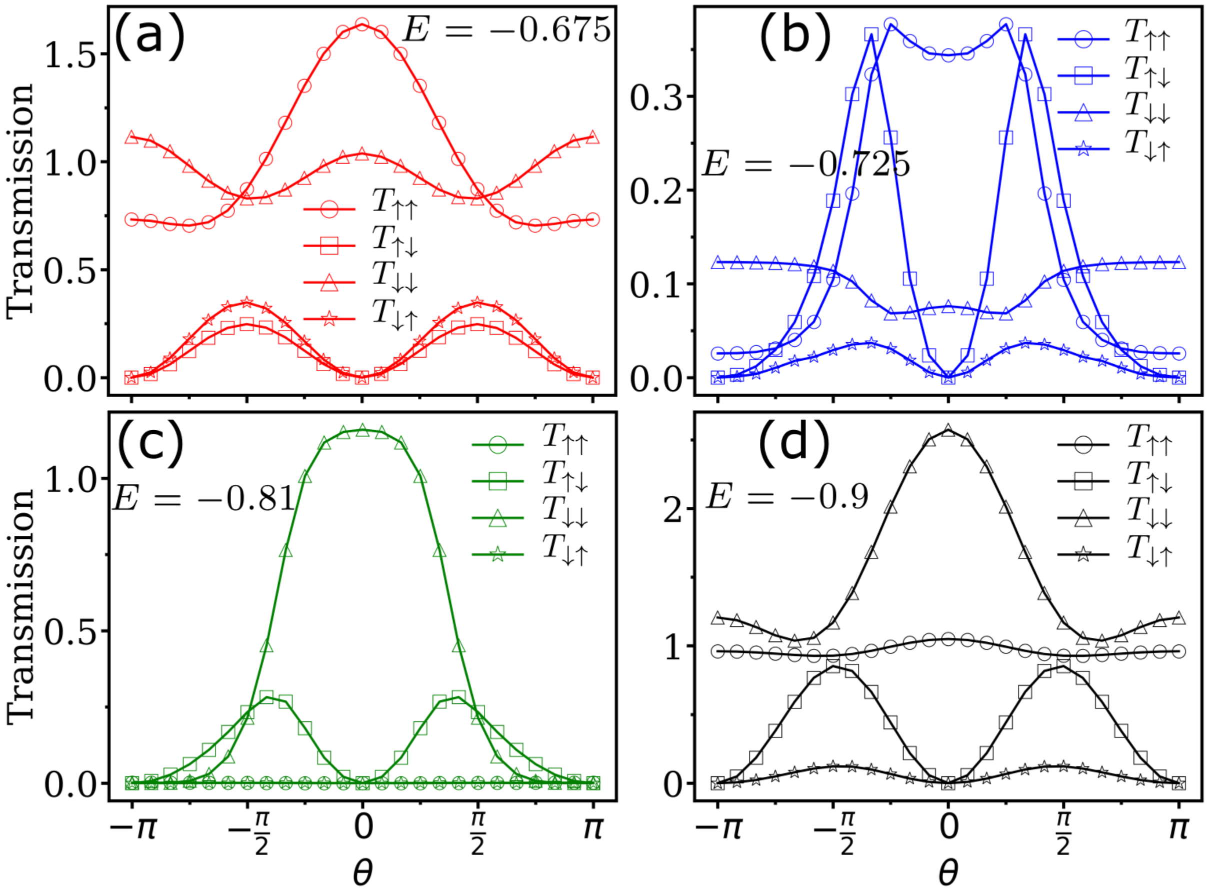

Figure 4.5: Transmission contributions defined by Eqs. (4.21) as a function of the angle θ for (a) $E = -0.675$ eV, (b) $E = -0.725$ eV, (c) $E = -0.81$ eV, (d) $E = -0.9$ eV.

allowing the quantum tunneling of the other spin species, that could provide a hint for the unusual oscillations it displays as a function of θ, while the c energy is in an energy region where the system is purely half-metallic with less surprising behavior.

Spin transfer torque dependence with respect the system size

In this section we devote our analysis to the size dependence of the spin transfer torque. We compare the variations in the STT when changed the length L, the width W and the separation of the magnets d for $\theta = \pi/4$, $\pi/2$ and $3\pi/4$. Because we are interested in the robustness of the STT we focus on results considering systems at $T = 300$ K. To calculate the torque at 300 K we considered the following equation:

$$\boldsymbol{\tau}(T) = \int \boldsymbol{\tau}(0) \left(\frac{-\partial f}{\partial E} \right) dE, \tag{4.24}$$

where $\boldsymbol{\tau}(0)$ is the torque at $T = 0$ K and $f = \frac{1}{e^{(E-\mu)/k_B T}+1}$ is the Fermi-Dirac distribution in which μ and T indicate electrochemical potential and temperature, respectively. We include again for convenience in all figures presented in this section the YIG band structure

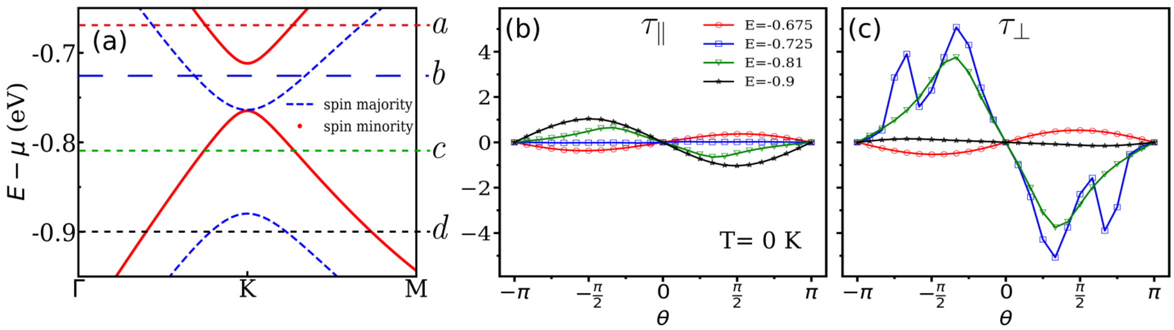

Figure 4.6: (a) YIG band structure for which four different energy values are highlighted with dashed lines, a, b, c, d correspond to the energies -0.675, -0.725, -0.81 and -0.9 eV respectively. (b) and (c) are the in-plane $\tau_{\parallel}$ and out of plane $\tau_{\perp}$ STT components as a function of the angle θ for the four chosen energies in (a).

showing the corresponding energy regions, discussed earlier. The green shaded regions correspond to regions where both spin channels are present as in Fig. 4.3, while the green dashed line separates the half-metallic regions white and pink regions. Fig. 4.7(a), (b) and (c) show the dependence of the STT with respect to the length L for three different angles, $\theta = \pi/4$, $\theta = \pi$ and $\theta = 3\pi/4$ for each torque component, in-plane (a2), (b2) and (c2) and out of plane (a3), (b3) and (c3). Let us focus first on the in-plane components presented in panels (a2), (b2) and (c2). We see that the in-plane torque does not present appreciable variations when θ is changed. We see that for big enough L, around 20 nm, the torque becomes positive for electron bands and remain negative for the hole bands. This behavior can be understood as the system needs a minimum length in order to polarize the electrons, something similar to what happened with the PMR L dependence (see for example Fig. 3.6(a4)). The behavior of the out of plane components (panels (a3), (b3) and (b4)) will be discussed later.

Fig. 4.8 shows the dependence of the STT as a function of the width W for the same angles considered previously. We see that the in-plane shape do not change qualitatively when the angle is changed. For small widths the torques are small and there is not a clear difference between the electron and the hole bands contributions. This difference becomes noticeable after around $W = 20$ nm. Most importantly, one can clearly notice that the in-plane component of STT oscillates as a function of W. The origin of these oscillations is related to quantum well states and the channel number available for transport in the nanoribbon. The out of plane component shows a huge dependence on the angle and present strong resonant-like peaks especially for energies corresponding to half-metallic behavior (cases b and c) with few channels available for transport. An interpretation for this behavior will be given later.

Fig. 4.9 shows the dependence of the STT as a function separation between the magnets d. We see in this case again that there is not a qualitative dependence of the in-plane component of the torque with respect the angle, remaining of the same order regardless

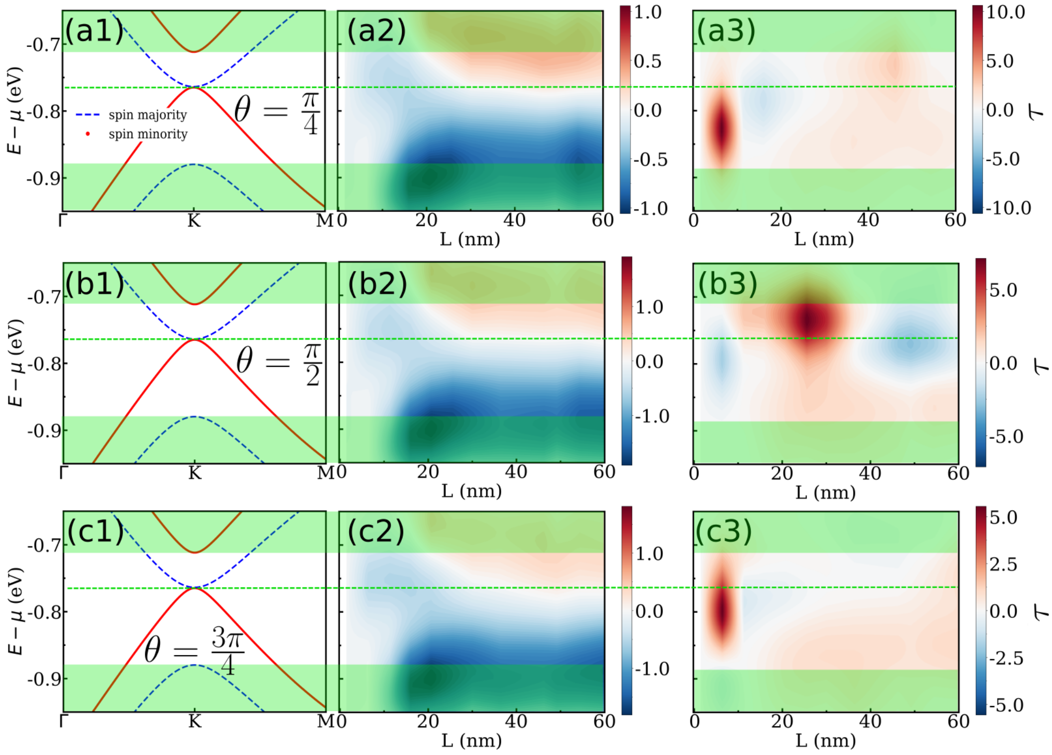

Figure 4.7: (1) YIG band structure, (2) in-plane STT component as a function of energy and magnet's length L and (3) out of plane STT as a function of energy and L for three different angles (a) $\pi/4$, (b) $\pi/2$ and (c) $3\pi/4$. The green shaded regions indicates the energy regions where there are both contributions of spin channels and the dashed line separates the half-metallic regions according to Fig. 4.3.

of the value of d. The torque in the electron bands is always positive, while in the hole bands is negative. In fact, this is a common feature of the figures presented. This behavior is understood as a change in the polarization, due to the higher number of minority channels in the electron bands when compared with the majority channels and the reverse situation in the hole bands.

The main question of this section is why the in-plane and out plane components behave so differently. Let us consider the free electron model to understand what is happening. This is studied using a very simple model with one ferromagnet and one barrier like in Ref. [127] or a more elaborated, considering two ferromagnets and a barrier as in Ref. [74]. For pedagogical purposes, we consider the STT expression obtained from Ref. [127]:

$$\tau = \frac{A}{\Omega}\frac{\hbar^2 k}{2m}\sin\theta[1 - Re(t_\uparrow t_\downarrow^* + r_\uparrow r_\downarrow^*)]\hat{e}_x - \frac{A}{\Omega}\frac{\hbar^2 k}{2m}\sin\theta Im(t_\uparrow t_\downarrow^* + r_\uparrow r_\downarrow^*)\hat{e}_y, \tag{4.25}$$

where Ω is a normalization volume, m is the electron mass and the parameters t_σ, r_σ, are the transmission and reflection amplitudes for the electron with spin $\sigma =\uparrow (\downarrow)$. The component along the x axis correspond to the in-plane torque, while the component along the y-axis to the out of plane torque. It can be seen that the in-plane torque

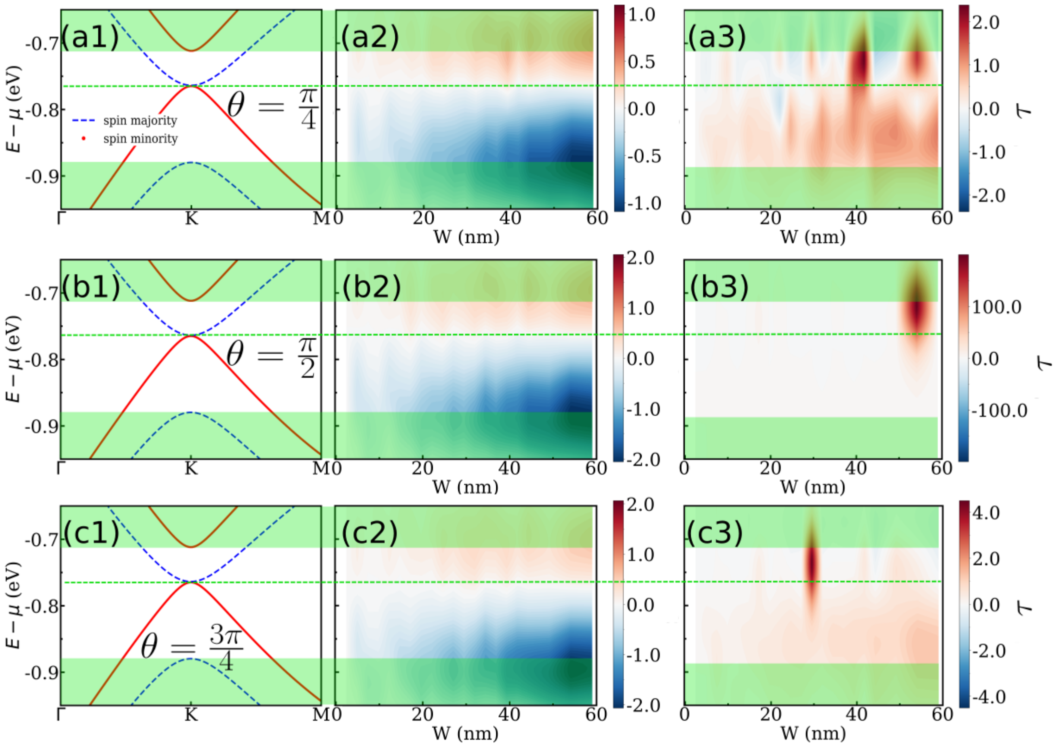

Figure 4.8: (1) YIG band structure, (2) in-plane STT component as a function of energy and magnet's width W and (3) out of plane STT as a function of energy and W for three different angles (a) $\pi/4$, (b) $\pi/2$ and (c) $3\pi/4$. The green shaded regions indicates the energy regions where there are both contributions of spin channels and the dashed line separates the half-metallic regions according to Fig. 4.3.

depends on the real part of the sum of the transmission and reflection mix components, in contrast with the out of plane, which depends on the imaginary part. We hypothesize that the real part of the mix transmission is dominant in the in-plane torque component, what would explains qualitatively its connection with the transmission. While in the out of plane torque, the imaginary part of the mix reflection is dominant, what lead us to speculate that the huge peaks found in Figs. 4.7, 4.8 and 4.9 are a consequence of multiple reflections that eventually leads to constructive interferences. To prove this hypothesis further research is needed.

4.5 Critical current estimation

The STT phenomena allowing to switch the magnetization orientation of magnets have been extensively used in the development of memories as MRAM [128]. In order to create viable devices it is necessary to minimize the current necessary to generate switching. The STT phenomena were studied mainly in semiconductor devices [129], as well as, with transition metal magnets, for which it has been found values as low as 9 μA in Fe-based low-damping perpendicular structures [130]. In this section we will calculate the critical

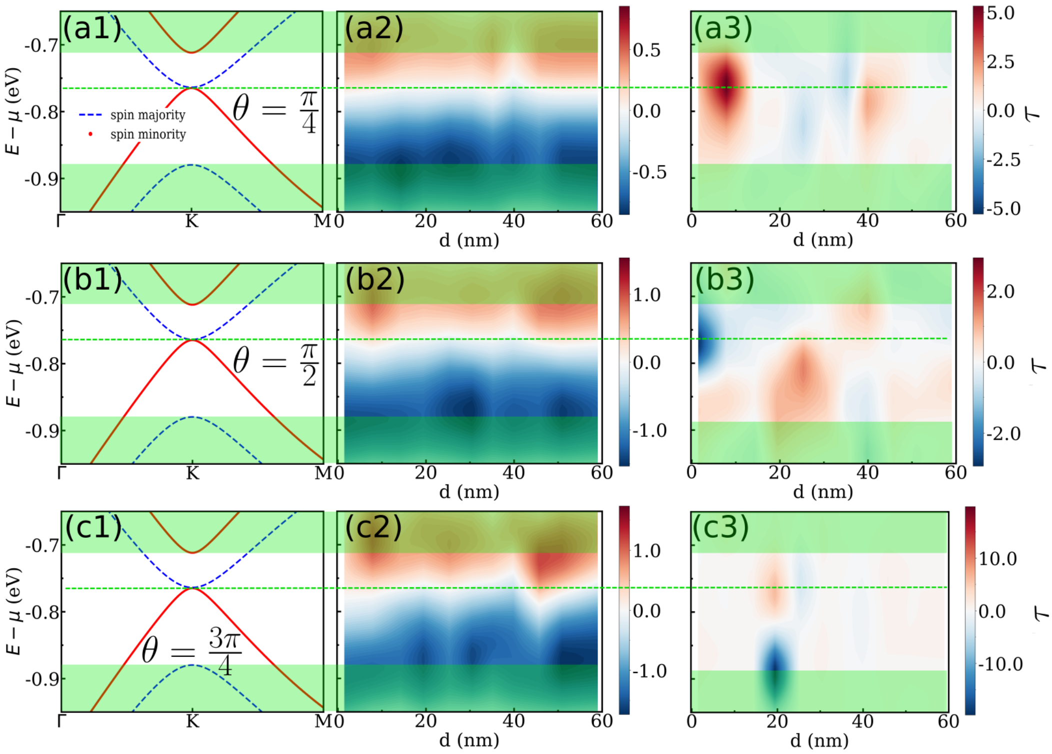

Figure 4.9: (1) YIG band structure, (2) in-plane STT component as a function of energy and magnet's separation d and (3) out of plane STT as a function of energy and d for three different angles (a) $\pi/4$, (b) $\pi/2$ and (c) $3\pi/4$. The green shaded regions indicates the energy regions where there are both contributions of spin channels and the dashed line separates the half-metallic regions according to Fig. 4.3.

current I_c for the graphene-based lateral spin valve presented in Fig. 4.1 considering magnets made of YIG.

4.5.1 In-plane torque fitting via Slonczewski's formula

Let us now, analyze the behavior of the in plane torque, that is the one responsible for the switching. With this objective in mind we fitted the values obtained with the following formula:

$$\tau(\theta) = \frac{\beta \sin\theta}{\Lambda \cos^2\frac{\theta}{2} + \frac{1}{\Lambda}\sin^2\frac{\theta}{2}}, \text{ with } \Lambda \neq 0, \tag{4.26}$$

which is the Slonczewski's formula for the reduced torque [131]. Λ depends on the length of the magnet and affects the amplitude and angular dependence of the torque, while β is related to the current polarization and only affects the amplitude of the torque [131] and by consequence has torque units (e). Fig. 4.10 shows the corresponding fitting for (a) E = -0.675 eV, (b) E = -0.725 eV, (c) E = -0.81 eV, (d) E = -0.9 eV. The curves overlap for a and d, while for b and c we start to see deviations indeed. Of great interest is to determine whether the torque is bigger near $\theta = 0$ or $\theta = \pi$. This will give us valuable information about the existence of different critical currents to switch the free layer. To do so we can use the following relation from Ref. [131]

$$\Lambda^2 = \chi + 1. \tag{4.27}$$

If $\chi < 0$ it implies we will have larger in-plane torque near $\theta = \pi$, while if $\chi > 0$ the in-plane torque will be larger near $\theta = 0$. Table 4.2 summarizes the fitted parameters Λ and β and the corresponding χ for each energy. From the obtained χ values we see that for the energies -0.725 eV, -0.81 eV and -0.9 eV the torque is larger near $\theta = \pi$, while for E = -0.675, the torque is larger near to $\theta = 0$, so qualitatively, there are different critical current to switch to 0 or π the magnetization of M_2.

Table 4.2: fitted parameters Λ, β and χ obtained for YIG using Eqs. (4.26) and (4.27) for four different energies

Energy (eV)	β	Λ	χ
-0.675	0.102	-1.198	0.434
-0.725	0.38	0.342	-0.883
-0.81	0.308	0.528	-0.721
-0.9	0.73	0.92	-0.154

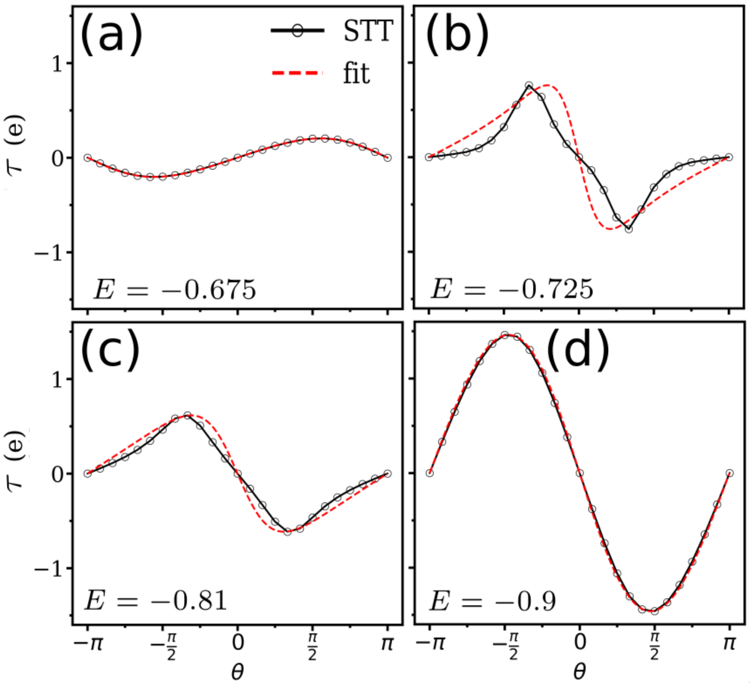

Figure 4.10: In-plane STT as a function of the angle θ and the corresponding fitting with Eq. (4.26) for the energies (a) -0.675 eV, (b) -0.725 eV, (c) -0.81 eV and (d) -0.9 eV.

4.5.2 Phase diagram from the LLG equation

Let us study the different phases of our system. To obtain the phase diagram we need to solve the LLG equation from Eq. (2.97) substituting $\boldsymbol{M}$ by M_1 and $\boldsymbol{m}$ by M_2

$$\frac{\partial \boldsymbol{M_2}}{\partial t} = \boldsymbol{M_2} \times \frac{1}{\hbar S_0} \frac{\partial E}{\partial \boldsymbol{M_2}} + \alpha \boldsymbol{M_2} \times \frac{\partial \boldsymbol{M_2}}{\partial t} + \frac{I}{e S_0} g(\boldsymbol{M_2} \cdot \boldsymbol{M_1}) \boldsymbol{M_2} \times (\boldsymbol{M_1} \times \boldsymbol{M_2}), \quad (4.28)$$

where e is the electron charge, I the current flowing through the system, α is the Gilbert damping parameter and S_0 the total spin of the magnet considered. E is the magnetic energy, $\boldsymbol{M_1}$ and $\boldsymbol{M_2}$ are the magnetizations of the magnetic layers and $g(\boldsymbol{M_2} \cdot \boldsymbol{M_1})$ is a function that mimics the torque created in the system. Without loss of generality the magnetic energy is

$$E(\boldsymbol{M_2}) = -\kappa S_0 (\boldsymbol{M_2} \cdot \boldsymbol{M_1})^2 - g \mu_B S_0 \boldsymbol{\mathcal{H}} \cdot \boldsymbol{M_2}, \quad (4.29)$$

where the first term corresponds to the uniaxial anisotropy and the second one to the coupling of the moment $\boldsymbol{M_2}$ with the external field $\mathbf{H}$ (Zeeman coupling). For $\boldsymbol{M_2}$ along the x-z plane and $\boldsymbol{M_1}$ along the z-axis with $|\boldsymbol{M_1}| = |\boldsymbol{M_2}| = 1$ and $\boldsymbol{\mathcal{H}} = \mathcal{H} \hat{e}_z$, we obtain the following expression for the time derivative of the magnetic energy:

$$\frac{\partial E}{\partial \boldsymbol{M_2}} = \left(\frac{-2\kappa S_0 \cos\theta + g \mu_B S_0 \mathcal{H}}{\hbar} \right) \hat{e}_z \quad (4.30)$$

Following the procedure presented in Ref. [132] we solve the LLG equation in spherical coordinates and find:

$$\dot{\theta} = -\alpha \dot{\phi} \sin\theta - \frac{I}{e S_0} g(\theta) \sin\theta \quad (4.31)$$

$$\dot{\phi} \sin\theta = \alpha \dot{\theta} + \frac{2\kappa}{\hbar} \cos\theta \sin\theta + \gamma \mathcal{H}, \quad (4.32)$$

where $\gamma = g\mu_B/\hbar$. In our case we express $g(\theta)$ as:

$$g(\theta) = \frac{\Lambda \beta}{(\Lambda^2 + 1) + (\Lambda^2 - 1)\cos\theta}, \quad (4.33)$$

which is the basically the denominator of Eq. (4.26) after the use of some trigonometrical identities. Using the previous equation and substituting Eq. (4.32) into Eq. (4.31) we obtain:

$$\dot{\theta} = \left(\frac{-2\kappa\alpha}{\hbar} \right) \frac{1}{1+\alpha^2} \left(\cos\theta \sin\theta + \frac{\hbar \gamma \mathcal{H}}{2\kappa} \sin\theta + \frac{\hbar I}{2\kappa\alpha e S_0} \frac{\Lambda \beta \sin\theta}{(\Lambda^2 + 1) + (\Lambda^2 - 1)\cos\theta} \right), \quad (4.34)$$

and we can rewrite this equation as:

$$\dot{u} = \left(\frac{-2\kappa\alpha(1-u^2)}{\hbar(1+\alpha^2)}\right)\left(u + \bar{H} + \frac{q'\bar{I}}{1+qu}\right) \tag{4.35}$$

where we have defined $u = \cos\theta$, $\bar{H} = \frac{\hbar\gamma\mathcal{H}}{2\kappa}$, $\bar{I} = \frac{\hbar I\beta}{2\kappa\alpha e S_0}$, $q = \frac{\Lambda^2-1}{\Lambda^2+1}$ and $q' = \frac{\Lambda}{\Lambda^2+1}$. The phase diagram is constructed from the analysis of stability of zeros in the equation $R(u) = \dot{u}$ and their corresponding derivatives $\partial_u R(u) < 0$. It is straightforward to see that Eq. (4.35) is zero when $u = \pm 1$ ($\theta = 0, \pi$), so we can write down the corresponding stability equations as:

for u= +1

$$\bar{I} > \frac{-\bar{H} - q - (q\bar{H}+1)}{q'} \tag{4.36}$$

for u= -1

$$\bar{I} < \frac{-\bar{H} - q + (q\bar{H}+1)}{q'} \tag{4.37}$$

The other two zeros are obtained by solving the equation $u + qu^2 + \bar{H} + q\bar{H} + q'\bar{I} = 0$, so

$$u = \frac{-(q\bar{H}+1) \pm \sqrt{(q\bar{H}+1)^2 - 4q(q'\bar{I}+\bar{H})}}{2q}, \tag{4.38}$$

from where two roots are obtained, u_1 for the (+) case and u_2 for the (−) case. We get as well from Eq. (4.38) the following condition:

$$\bar{I} < \frac{(q\bar{H}-1)^2}{4qq'}, \tag{4.39}$$

After numerical implementation we find that u_2 is stable and u_1 is not by using the criteria $\partial_u R(u) < 0$. Employing this analysis and Eqs. (4.36), (4.37) and (4.38) we build the phase diagram shown in Fig. 4.11. We see that there are five different regions: (−1) and (+1) regions correspond to stable fixed points for $u = -1$ and $u = 1$, respectively. In the $(-1, 1)$ region we have the unstable fixed point u_1, as well as, the fixed points $u = -1$ and $u = 1$. In the (SP) region there is the intermediate point $-1 < u_2 < 1$ that correspond to a spin precession state. In the (SP,+1) region (in gray) we have the coexistence of two stable fixed points, $u = 1$ and u_2, and one unstable fixed point u_1. The existence of this region removes the possibility of switching the magnet without hysteresis [132], what implies we will have different currents to switch to the parallel state and to the antiparallel state.

Let us now estimate the order of magnitude of the critical current, to do so let us calculate the phase diagram for a thin YIG magnet using parameters reported in the literature. For our calculation we used damping $\alpha = 9\times10^{-5}$ [133], perpendicular uniaxial anisotropy $H_k = -3.75\times10^{-3}$ T [134], saturation magnetization $M_s = 0.176$ (T/μ_0) [133] and gyromagnetic ratio $\gamma = 1.79\times10^{11}$ T^{-1}s^{-1} [133]. The dimension of the magnets are:

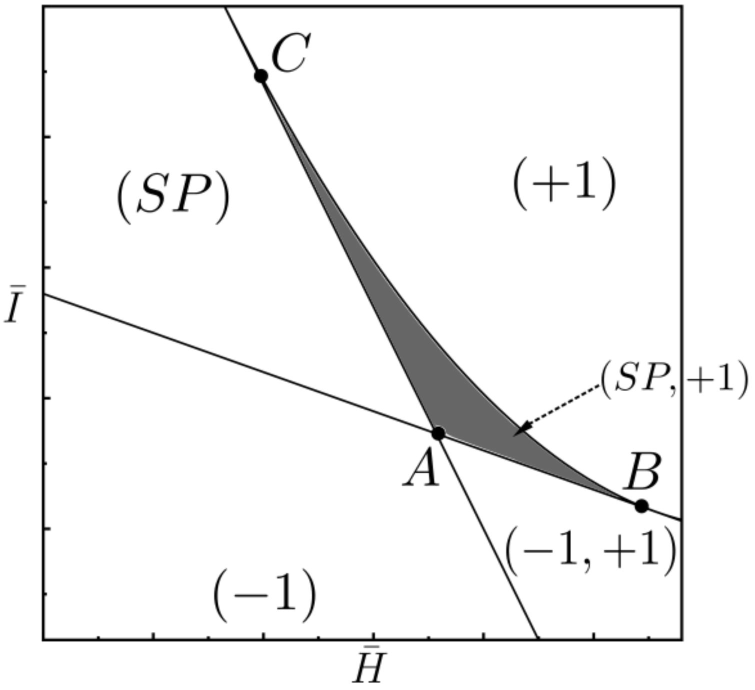

Figure 4.11: Phase diagram of the LLG Eq. (4.28). Each region is denoted differently according to the stability and number of fixed points on it. The different intersections of the curves have coordinates $A = \left(-2 - \frac{1}{q}, \frac{(q+1)^2}{qq'}\right)$, $B = \left(2 - \frac{1}{q}, \frac{(-q+1)^2}{qq'}\right)$ and $C = \left(-\frac{1}{q}, \frac{1-q}{qq'}\right)$.

thickness $t = 20$ nm, length $L = 49$ nm, width $W = 39$ nm. To obtain κ we need to use the following formula:

$$\kappa = \frac{H_k M_s}{2}, \tag{4.40}$$

so $\kappa = -2.57 \times 10^2$ J/m^2. Very important to say is that κ depends on temperature and magnet's thickness, and can even change its sign depending on the configuration of the system [134]. This is crucial while analyzing the phase diagram. The last parameter we need is the total spin S_0. To do so we can use the following formula [135]:

$$S_0 = \frac{|\boldsymbol{M}|}{\hbar\gamma}, \tag{4.41}$$

where $\boldsymbol{M}$ is the total magnetic moment of the magnet. We can get the value of $\boldsymbol{M}$ by multiplying the total number of unit cells in the magnet by the magnetic moment of a single unit cell of YIG, whose magnetic moment is 40 μ_B [136, 137]. The total spin in the ferromagnet is then

$$S_0 = \frac{20 \times 39 \times 49}{(1.238)^3} \times \frac{40\mu_B}{\hbar\gamma} \approx 3.96 \times 10^6, \tag{4.42}$$

where we have used 1.238 nm as the YIG's lattice parameter [136]. Fig. 4.12 shows the phase diagram obtained for YIG at $E = -0.81$ eV, an energy in a half-metallic region (pink region according to Fig. 4.3) were the transmission has low values. It is well-known that the critical current is inversely proportional to the STT efficiency defined as $\eta = \frac{\tau}{T^{tot}}$, so the smaller the transmission the higher η and as a consequence the smaller the current. One can see that the diagram conserves qualitatively the same shape as Fig. 4.11, so the discussions done there for each region are valid here too. The main difference is the position of the (+1) and (-1) zones that in Fig. 4.12 are inverted with respect to Fig. 4.11 due to the negative κ value. Note that the magnetic field values necessary to access some regions of the phase diagram are of the order of 1×10^3 T what makes them experimentally inaccessible. So, let us focus on low field cases. An estimation of the critical currents to switch either to the (+1) or (-1) state at $H = 0$ T(red dashed line) can be done looking at the crossing with the curves that separates different phases. For (+1) and (-1) states the critical currents are -0.084 and 0.024 A, respectively. Further research is necessary to confirm if total switching of the magnet is possible and more accurate models should be developed to confirm the values estimated.

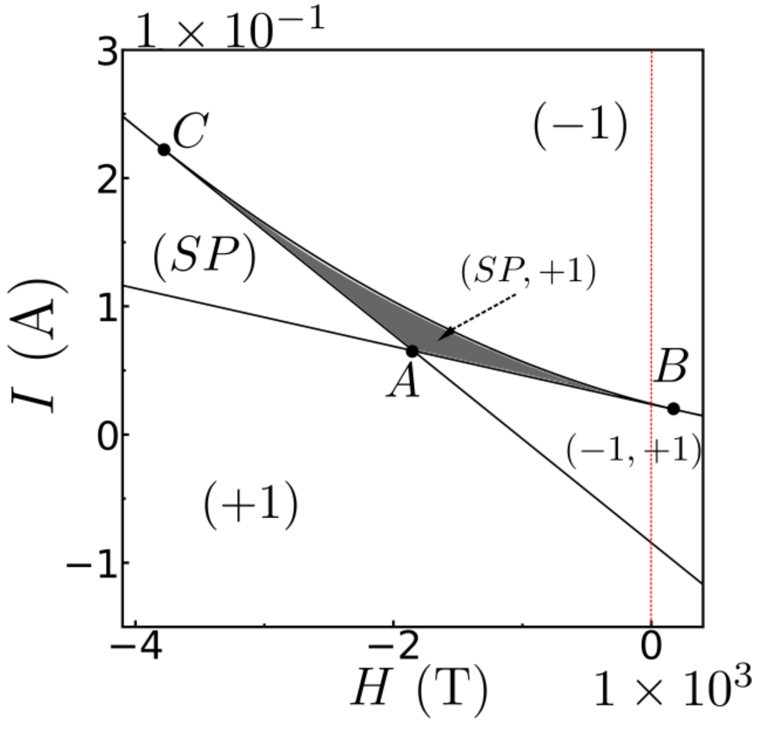

Figure 4.12: Phase diagram of YIG obtained by solving the LLG Eq. (4.28). Each region is denoted differently according to the stability and number of fixed points on it. The different intersections of the curves have coordinates $A = (-1.85 \times 10^3, 0.065)$, $B = (252, 0.018)$ and $C = (-3.9 \times 10^3, 0.23)$. The red dashed line highlights the field $H = 0$ T.

4.6 Conclusion

The STT phenomena in a graphene-based lateral spintronic device with YIG magnets have been studied theoretically using the tight-binding model. We have derived the corresponding steady state spin current conservation equation for the graphene case when the system has spin dependent hoppings and sublattice potential. This equation allowed to simulate the in-plane and out of plane STT components, for which an angular and size dependence study was made. Our results show that the in-plane torque present a sinus-like behavior at any energy value, while the out plane one behaves differently depending on the energy region where the torque is calculated. We explain this behavior as a consequence of the number of channels available and quantum tunneling. In connection with these results found that the out of plane torque component is highly dependent on the size of the system showing peaks at some particular dimension values as consequence of constructive interference and number of channels in play at different energies. Further studies are necessary in order to confirm this hypothesis. Finally, for a thin YIG layer of 20 nm we calculated the STT phase diagram of a graphene-based spin valve and found currents of the order of 0.1 A. If the switching is possible in this device, according to our estimation, the critical current is of the order of 10 mA.

CHAPTER 5

Conclusions and perspectives

In this thesis we have provided a detailed study of the magnetoresistance and spin transfer torque phenomena in a proposed graphene-based lateral spin valve system. By using the tight-binding approach, we derived the Hamiltonian of the device and employed the scattering matrix method, implemented in the python quantum transport package Kwant, to systematically investigate transport properties of the system.

We demonstrated the existence of the proximity magnetoresistance (PMR) effect in graphene in the proximity of different MIs: Yttrium Iron garnet(YIG), Cobalt ferrite(CFO), Europium oxide(EuO) and Europium sulfide(EuS). We showed that PMR is robust with respect to the dimensions of the system and presented a study on PMR dependence of YIG-based device on edge termination and SOC at room temperature, due to its potential for applications. Furthermore, we investigated the interplay of electrical polarizations and magnetizations on the proposed device based on the multiferroic material bismuth ferrite (BFO) and studied the conductance for different combinations of these quantities that appeared as a consequence of the new degree of freedom. In order to quantify these combinations, we introduced two novel phenomena PER and PMER and studied their dependence with respect to the size of the system. We demonstrated that it is possible to tune the magneto-transport properties of the system by changing the electrical polarization of the material.

To study the STT phenomenon in the aforementioned device with magnets made of YIG, we derived the steady state spin current conservation equation for graphene when it has spin dependent hoppings and sublattice potential. This equation allowed us to simulate the in-plane and out of plane STT components, for which an angular and size dependence study was performed. We found that the in-plane torque is well behaved, while the out of plane component behavior depends on the energy regime it is calculated.

Also, we showed the dependence of the torque components as a function of the dimension of the system and found unexpected behaviors. We hypothesized that there is a strong relation between the real part of the mix transmission with the in-plane, as well as the imaginary part of the mix reflection with the out of plane torque component. Finally, we presented STT switching diagrams and estimated critical currents of the order of 10 mA, being the latter the current needed to switch the magnetization of the immediate graphene region in contact with the magnet that may switch eventually the magnetic orientation of the whole magnet.

The findings of this work can be used for the development of new devices, for instance, proximity magnetoresistance memories and devices with four logical gates instead of two. Most importantly, we have introduced several novel phenomena in graphene-based lateral device with proximity-induced magnetism. There are many open problems that can be studied with a similar setup, for example simulate Hanle measurements in the system, study transport in the quantum anomalous Hall effect (QAHE) regime or in twisted bilayer graphene. Graphene has still a lot of potential!

Bibliography

[1] J. M. D. Coey, *Magnetism and Magnetic Materials* (Cambridge University Press, 2010).

[2] D. J. Griffiths, *Introduction to electrodynamics*, 3rd ed. (Prentice Hall, 1999).

[3] W. Nolting and A. Ramakanth, *Quantum Theory of Magnetism* (Springer-Verlag Berlin Heidelberg, 2009).

[4] S. Blundell, *Magnetism In Condensed Matter* (Oxford University Press, 2001).

[5] T. William, "XIX. *on the electro-dynamic qualities of metals:—effects of magnetization on the electric conductivity of nickel and of iron,*" Proc. R. Soc. Lond. **8** (1857), 10.1098/rspl.1856.0144.

[6] P. M. Tedrow and R. Meservey, *"Spin-dependent tunneling into ferromagnetic nickel,"* Phys. Rev. Lett. **26**, 192 (1971).

[7] M. Julliere, *"Tunneling between ferromagnetic films,"* Physics Letters A **54**, 225 (1975).

[8] M. N. Baibich, J. M. Broto, A. Fert, F. N. Van Dau, F. Petroff, P. Etienne, G. Creuzet, A. Friederich, and J. Chazelas, *"Giant magnetoresistance of (001)* Fe*/(001)* Cr *magnetic superlattices,"* Phys. Rev. Lett. **61**, 2472 (1988).

[9] G. Binasch, P. Grünberg, F. Saurenbach, and W. Zinn, *"Enhanced magnetoresistance in layered magnetic structures with antiferromagnetic interlayer exchange,"* Phys. Rev. B **39**, 4828 (1989).

[10] N. F. Mott and R. H. Fowler, *"The electrical conductivity of transition metals,"* Proc. R. Soc. Lond. A. **153** (1936), 10.1098/rspa.1936.0031.

[11] A. Fert, *"Nobel lecture: Origin, development, and future of spintronics,"* Rev. Mod. Phys. **80**, 1517 (2008).

[12] J. C. Slonczewski, *"Conductance and exchange coupling of two ferromagnets separated by a tunneling barrier,"* Phys. Rev. B **39**, 6995 (1989).

[13] J. S. Moodera, L. R. Kinder, T. M. Wong, and R. Meservey, *"Large magnetoresistance at room temperature in ferromagnetic thin film tunnel junctions,"* Phys. Rev. Lett. **74**, 3273 (1995).

[14] W. H. Butler, X.-G. Zhang, T. C. Schulthess, and J. M. MacLaren, *"Spin-dependent tunneling conductance of* Fe|MgO|Fe *sandwiches,"* Phys. Rev. B **63**, 054416 (2001).

[15] J. Mathon and A. Umerski, *"Theory of tunneling magnetoresistance of an epitaxial* Fe/MgO/Fe*(001) junction,"* Phys. Rev. B **63**, 220403 (2001).

[16] S. Yuasa, T. Nagahama, A. Fukushima, Y. Suzuki, and K. Ando, *"Giant room-temperature magnetoresistance in single-crystal* Fe/MgO/Fe *magnetic tunnel junctions,"* Nature Materials **3**, 868 (2004).

[17] S. S. P. Parkin, C. Kaiser, A. Panchula, P. M. Rice, B. Hughes, M. Samant, and S.-H. Yang, *"Giant tunnelling magnetoresistance at room temperature with* MgO *(100) tunnel barriers,"* Nature Materials **3**, 862 (2004).

[18] Y. M. Lee, J. Hayakawa, S. Ikeda, F. Matsukura, and H. Ohno, *"Effect of electrode composition on the tunnel magnetoresistance of pseudo-spin-valve magnetic tunnel junction with a* MgO *tunnel barrier,"* Applied Physics Letters **90**, 212507 (2007).

[19] E. Y. Tsymbal and I. Zutic, *Handbook of Spin Transport and Magnetism* (Chapman and Hall/CRC, 2012).

[20] Y. Xu, D. D. Awschalom, and J. Nitta, *Handbook of Spintronics* (Springer, Dordrecht, 2016).

[21] S. Schubin, S. Wonsowsky, and R. H. Fowler, *"On the electron theory of metals,"* Proc. R. Soc. Lond. A. **145**, 159 (1934).

[22] C. Huan, *"Spin current,"* Contemporary Physics **55**, 127 (2014), https://doi.org/10.1080/00107514.2013.877970 .

[23] C. A. Akosa, *"Spin Transport in Ferromagnetic andAntiferromagnetic Textures"*, Ph.D. thesis, King Abdullah University of Science and Technology, Thuwal, Kingdom of Saudi Arabia (2012).

[24] H. Zeng, J. Dai, W. Yao, D. Xiao, and X. Cui, *"Valley polarization in* MoS_2 *monolayers by optical pumping,"* Nature Nanotechnology **7**, 490 (2012).

[25] W. Han, *"Perspectives for spintronics in 2*D *materials,"* APL Materials **4**, 032401 (2016), https://doi.org/10.1063/1.4941712 .

[26] A. Manchon, H. C. Koo, J. Nitta, S. M. Frolov, and R. A. Duine, *"New perspectives for rashba spin-orbit coupling,"* Nature Materials **14**, 871 EP (2015), review article.

[27] Y. Bychkov and E. Rashba, *"Properties of a 2*D *electron gas with lifted spectral degeneracy (english),"* Phys. Rev. Lett. **39**, 78 (1984).

[28] G. Dresselhaus, *"Spin-orbit coupling effects in zinc blende structures,"* Phys. Rev. **100**, 580 (1955).

[29] V. M. Karpan, G. Giovannetti, P. A. Khomyakov, M. Talanana, A. A. Starikov, M. Zwierzycki, J. van den Brink, G. Brocks, and P. J. Kelly, *"Graphite and graphene as perfect spin filters,"* Phys. Rev. Lett. **99**, 176602 (2007).

[30] O. V. Yazyev and A. Pasquarello, *"Magnetoresistive junctions based on epitaxial graphene and hexagonal boron nitride,"* Phys. Rev. B **80**, 035408 (2009).

[31] M. Z. Iqbal, M. W. Iqbal, J. H. Lee, Y. S. Kim, S.-H. Chun, and J. Eom, *"Spin valve effect of* NiFe/graphene/NiFe *junctions,"* Nano Research **6**, 373 (2013).

[32] M. Z. Iqbal, N. A. Qureshi, and G. Hussain, *"Recent advancements in 2*D*-materials interface based magnetic junctions for spintronics,"* Journal of Magnetism and Magnetic Materials **457**, 110 (2018).

[33] M. Z. Iqbal, S. Siddique, G. Hussain, and M. W. Iqbal, *"Room temperature spin valve effect in the* NiFe/Gr–hBN/Co *magnetic tunnel junction,"* J. Mater. Chem. C **4**, 8711 (2016).

[34] P. U. Asshoff, J. L. Sambricio, A. P. Rooney, S. Slizovskiy, A. Mishchenko, A. M. Rakowski, E. W. Hill, A. K. Geim, S. J. Haigh, V. I. Fal'ko, I. J. Vera-Marun, and I. V. Grigorieva, *"Magnetoresistance of vertical* Co-graphene-NiFe *junctions controlled by charge transfer and proximity-induced spin splitting in graphene,"* 2D Materials **4**, 031004 (2017).

[35] M. Popinciuc, C. Józsa, P. J. Zomer, N. Tombros, A. Veligura, H. T. Jonkman, and B. J. van Wees, *"Electronic spin transport in graphene field-effect transistors,"* Phys. Rev. B **80**, 214427 (2009).

[36] B. Dlubak, M.-B. Martin, C. Deranlot, B. Servet, S. Xavier, R. Mattana, M. Sprinkle, C. Berger, W. A. De Heer, F. Petroff, A. Anane, P. Seneor, and A. Fert, *"Highly efficient spin transport in epitaxial graphene on* SiC*,"* Nature Physics **8**, 557 (2012).

[37] L. Banszerus, M. Schmitz, S. Engels, M. Goldsche, K. Watanabe, T. Taniguchi, B. Beschoten, and C. Stampfer, *"Ballistic transport exceeding 28 μm in* CVD *grown graphene,"* Nano Letters **16**, 1387 (2016), pMID: 26761190, https://doi.org/10.1021/acs.nanolett.5b04840 .

[38] N. Tombros, C. Jozsa, M. Popinciuc, H. T. Jonkman, and B. J. van Wees, *"Electronic spin transport and spin precession in single graphene layers at room temperature,"* Nature **448**, 571 (2007).

[39] W.-K. Tse, Z. Qiao, Y. Yao, A. H. MacDonald, and Q. Niu, *"Quantum anomalous hall effect in single-layer and bilayer graphene,"* Phys. Rev. B **83**, 155447 (2011).

[40] B. Dlubak, P. Seneor, A. Anane, C. Barraud, C. Deranlot, D. Deneuve, B. Servet, R. Mattana, F. Petroff, and A. Fert, *"Are* Al_2O_3 *and* MgO *tunnel barriers suitable for spin injection in graphene?"* Applied Physics Letters **97**, 092502 (2010).

[41] W. Han and R. K. Kawakami, *"Spin relaxation in single-layer and bilayer graphene,"* Phys. Rev. Lett. **107**, 047207 (2011).

[42] T.-Y. Yang, J. Balakrishnan, F. Volmer, A. Avsar, M. Jaiswal, J. Samm, S. R. Ali, A. Pachoud, M. Zeng, M. Popinciuc, G. Güntherodt, B. Beschoten, and B. Özyilmaz, *"Observation of long spin-relaxation times in bilayer graphene at room temperature,"* Phys. Rev. Lett. **107**, 047206 (2011).

[43] T. Maassen, J. J. van den Berg, N. IJbema, F. Fromm, T. Seyller, R. Yakimova, and B. J. van Wees, *"Long spin relaxation times in wafer scale epitaxial graphene on* SiC*(0001),"* Nano Letters **12**, 1498 (2012), pMID: 22324998, http://dx.doi.org/10.1021/nl2042497 .

[44] A. W. Cummings and S. Roche, *"Effects of dephasing on spin lifetime in ballistic spin-orbit materials,"* Phys. Rev. Lett. **116**, 086602 (2016).

[45] D. Van Tuan, F. Ortmann, A. W. Cummings, D. Soriano, and S. Roche, *"Spin dynamics and relaxation in graphene dictated by electron-hole puddles,"* Scientific Reports **6**, 21046 EP (2016), article.

[46] A. H. Castro Neto, F. Guinea, N. M. R. Peres, K. S. Novoselov, and A. K. Geim, *"The electronic properties of graphene,"* Rev. Mod. Phys. **81**, 109 (2009).

[47] S. Roche, J. Åkerman, B. Beschoten, J.-C. Charlier, M. Chshiev, S. P. Dash, B. Dlubak, J. Fabian, A. Fert, M. Guimarães, F. Guinea, I. Grigorieva, C. Schönenberger, P. Seneor, C. Stampfer, S. O. Valenzuela, X. Waintal, and B. van Wees, *"Graphene spintronics: the european flagship perspective,"* 2*D* Materials **2**, 030202 (2015).

[48] D. L. Björn Trauzettel, Denis V. Bulaev and G. Burkard, *"Spin qubits in graphene quantum dots,"* Nat. Phys. **3**, 192 (2007).

[49] H.-S. P. Wong and D. Akinwande, *Carbon Nanotube and Graphene Device Physics* (Cambridge University Press, 2010).

[50] C. Gutiérrez, L. Brown, C.-J. Kim, J. Park, and A. N. Pasupathy, *"Klein tunnelling and electron trapping in nanometre-scale graphene quantum dots,"* Nature Physics **12**, 1069 (2016).

[51] K. Nakada, M. Fujita, G. Dresselhaus, and M. S. Dresselhaus, *"Edge state in graphene ribbons: Nanometer size effect and edge shape dependence,"* Phys. Rev. B **54**, 17954 (1996).

[52] A. Kimouche, M. M. Ervasti, R. Drost, S. Halonen, P. M. Harju, Ari Joensuu, J. Sainio, and P. Liljeroth, *"Ultra-narrow metallic armchair graphene nanoribbons,"* Nat. Comm. **6** (2015), doi:10.1038/ncomms10177.

[53] Y.-W. Son, M. L. Cohen, and S. G. Louie, *"Half-metallic graphene nanoribbons,"* Nat. Phys. **444**, 347 (2007).

[54] O. V. Yazyev, *"A guide to the design of electronic properties of graphene nanoribbons,"* Accounts of Chemical Research **46**, 2319 (2013), pMID: 23282074, http://dx.doi.org/10.1021/ar3001487 .

[55] Y.-W. Son, M. L. Cohen, and S. G. Louie, *"Energy gaps in graphene nanoribbons,"* Phys. Rev. Lett. **97**, 216803 (2006).

[56] F. Libisch, S. Rotter, and J. Burgdörfer, *"Coherent transport through graphene nanoribbons in the presence of edge disorder,"* New Journal of Physics **14**, 123006 (2012).

[57] M. Wimmer, İ. Adagideli, S. Berber, D. Tománek, and K. Richter, *"Spin currents in rough graphene nanoribbons: Universal fluctuations and spin injection,"* Phys. Rev. Lett. **100**, 177207 (2008).

[58] J. Hong, E. Bekyarova, P. Liang, W. A. de Heer, R. C. Haddon, and S. Khizroev, *"Room-temperature magnetic ordering in functionalized graphene,"* Scientific Reports **2**, 624 (2012).

[59] A. J. M. Giesbers, K. Uhlířová, M. Konečný, E. C. Peters, M. Burghard, J. Aarts, and C. F. J. Flipse, *"Interface-induced room-temperature ferromagnetism in hydrogenated epitaxial graphene,"* Phys. Rev. Lett. **111**, 166101 (2013).

[60] O. V. Yazyev and L. Helm, *"Defect-induced magnetism in graphene,"* Phys. Rev. B **75**, 125408 (2007).

[61] J. A. Fürst, J. G. Pedersen, C. Flindt, N. A. Mortensen, M. Brandbyge, T. G. Pedersen, and A.-P. Jauho, *"Electronic properties of graphene antidot lattices,"* New Journal of Physics **11**, 095020 (2009).

[62] H.-X. Yang, M. Chshiev, D. W. Boukhvalov, X. Waintal, and S. Roche, *"Inducing and optimizing magnetism in graphene nanomeshes,"* Phys. Rev. B **84**, 214404 (2011).

[63] H. X. Yang, A. Hallal, D. Terrade, X. Waintal, S. Roche, and M. Chshiev, *"Proximity Effects Induced in Graphene by Magnetic Insulators: First-Principles Calculations on Spin Filtering and Exchange-Splitting Gaps,"* Phys. Rev. Lett. **110**, 046603 (2013).

[64] K. Zollner, M. Gmitra, T. Frank, and J. Fabian, *"Theory of proximity -induced exchange coupling in graphene on* hBN/(Co, Ni)*,"* Phys. Rev. B **94**, 155441 (2016).

[65] Z. Wang, C. Tang, R. Sachs, Y. Barlas, and J. Shi, *"Proximity-induced ferromagnetism in graphene revealed by the anomalous hall effect,"* Phys. Rev. Lett. **114**, 016603 (2015).

[66] P. Wei, S. Lee, F. Lemaitre, L. Pinel, D. Cutaia, W. Cha, F. Katmis, Y. Zhu, D. Heiman, J. Hone, J. S. Moodera, and C.-T. Chen, *"Strong interfacial exchange field in the* graphene/EuS *heterostructure,"* Nat. Mater. **15**, 711 (2016).

[67] J. C. Leutenantsmeyer, A. A. Kaverzin, M. Wojtaszek, and B. J. van Wees, *"Proximity induced room temperature ferromagnetism in graphene probed with spin currents,"* 2*D*. Mater. **4**, 1 (2016).

[68] H. Haugen, D. Huertas-Hernando, and A. Brataas, *"Spin transport in proximity-induced ferromagnetic graphene,"* Phys. Rev. B **77**, 115406 (2008).

[69] W. Han, R. K. Kawakami, M. Gmitra, and J. Fabian, *"Graphene spintronics,"* Nature Nanotechnology **9**, 794 EP (2014), review article.

[70] I. Žutić, A. Matos-Abiague, B. Scharf, H. Dery, and K. Belashchenko, *"Proximitized materials,"* Materials Today **22**, 85 (2019).

[71] W. Han, R. K. Kawakami, M. Gmitra, and J. Fabian, *"Graphene spintronics,"* Nature Nanotechnology **9**, 794 EP (2014), review article.

[72] S. Datta, *Electronic Transport in Mesoscopic Systems* (Springer, Dordrecht, 1995).

[73] M. Chshiev, J. Velev, A. Kalitsov, and W. Butler, "Spin-dependent transport theory for nanoscale systems," .

[74] M. Chshiev, A. Manchon, A. Kalitsov, N. Ryzhanova, A. Vedyayev, N. Strelkov, W. H. Butler, and B. Dieny, *"Analytical description of ballistic spin currents and torques in magnetic tunnel junctions,"* Phys. Rev. B **92**, 104422 (2015).

[75] C. Petitjean, D. Luc, and X. Waintal, *"Unified drift-diffusion theory for transverse spin currents in spin valves, domain walls, and other textured magnets,"* Phys. Rev. Lett. **109**, 117204 (2012).

[76] P. Hohenberg and W. Kohn, *"Inhomogeneous electron gas,"* Phys. Rev. **136**, B864 (1964).

[77] W. Kohn and L. J. Sham, *"Self-consistent equations including exchange and correlation effects,"* Phys. Rev. **140**, A1133 (1965).

[78] K. Schwarz and P. Blaha, *DFT calculations of solids in the ground state* (2018).

[79] D. M. Ceperley and B. J. Alder, *"Ground state of the electron gas by a stochastic method,"* Phys. Rev. Lett. **45**, 566 (1980).

[80] A. Görling, *"Density-functional theory for excited states,"* Phys. Rev. A **54**, 3912 (1996).

[81] S. A. Tolba, K. M. Gameel, B. A. Ali, H. A. Almossalami, and N. K. Allam, *The DFT+U: Approaches, Accuracy, and Applications*, edited by G. Yang (IntechOpen, Rijeka, 2018) Chap. 1.

[82] A. Hallal, F. Ibrahim, H. Yang, S. Roche, and M. Chshiev, *"Tailoring magnetic insulator proximity effects in graphene: first-principles calculations,"* 2*D*. Mater. **4**, 025074 (2017).

[83] F. Ibrahim, A. Hallal, D. S. Lerma, X. Waintal, E. Y. Tsymbal, and M. Chshiev, *"Unveiling multiferroic proximity effect in graphene,"* 2*D* Materials **7**, 015020 (2019).

[84] F. Gimbert, *"Structure électronique et propriétés magnétiques de nanostructures et superéseaux* Co/Ni*(111)"*, Ph.D. thesis, Université Toulouse III Paul Sabatier, Toulouse, France (2012).

[85] C. W. Groth, M. Wimmer, A. R. Akhmerov, and X. Waintal, *"Kwant: a software package for quantum transport,"* New Journal of Physics **16**, 063065 (2014).

[86] S. Borlenghi, V. Rychkov, C. Petitjean, and X. Waintal, *"Multiscale approach to spin transport in magnetic multilayers,"* Phys. Rev. B **84**, 035412 (2011).

[87] T. P. Santos, L. R. Lima, and C. H. Lewenkopf, *"An order n numerical method to efficiently calculate the transport properties of large systems: An algorithm optimized for sparse linear solvers,"* Journal of Computational Physics **394**, 440 (2019).

[88] C. W. Groth, M. Wimmer, A. R. Akhmerov, and X. Waintal, "Kwant online documentation," `https://kwant-project.org/doc/dev/tutorial/`.

[89] A. Manchon, N. Ryzhanova, N. Strelkov, A. Vedyayev, and B. Dieny, *"Modelling spin transfer torque and magnetoresistance in magnetic multilayers,"* Journal of Physics: Condensed Matter **19**, 165212 (2007).

[90] D. M. Edwards, F. Federici, J. Mathon, and A. Umerski, *"Self-consistent theory of current-induced switching of magnetization,"* Phys. Rev. B **71**, 054407 (2005).

[91] H. Haugen, D. Huertas-Hernando, and A. Brataas, *"Spin transport in proximity-induced ferromagnetic graphene,"* Phys. Rev. B **77**, 115406 (2008).

[92] A. G. Swartz, P. M. Odenthal, Y. Hao, R. S. Ruoff, and R. K. Kawakami, *"Integration of the ferromagnetic insulator* EuO *onto graphene,"* ACS Nano **6**, 10063 (2012).

[93] Y.-F. Wu, H.-D. Song, L. Zhang, X. Yang, Z. Ren, D. Liu, H.-C. Wu, J. Wu, J.-G. Li, Z. Jia, B. Yan, X. Wu, C.-G. Duan, G. Han, Z.-M. Liao, and D. Yu, *"Magnetic proximity effect in graphene coupled to a* $\mathrm{BiFeO_3}$ *nanoplate,"* Phys. Rev. B **95**, 195426 (2017).

[94] H.-D. Song, Y.-F. Wu, X. Yang, Z. Ren, X. Ke, M. Kurttepeli, G. V. Tendeloo, D. Liu, H.-C. Wu, B. Yan, X. Wu, C.-G. Duan, G. Han, Z.-M. Liao, and D. Yu, *"Asymmetric modulation on exchange field in a* $\mathrm{graphene/BiFeO_3}$ *heterostructure by external magnetic field,"* Nano Letters **18**, 2435 (2018).

[95] D. A. Solis, A. Hallal, X. Waintal, and M. Chshiev, *"Proximity magnetoresistance in graphene induced by magnetic insulators,"* Phys. Rev. B **100**, 104402 (2019).

[96] V. Edelstein, *"Spin polarization of conduction electrons induced by electric current in two-dimensional asymmetric electron systems,"* Solid State Communications **73**, 233 (1990).

[97] J. Varignon, L. Vila, A. Barthélémy, and M. Bibes, *"A new spin for oxide interfaces,"* Nature Physics **14**, 322 (2018).

[98] I. I. Klimovskikh, M. M. Otrokov, V. Y. Voroshnin, D. Sostina, L. Petaccia, G. Di Santo, S. Thakur, E. V. Chulkov, and A. M. Shikin, *"Spin-orbit coupling induced gap in graphene on* Pt*(111) with intercalated* Pb *monolayer,"* ACS Nano **11**, 368 (2017).

[99] J. Sławińska and J. I. Cerdá, *"Spin–orbit proximity effect in graphene on metallic substrates: decoration versus intercalation with metal adatoms,"* New Journal of Physics **21**, 073018 (2019).

[100] A. Avsar, J. Y. Tan, T. Taychatanapat, J. Balakrishnan, G. K. W. Koon, Y. Yeo, J. Lahiri, A. Carvalho, A. S. Rodin, E. C. T. O'Farrell, G. Eda, A. H. Castro Neto, and B. Özyilmaz, *"Spin-orbit proximity effect in graphene,"* Nature Communications **5**, 4875 EP (2014), article.

[101] M. Gmitra, D. Kochan, P. Högl, and J. Fabian, *"Trivial and inverted dirac bands and the emergence of quantum spin hall states in graphene on transition-metal dichalcogenides,"* Phys. Rev. B **93**, 155104 (2016).

[102] T. S. Ghiasi, J. Ingla-Aynés, A. A. Kaverzin, and B. J. van Wees, *"Large proximity-induced spin lifetime anisotropy in transition-metal dichalcogenide/graphene heterostructures,"* Nano Letters **17**, 7528 (2017).

[103] K.-H. Jin and S.-H. Jhi, *"Proximity-induced giant spin-orbit interaction in epitaxial graphene on a topological insulator,"* Phys. Rev. B **87**, 075442 (2013).

[104] P. Lee, K.-H. Jin, S. J. Sung, J. G. Kim, M.-T. Ryu, H.-M. Park, S.-H. Jhi, N. Kim, Y. Kim, S. U. Yu, K. S. Kim, D. Y. Noh, and J. Chung, *"Proximity effect induced electronic properties of graphene on* Bi_2Te_2Se*,"* ACS Nano **9**, 10861 (2015).

[105] J. Zhang, C. Triola, and E. Rossi, *"Proximity effect in graphene–topological-insulator heterostructures,"* Phys. Rev. Lett. **112**, 096802 (2014).

[106] Z. Wang, C. Tang, R. Sachs, Y. Barlas, and J. Shi, *"Proximity-induced ferromagnetism in graphene revealed by the anomalous hall effect,"* Phys. Rev. Lett. **114**, 016603 (2015).

[107] Z. Qiao, W. Ren, H. Chen, L. Bellaiche, Z. Zhang, A. H. MacDonald, and Q. Niu, *"Quantum anomalous hall effect in graphene proximity coupled to an antiferromagnetic insulator,"* Phys. Rev. Lett. **112**, 116404 (2014).

[108] N. A. Spaldin, S.-W. Cheong, and R. Ramesh, *"Multiferroics: Past, present, and future,"* Physics Today **63**, 38 (2010).

[109] J. P. Velev, C.-G. Duan, J. D. Burton, A. Smogunov, M. K. Niranjan, E. Tosatti, S. S. Jaswal, and E. Y. Tsymbal, *"Magnetic Tunnel Junctions with Ferroelectric Barriers: Prediction of Four Resistance States from First Principles,"* Nano Letters **9**, 427 (2009).

[110] S. K. Gore, S. S. Jadhav, V. V. Jadhav, S. M. Patange, M. Naushad, R. S. Mane, and K. H. Kim, *"The structural and magnetic properties of dual phase cobalt ferrite,"* Scientific reports **7**, 2524 (2017).

[111] J. Slonczewski, *"Current-driven excitation of magnetic multilayers,"* Journal of Magnetism and Magnetic Materials **159**, L1 (1996).

[112] L. Berger, *"Emission of spin waves by a magnetic multilayer traversed by a current,"* Phys. Rev. B **54**, 9353 (1996).

[113] M. Tsoi, A. G. M. Jansen, J. Bass, W.-C. Chiang, M. Seck, V. Tsoi, and P. Wyder, *"Excitation of a magnetic multilayer by an electric current,"* Phys. Rev. Lett. **80**, 4281 (1998).

[114] J. A. Katine, F. J. Albert, R. A. Buhrman, E. B. Myers, and D. C. Ralph, *"Current-driven magnetization reversal and spin-wave excitations in* Co/Cu/Co *pillars,"* Phys. Rev. Lett. **84**, 3149 (2000).

[115] J. Grollier, V. Cros, H. Jaffrès, A. Hamzic, J. M. George, G. Faini, J. Ben Youssef, H. Le Gall, and A. Fert, *"Field dependence of magnetization reversal by spin transfer,"* Phys. Rev. B **67**, 174402 (2003).

[116] T. Valet and A. Fert, *"Theory of the perpendicular magnetoresistance in magnetic multilayers,"* Phys. Rev. B **48**, 7099 (1993).

[117] M. D. Stiles and A. Zangwill, *"Anatomy of spin-transfer torque,"* Phys. Rev. B **66**, 014407 (2002).

[118] A. Shpiro, P. M. Levy, and S. Zhang, *"Self-consistent treatment of nonequilibrium spin torques in magnetic multilayers,"* Phys. Rev. B **67**, 104430 (2003).

[119] A. Brataas, Y. V. Nazarov, and G. E. W. Bauer, *"Finite-element theory of transport in ferromagnet–normal metal systems,"* Phys. Rev. Lett. **84**, 2481 (2000).

[120] A. Brataas, G. E. Bauer, and P. J. Kelly, *"Non-collinear magnetoelectronics,"* Physics Reports **427**, 157 (2006).

[121] P. M. Haney, D. Waldron, R. A. Duine, A. S. Núñez, H. Guo, and A. H. MacDonald, *"Current-induced order parameter dynamics: Microscopic theory applied to* Co/Cu/Co *spin valves,"* Phys. Rev. B **76**, 024404 (2007).

[122] A. Manchon, N. Ryzhanova, A. Vedyayev, M. Chschiev, and B. Dieny, *"Description of current-driven torques in magnetic tunnel junctions,"* Journal of Physics: Condensed Matter **20**, 145208 (2008).

[123] X. Waintal, E. B. Myers, P. W. Brouwer, and D. C. Ralph, *"Role of spin-dependent interface scattering in generating current-induced torques in magnetic multilayers,"* Phys. Rev. B **62**, 12317 (2000).

[124] N. Locatelli, V. Cros, and J. Grollier, *"Spin-torque building blocks,"* Nat. Mater. **13**, 11 (2014).

[125] C.-C. Lin, A. V. Penumatcha, Y. Gao, V. Q. Diep, J. Appenzeller, and Z. Chen, *"Spin transfer torque in a graphene lateral spin valve assisted by an external magnetic field,"* Nano Letters **13**, 5177 (2013).

[126] C. Baraduc, M. Chshiev, and U. Ebels, *Nanomagnetism and Spintronics*, pp. 173–192, https://www.worldscientific.com/doi/pdf/10.1142/9789814273060$_0$008 .

[127] D. Ralph and M. Stiles, *"Spin transfer torques,"* Journal of Magnetism and Magnetic Materials **320**, 1190 (2008).

[128] B. Dieny, R. B. Goldfarb, and K.-J. Lee, *Introduction to Magnetic Random-Access Memory* (IEEE press, 2016).

[129] J. Sun and D. Ralph, *"Magnetoresistance and spin-transfer torque in magnetic tunnel junctions,"* Journal of Magnetism and Magnetic Materials **320**, 1227 (2008).

[130] H. Yoda, T. Kishi, T. Nagase, M. Yoshikawa, K. Nishiyama, E. Kitagawa, T. Daibou, M. Amano, N. Shimomura, S. Takahashi, T. Kai, M. Nakayama, H. Aikawa, S. Ikegawa, M. Nagamine, J. Ozeki, S. Mizukami, M. Oogane, Y. Ando, S. Yuasa, K. Yakushiji, H. Kubota, Y. Suzuki, Y. Nakatani, T. Miyazaki, and K. Ando, *"High efficient spin transfer torque writing on perpendicular magnetic tunnel junctions for high density* MRAMs,*"* Current Applied Physics **10**, e87 (2010), 2009 International Symposium on Next Generation Terabit Memory Technology.

[131] J. Slonczewski, *"Currents and torques in metallic magnetic multilayers,"* Journal of Magnetism and Magnetic Materials **247**, 324 (2002).

[132] O. Parcollet and X. Waintal, *"Spin torque in a nanomagnet coupled to noncollinear ferromagnetic electrodes,"* Phys. Rev. B **73**, 144420 (2006).

[133] K. An, A. N. Litvinenko, R. Kohno, A. A. Fuad, V. V. Naletov, L. Vila, U. Ebels, G. de Loubens, H. Hurdequint, N. Beaulieu, J. Ben Youssef, N. Vukadinovic,

G. E. W. Bauer, A. N. Slavin, V. S. Tiberkevich, and O. Klein, *"Coherent long-range transfer of angular momentum between magnon kittel modes by phonons,"* Phys. Rev. B **101**, 060407 (2020).

[134] N. Beaulieu, N. Kervarec, N. Thiery, O. Klein, V. Naletov, H. Hurdequint, G. de Loubens, J. Ben Youssef, and N. Vukadinovic, *"Temperature dependence of magnetic properties of a ultrathin yttrium-iron garnet film grown by liquid phase epitaxy: Effect of a* Pt *overlayer,"* IEEE Magnetics Letters **9**, 1 (2018).

[135] E. M. Chudnovsky and J. R. Friedman, *"Macroscopic quantum coherence in a magnetic nanoparticle above the surface of a superconductor,"* Phys. Rev. Lett. **85**, 5206 (2000).

[136] D. N. Bose, S. R. Borgaonkar, and T. S. Vedavathy, *"Measurement of magnetic properties of single crystal yig by non-resonant method,"* Bulletin of Materials Science **1**, 121 (1979).

[137] M. Wu, *Nonlinear Spin Waves in Magnetic Film Feedback Rings*, edited by R. E. Camley and R. L. Stamps, Solid State Physics, Vol. 62 (Academic Press, 2010) pp. 163 – 224.

List of Figures

List of Tables

Acronyms

CIP	Current in Plane
CPP	Current perpendicular to Plane
DFT	Density Functional Theory
FM	Ferromagnet
GMR	Giant Magnetoresistance
GNR	Graphene Nanoribbon
MI	Magnetic Insulator
MFPE	Multiferroic-induced Proximity Effect
MRAM	Magnetic Random Access Memory
PER	Proximity Electroresistance
PMR	Proximity Magnetoresistance
QAHE	Quantum Anomalous Hall effect
QHE	Quantum Hall effect
SHE	Spin Hall effect
SOC	Spin Orbit Coupling
STT	Spin Transfer Torque
TB	Tight Binding
TMDC	Transition Metal Dichalcogenide
MTJ	Magnetic Tunnel Junction
TMR	Tunnel Magnetoresistance